Untersuchungen zur Scherbeanspruchung von Membranplatten des MBR-Verfahrens durch Einzel-luftblasen mit Hilfe von CFD

Examinations of the shear stress on MBR-membrane plates by a single bubble using CFD

Masterarbeit von
Yingchen Cao, Matr.: 2594611
Betreuer: Dr. Alexander Sonnenburg
Prüfer: Prof. Dipl. –Ing. Dr. nat. techn. Wilhelm Urban
Institut für Wasserversorgung und Grundwasserschutz
Darmstadt, 12.2015

TECHNISCHE
UNIVERSITÄT
DARMSTADT

Declaration

Erklärung zur Abschlussarbeit gemäß §22, Abs.7 APB

Hiermit versichere ich, die vorliegende Abschlussarbeit ohne Hilfe Dritter nur mit den angegebenen Quellen und Hilfsmitteln angefertigt zu haben. Alle Stellen, die aus den Quellen entnommen wurden, sind als solche kennlich gemacht worden. Diese Arbeit hat in gleicher Form oder ähnlicher Form noch keiner Prüfungsbehörde vorgelegen.

Darmstadt, den_____

_____
Unterschrift

Abstract

Nowadays the use of membrane filtration process is rapidly increasing in industrial fields, especially in the field of water and wastewater treatment. Aeration is one of the most important processes in MBR systems. The cost of aeration is the main operating cost. It can provide the biomass with oxygen and prevent them from settling down. Besides, the shear stress created by the aeration process can scour the solid from the membrane surface to control the growth of cake layer and increase the filtration flux.

At the same time computational fluid dynamics (CFD) has become a leading modeling and analysis tool for fluid simulation because of its advances in computational performance. Recently more and more studies have used CFD techniques to investigate and model the fluid flow through a membrane module and to study the membrane performance.

The aim of this thesis is to investigate the shear stress on the membrane plate induced by a single bubble in the MBR system. A better understanding of the shear stress caused by aeration in MBR, which depend greatly on operating conditions and bubble size, can be achieved by using numerical simulation. This thesis focuses on the operation conditions, bubble sizes and the geometry of the membrane models etc. as well as their influence on shear stress.

The thesis firstly introduces the basics of membrane and CFD as well as the model theories. Then a model for simulation of the membrane systems is established and its independence on the mesh size and model geometry was tested. Experiments for validation are conducted. The results of this simulation and the results from the experiments and from literature are presented and compared. Finally in models with an appropriate geometry, an appropriate mesh size and most importantly reliable results, different simulations are carried out to simulate the bubble formation, to investigate the effect of different parameters on the bubble motion, to study what affects the shear stress and shear force, especially in the escape zone, where the bubble moves out of the gap between the submerged flat sheet membranes.

The novel of this study lies in the flexibility of membranes. The membrane in almost all CFD simulations for membrane in previous studies was set as rigid wall. In the last part of this thesis, the membrane was set to be flexible. A two-way system coupling was applied for the simulation of the membrane movement and the rise of the bubble.

At first the formation of bubbles was studied. The amount of gas injected into the water, the way it is injected (continued aeration and discontinued aeration), the inlet configurations and the inlet velocity of the gas determine the bubble shape and size. Then it was found out that the bubble size has a very powerful impact on the bubble motion and shear stress exerted by rising bubbles. An increase in bubble size leads to an increase in maximal shear stress, which also means an increase in cleaning effect on the membrane surface in the filtration. When the bubble size is larger than the gap width, this cleaning effect is no longer that much significant. As for the bubble rising velocity, it reaches its maximal value at a bubble diameter of 5 mm, above which, the wall effect of the membrane makes the bubble slow down. This effect was more significant for the bubbles, whose diameter is larger than the channel gap of membranes. For these bubbles a slug flow could be observed, and according to their spherical-cup shape, they belong to Taylor bubbles. To identify the most effective multi-phase flow pattern for fouling control, membrane module configurations with different gap width were evaluated with CFD. The shear stress was found out to be highest at the smallest gap distance. Considering the clogging problem for small membrane gaps, it is concluded that the rise of a 5 mm bubble between the membranes with a gap of 6 mm might be the optimal conditions for the aeration during the filtration process. The fluid velocity was also investigated in this study. The averaged shear stress shows a linear dependence on the fluid velocity and the bubble motion can increase the shear stress at low fluid velocity significantly. 2d simulation and 3d simulation were also compared in this study. The

numerical results from 3d simulation were more reliable. At last a two-way system coupling simulation was performed to investigate the effect of membrane movement on the shear stress. It was found out that the maximal shear stress produced by membrane movement and bubble rising is more than ten times greater than that only induced by the rise of a single bubble.

Keywords: *CFD* *Shear Stress* *Flat Sheet Membrane* *Multi-phase Simulation* *Bubble Formation* *Two-way System Coupling* *Flexible Membrane*

Acknowledgement

This Master's Thesis consumed a lot of time, work and research. Still, it would be not possible to finish this within the limited time without the support of many individuals and the company of MICRODYN-NADIR. Therefore, I would like to express my gratitude to all of the people who offered me valuable help, advice and encouragement during the writing of my thesis.

First of all I would like to thank my supervisor, Dr. Alexander Sonnenburg, for giving me this opportunity to write my thesis on this topic. I am deeply grateful of his instructive guidance, advice and suggestions. Without them it would be impossible for this thesis to reach its present form.

Secondly, I would like to thank Mr. Bareth for offering the place and apparatus for the experiment, for offering me the opportunity to write my thesis at the company MICRODYN-NADIR, where I learned a lot.

Thirdly, I want to express my thanks to the friends, who helped me build the small model for my experiment using a 3D printer.

Last but not Least, I would like to extend my thanks towards my family and my friends for encouraging me, supporting me and caring for me.

Contents

1. Introduction

1.1. Motivation

During the last decades, the MBR technology has been widely applied and well developed in municipal and industrial wastewater treatment. An MBR can be regarded as a conventional activated sludge process coupled with membrane filtration to separate solid and liquid. The pore size of the membrane is so small, that it can produce a clarified and disinfected effluent [1]. In addition, it can allow higher mixed liquor suspended solids (MLSS) concentration in the bioreactor compared to the conventional activated sludge process. Therefore, the footprint of a bioreactor's tank can be reduced. Furthermore, it produces less excess sludge, which means that the solid retention time (SRT) in MBR process is larger.

However, membrane fouling is the major obstacle to wide application and development. Fouling, which is caused by the block of the pores of the membranes during the accumulation of particles on the membrane surface, can lead to a significant increase in the hydraulic resistance of membranes. In this case the driving pressure, which forces the fluid going through the membrane will be increased or the flux through the membrane will be declined. In other words, fouling has a considerable negative effect on membrane performance during the filtration.

One of the most important ways to control membrane fouling and improve the performance in the MBR system is aeration. Aeration can provide biomass with sufficient oxygen and keep them not to settle down. During the aeration process, shear stress exerted by rising bubbles can scour the solids from the membrane surface to control the cake layer growth. However, the cost of the aeration process accounts for the major operating cost in the MBR system. So it is necessary to save energy and operating costs by using of bubbles and optimizing the configurations of membrane modules.

Another problem that occurs during the aeration process in practice is that the membrane may be broken in case of large bubbles, when they move out of the channel gap between the membranes.

This study was carried out to achieve a better understanding of multi-phase flow pattern for the flat sheet membranes in the MBR system, to investigate the affecting factors in the bubble formation, to find out the most appropriate bubble size and the best configurations of membrane modules for aeration process. In addition, the shear force induced by the rise of a single bubble near the membrane upper edge in different operation conditions was calculated to provide insights into the dependence of shear force in this area on the bubble size and the operating conditions. The challenge of this simulation is that the membrane plate is flexible in practice, which may affect the flow pattern in channel gap. How to carry out the simulation in this case was described in chapter 7 of the thesis.

1.2. Thesis Outline

This thesis consists of 8 chapters and each chapter is described separately as below:

Chapter 1 consists of the motivation of the thesis and outlines the structure of the thesis.

Chapter 2 introduces the basics of membrane filtration, the background knowledge of CFD simulation as well as the model theories.

Chapter 3 is the review of previous literatures in the fields of CFD simulation for MBR systems on a large scale and on a small scale as well; in the field of multi-phase modeling (water and gas). A literature review about the rheology of MBR sludge and its mathematical expressions is also included in this part. At last the ASM model for CFD simulations was reviewed in this chapter as well.

Chapter 4 provides the description of different models for simulation of the membrane systems. The independence on the mesh size and model geometry of these models was tested in this chapter. At last a model with the most appropriate mesh size and the most appropriate domain geometry was chosen to obtain a reliable result.

Chapter 5 describes the experimental setup and the data processing from the experiment.

Chapter 6 is the discussion of the results. At first the results of this simulation were checked against the results of the experiments and from literature. The affecting factors in the bubble formations are discussed. The effects of different parameters on the bubble motion, on the shear stress and shear force, especially in the escape zone, where the bubble moves out of the gap, were investigated in this chapter. The reliability of 2d simulation and 3d simulation was compared at last.

Chapter 7 describes the further work, which can be carried out in the future. A two-way system coupling simulation to investigate the flexible membrane wall movement and its effect on the flow field in the channel gap between membranes was provided in this section.

Chapter 8 provides the conclusions of the thesis, which are drawn from this study and some considerations based on the study. Some suggestions about coupling the ASM model in the simulation and the patch of a group of bubbles with different diameters are also given in this chapter.

2. Theoretical Background

2.1. Membrane Technology

2.1.1. Membrane Processes

A membrane is a perm-selective layer which can be used to separate particles from liquid, when adequate pressure is applied to its surface. As shown in Figure 2.1, during the operation, the water (Feed) is pumped across the membrane, which allows certain constituents to pass through it and other constituents still remain in the stream, which is known as waste stream, concentrate or retentate. The stream that contains permeable components is known as product stream or permeate, which is relatively free of constituents.

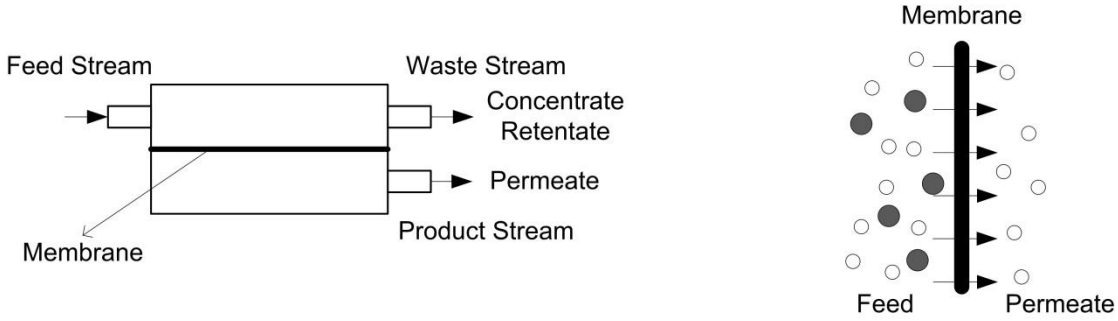

Figure 2.1 Schematic of Membrane Separation Process (left) and Particle Removal via Membrane (right)

Membrane filtration has a very wide spread in the field of environmental and industrial processing, including [2]:

a) Seawater desalination to produce drinking water;
b) Reclaimed water reuse to produce drinking water;
c) Drinking water purification by removing pathogens and contaminants;
d) Municipal sewage and industrial wastewater treatment;
e) Wastewater reuse for other industry;
f) Recovery of valuable materials from industrial effluent.

Four types of membranes are mainly used in water and wastewater treatment: microfiltration (MF), ultrafiltration (UF), nanofiltration (NF) and reverse osmosis (RO). This classification is mainly based on membrane pore size. There are a lot of classification criteria of membranes. According to different operating pressures, membranes can be divided into low-pressure membranes and high-pressure membranes. While NF and RO are high-pressure membranes, MF and UF belong to the low-pressure membranes with an operating pressure under 5 bars. Table 2-1 shows an overview of different types of membranes.

Table 2-1 Classification of membrane processes

Membrane	Pressure [3]	Pore Size [3]	Removal Mechanism	Transport Mechanism	Removable Components [4]
MF	1-2 bar	0.05-10 μm	Sieving	Convection	Particles, Sediment, Algae, Protozoa, Bacteria
UF	2-5 bar	0.001-0.05 μm	Sieving	Convection	Small colloids, Viruses
NF	5-15 bar	<2.0 nm	Diffusion	Diffusion	Dissolved organic matter, Divalent ions (Ca^{2+}, Mg^{2+})
RO	15-100 bar	~0.6 nm	Diffusion	Diffusion	Monovalent species (Na^{+}, Cl^{-})

The membrane filtration process in this thesis is focused on MF and UF, which are mainly used in membrane bio-reactors (MBRs) in wastewater treatment.

2.1.2. Membrane Performances

Like other filtration processes MF and UF separate particles from the liquid phase that can pass through a porous medium. Just like the conventional filtration, a cake of solids can be formed at the surface of the membrane due to straining during the filtration, as shown in Figure 2.2. This cake layer can be regarded as a "dynamic" membrane, which only allows even smaller particles to pass through it, resulting in declining flux or increasing the trans-membrane pressure (TMP).

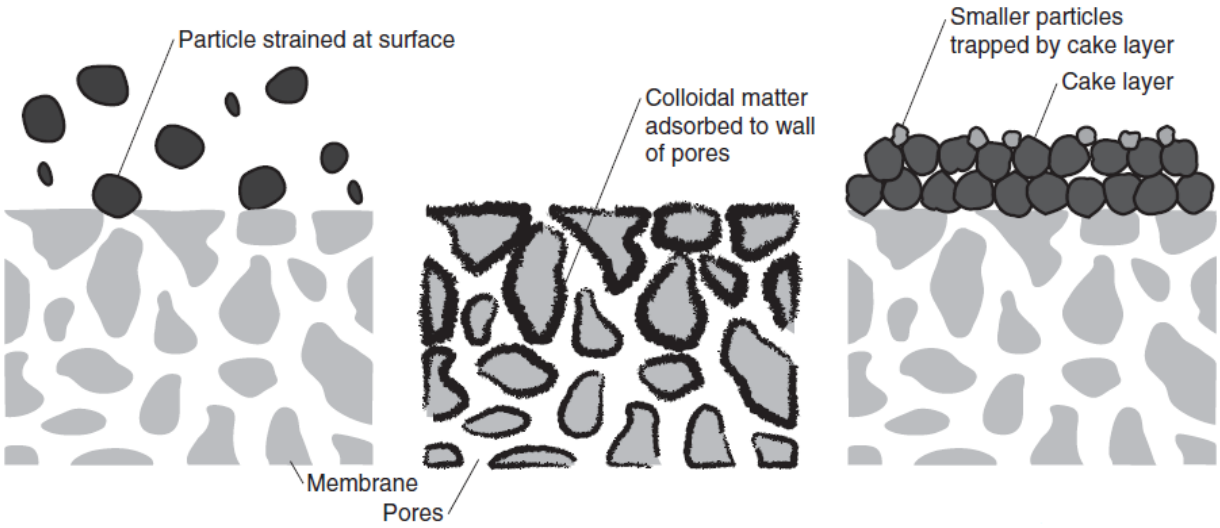

Figure 2.2 Straining in the membrane filtration (left), Adsorption to wall of pores (center), Cake formation at the membrane surface (right) (taken form [4])

Some particles, e.g. natural organic matter (NOM) are not only accumulated at the membrane surface, they can go deeper into the membrane and then will be adsorbed to wall of pores, as shown in the middle of Figure 2.2. This process is known as fouling which can also be caused by pore blocking and cake formation. As parts of the porous area are blocked and some pores become smaller due to adsorption, the hydraulic resistance, which is inversely correlated to the effective pore areas, increases significantly. In other words the driving pressure, which forces the fluid through the membrane, will be increased or the flux through the membrane will be declined.

A great number of studies [5-8] show that wall shear stress is a very important parameter, which can be used to indicate the membrane performance. It is well known that particles accumulated on the membrane surface will be flushed away, when the shear stress increases, because it can increase the back-transport of particles away from the membrane. An earlier study on the relationship between the membrane fouling and the ratio between the permeate flux and wall shear stress was investigated by LeBerre and Daufin in 1996 [5]. It shows that the ratio between the permeate flux and wall shear stress could be a useful parameter to predict the membrane performance in different operating conditions. In later studies [6-10], the effect of wall shear stress on membrane fouling during membrane filtration was investigated by numerical simulation using CFD [6-9] or experimentally [10]. All these studies indicate that the surface shear stress could be used as a useful parameter to indicate the membrane performance.

2.1.3. Membrane Operation Modes

A major problem that limits the application of membrane is the effect of membrane fouling and cake formation. To minimize this negative effect a suitable operation mode should be wisely chosen. Three types of membrane operation modes are mainly used in water and wastewater treatment: Dead-End-Filtration mode, Cross-Flow-Filtration mode and Submerged-Filtration mode.

Dead-End-Filtration is the most fundamental mode, in which the feed flow is normal to the membrane, resulting in a large number of constituents accumulating on the surface of membrane and generating a layer of solids known as filter cake. This filter cake can also act as filter media. But it also makes the TMP significantly increasing.

Compared to Dead-End-Filtration is the feed flow in Cross-Flow-Filtration tangential to the filter media. This tangential flow can scour the particles and prevent them from accumulating on the membrane surface. To this purpose a large velocity is needed to create turbulence, which means that the energy consumption of Cross- Flow-Filtration is much bigger than that of Dead-End-Filtration.

In Submerged-Filtration mode the membrane are direct installed in the tank with the feed mixture. A vacuum is applied as a driving force on the inner side of membrane, which forces permeate to go through the filter media into membrane. This filtration process is illustrated in Figure 2.3. But because of the vacuum, the driving force is limited and it's lower than that in other filtration modes. As a result of the limited driving force restrictions on permeate flux and TMP are imposed. The maximal TMP in submerged membrane system is about 0.5 bars [4] and the typical TMP of submerge membrane filtration is 0.2 bars [4]. Furthermore, gas sparging is applied along the membrane surface in order to promote turbulence, which controls and limits the growth of filter cake. It should be noted that the submerged filtration is often referred to Cross-Flow-Filtration, because the feed flow near the membrane surface can be regarded as bubble-induced tangential flow.

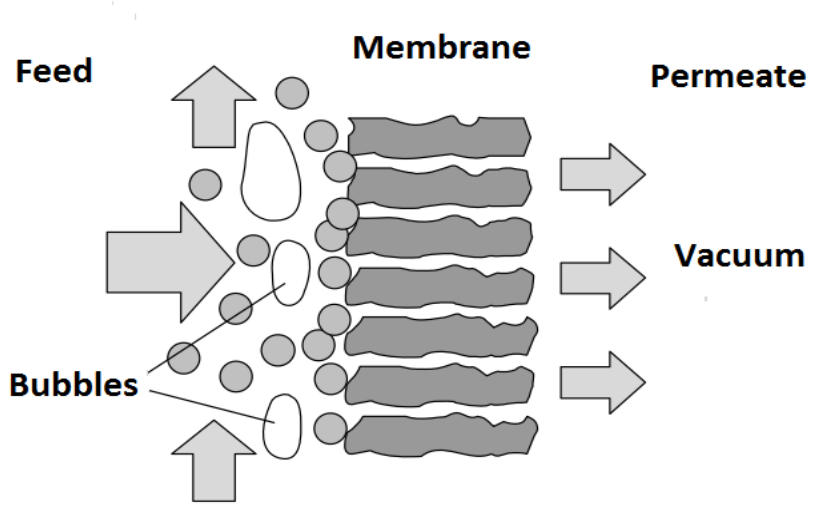

Figure 2.3 The submerged membrane system (adapted from [11])

2.1.4. Membrane Modules

In the previous section the operating principle of submerged membrane filtration is fully described. In this section the two most common modules in submerged membrane filtration will be discussed: submerged Hollow-Fiber Module and submerged Flat-Sheet Module, as shown in Figure 2.4. Except the two modules there's a spiral wound module, which is mainly used in RO and NF.

Hollow-Fiber membranes, as shown on the right side of Figure 2.4, have a bundle of fibers with a diameter ranging from 0.5-5 mm [11] and therefore a high packing density. The fiber can swag with the bubble flow since it is held loosely between each end of the fiber. During the membrane filtration, clean water is extracted from the feed mixture via the hollow fiber wall into the hollow fiber and then exits the open fiber ends, where pump develops suction on it.

Flat-Sheet Module as shown on the left side of the following figure has many planar and rectangular sheets or most commonly panels. These filtration elements are normally regarded as rigid, but actually they are not fixed, they can swag with the bubble flow. During the membrane filtration the water flows from outside the membrane surface via the wall of the panel into the inside of the panel. And then permeate will be collected from the outlet tubes, where a vacuum is applied.

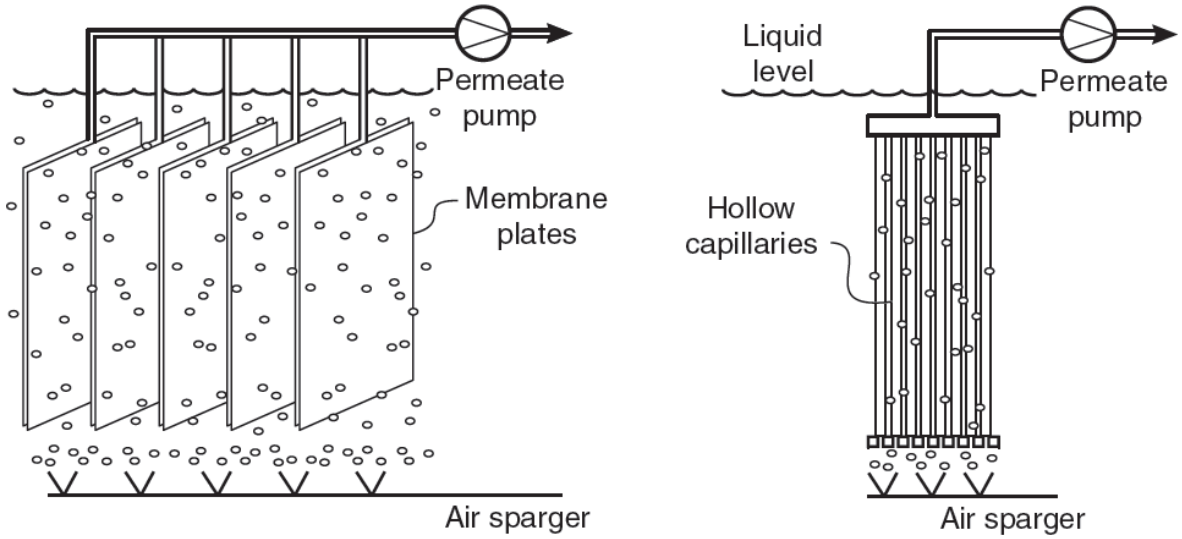

Figure 2.4 Submerged Flat-Sheet Module (left) and Submerged Hollow-Fiber Module (right) (adapted from [12])

Compared to Hollow Fiber membrane the Flat Sheet membrane hat a relative lower packing density and is not that much easy to clog. The advantages and disadvantages of the two types of membrane modules are listed in Table 2-2.

Table 2-2 Comparison of Hollow-Fiber Membrane and Flat-Sheet Membrane

Membrane Module	Advantages	Disadvantages
Hollow Fiber Membrane	• High packing density (750-1700 m^2/m^3) [4] • Cost-effective manufacture [11] • Can be designed to at higher flux [13] • Easy to back wash	• Easy to block • Bad substances exchange because of the laminar flow inside the hollow fiber [11] • More frequent cleaning (mechanically and chemically) [13] • Operation at lower MLSS concentration [13]
Flat Sheet Membrane	• Each membrane panel can be changed separately • Less prone to contamination [11] • Longer Operation time without cleaning [14]	• Low packing density (<400 m^2/m^3) [11] • Restriction on backwashing • Larger pressure drop [11]

2.2. Gas Sparging in MBR

Aeration in the MBR system is the most important process, which makes up more than 90% of the total cost in MBR systems [15]. Because of its high energy consumption aeration is also the main operating cost in MBRs. The key contributing factor to evaluate the energy demand in MBRs is the specific aeration demand, i.e. specific aeration demand against the membrane area (SAD_m) and specific aeration demand against the permeate volume (SAD_p):

$$SAD_m = \frac{Q_{A,m}}{A_m} [Nm^3/m^2/h] \quad (2\text{-}1)$$

$$SAD_p = \frac{Q_{A,m}}{JA_m} [-] \quad (2\text{-}2)$$

Where $Q_{A,m}$ is the air flow rate, whose unit is m^3/h. A_m is the total membrane surface area (m^2) and J is the permeate flux (m/h). The value of SAD_m ranges from 0.1 to 0.6 m^3 air/m^2 membrane/h [16] and SAD_p changes from 7 to 17 m^3 air/m^3 permeate [16]. SAD_p indicates the operation cost in MBRs more directly than SAD_m.

Aeration on the one hand can provide necessary oxygen biomass and keep them not to settle down, which is known as biomass aeration; on the other hand can scour solids from the membrane surface to control the growth of cake layer by creating turbulence, which is regarded as membrane aeration. Cui [17] reported that a bubble-induced secondary flow that can promote the local mixing and enhance the membrane filtration is generated by gas sparging. This section will be focused on the membrane aeration. Bubble size, bubble shape and air flow velocity are key factors [18], which should be taken into consideration during the design and operation of a MBR system. A great number of studies [15, 17-19] have been conducted to investigate and model the membrane aeration. Judd et al [20] have determined the effect of two types of air sparging technology on the membrane performance, showing that in air-lift module the flux was increased by 43% and no further flux increase can be observed when the gas flow velocity increases and the air-jet module tends to be clogged due to the cake layer inside the lumen. The relationship between the aeration rate and the membrane permeability was investigated by Rahimi [21], which showed that the optimum range of aeration rate is 151-184 l gas/h with a SAD_m of 0.8-1.2 m^3 air/m^2 membrane/h. Furthermore, the distance of two plates also strongly affects the bubble shape and shear stress in the membrane filtration. It is expected that [22] the highest shear stress can be achieved with narrower channels.

2.2.1. Bubble Size and Frequency

When gas is injected into the MBR system, bubbles are formed and rise in the liquid medium because of buoyancy force. The size of the bubbles depends on the sparger type and the gas flow rate [18]. The Bubbles generated from the gas sparger can be grouped into fine bubbles and coarse bubbles. Fine bubbles can induce higher cross-flow velocity, therefore creating stronger wall shear stress than coarse bubbles, as reported in the study of Sofia et al [23]. The main difference between the fine and the coarse bubbles are listed in Table 2-3. A study [24] of bubble size on mass transfer in membrane filtration found that a critical bubble size existed that could enhance the mass transfer and give the most efficient enhancement of permeate flux. The bubble size was found to vary in a wide range, from 0.2 to 50 mm but the majority is in the range of 3-5 mm [25] .

Bubbling frequency has a positive correlation with shear stress [15]. Therefore an increasing bubble frequency can contribute to a better membrane fouling control. However, it results in high operating cost in MBR system. Furthermore the fouling rates decrease hardly when the frequency is increasing by more than 1 Hz. An optimal bubble frequency of 0.4 Hz was reported in the study of cui et al. [24].

Table 2-3 Comparison of fine and coarse bubbles

Features	Fine bubbles	Coarse bubbles
Size [1]	2-5 mm	6-10 mm
OTE (percentage of O_2 transfer [1] per m depth)	3-10%	1-3%
Cross-flow velocity [23]	high	low
MBR operation time [15]	8 months	4 weeks
Distribution	more uniform	less uniform

2.2.2. Bubble Shape and Rising Velocity

The shape of the bubbles can be divided into three categories: Spherical bubbles, Ellipsoidal bubbles and Spherical-cap or Ellipsoidal-cap bubbles [26]. The characteristics of these shape regimes are summarized below in Table 2-4:

Table 2-4 Characteristics of bubble shape regimes

Features	Spherical bubbles	Ellipsoidal bubbles	Spherical-cap bubbles
Size [18]	<1 mm	1.5-15 mm	>15 mm
Terminal rise velocity	$U_b = \frac{d_e^2 g(\rho_l - \rho_g)}{18\mu_l}$ (for Re<1) [18]	~0.24 m/s (for d_e=4-5 mm) [18] $U_b = (\frac{2.14\sigma}{\rho d_e} + 0.505 g d_e)^{0.5}$ (for d_e>1.3 mm) [26]	$U_b = 0.71(g d_e)^{0.5}$
Vortex wake [18]	No wake region	Helical vortex wakes	A wake region with shields vortex ring

Where U_b is the terminal velocity (m/s); d_e is the bubble diameter (m); ρ_g is the density of gas and ρ_l is the density of liquid, their unity is kg/m^3; μ_l is the dynamic viscosity of liquid (Ns/m^2); σ is the surface tension (N/m).

Generally speaking, bubble shape depends on its velocity. Bubbles with low velocity are spherical and they start to deform with increasing velocity [27]. At high gas flow rates, the velocity does not depend on the fluid viscosity. However, at slow velocity the fluid viscosity affects the bubble velocity. The relationship between the velocity and bubble diameter at high gas flow rates can be determined by the Davidson and Harrison model [27]:

$$U_b = 0.71(g d_e)^{0.5} \tag{2-3}$$

The dynamic of bubble rising in the water may be governed by the following forces: i.e. inertial force (F_i), buoyancy force (F_b), viscous force (F_μ), and surface force (F_s). The bubble motion may be characterized by the following parameters: the bubble rising velocity V_T, gravitational acceleration g, water density ρ_L, gas density Δρ or ($\rho_L - \rho_g$), bubble equivalent diameter d_e, water viscosity μ_L and surface tension σ. Based on the Π-theory, the following dimensionless variables Reynolds number (Re), Eotvos number (Eo), Morton number (M), Froude number (Fr) and Weber number (We) can be gained by the following equations:

$$Re = \frac{F_i}{F_\mu} = \frac{\rho_L V_T d}{\mu_L} \tag{2-4}$$

$$Eo = \frac{F_b}{F_s} = \frac{\Delta\rho g d^2}{\sigma} \tag{2-5}$$

$$M = \frac{F_\mu^4 F_b}{F_s^3 F_i^2} = \frac{\Delta\rho g \mu_L^4}{\rho_L^2 \sigma^3} \tag{2-6}$$

$$Fr = \sqrt{\frac{F_i}{F_b}} = \frac{V_T}{\sqrt{\frac{\Delta\rho g d}{\rho_L}}} \tag{2-7}$$

$$We = \frac{F_i}{F_s} = \frac{\rho_L {V_T}^2 d}{\sigma} \tag{2-8}$$

Using these dimensionless numbers, the bubble shape regime of a single bubble can be estimated. Based on the Reynolds number (*Re*), Eotvos number (*Eo*) and Morton number (*M*), a graphical correlation was proposed by Grace [28].

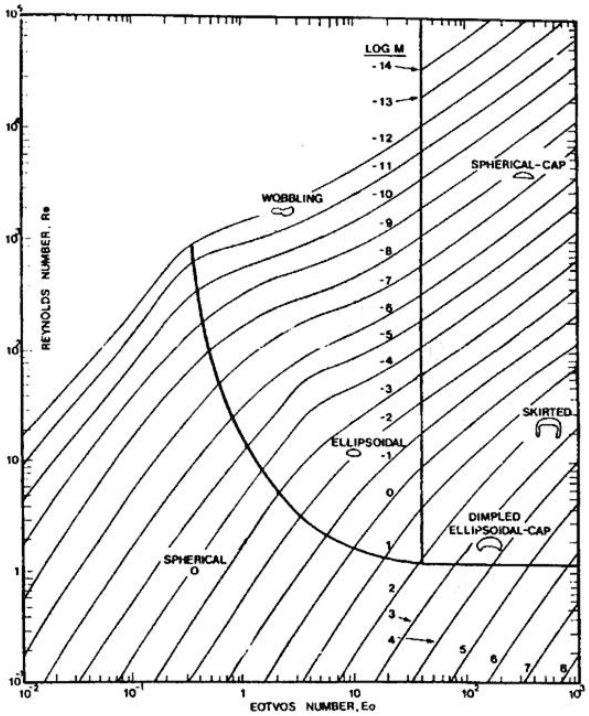

Figure 2.5 Bubble shape regime map of Grace [28] (adapted from Annaland M. V. et al. [29])

2.2.3. Flow Patterns

There are five common flow patterns of gas/liquid vertical flow: Bubble flow, Slug flow, Churn flow, Annular flow and Disperse flow [30]. At low gas volume fractions (about 1%) [30], the two-phase flow regime tends to be the bubble flow pattern, as shown first in Figure 2.6. At a gas volume fraction between 4.5% and 15% [30], the flow becomes unsteady, which promotes large scale mixing motions and makes the bubble to have a larger diameter. At even larger gas volume fractions, the fluid flow will show a churn flow pattern, successively as annular pattern and at last disperse flow pattern, as shown in Figure 2.6.

Given the high cost in aeration, two main bubbling regimes: slug bubble and free bubble are used in the MBR system. It was found that compared to the bubble flow regime the slug flow regime can provide a larger permeate flux and better control of fouling [31]. However, slug flow has higher energy consumption than bubble flow. Zhang et al. [31] studied the effect of two bubbling regimes on

the membrane performance and energy cost in MBR and found that the slug flow regime in flat sheet MBRs seems to be more energy saving and an optimal gas bubbling rate is 2.5 l/min, when the energy demand and the performance are taken into consideration together.

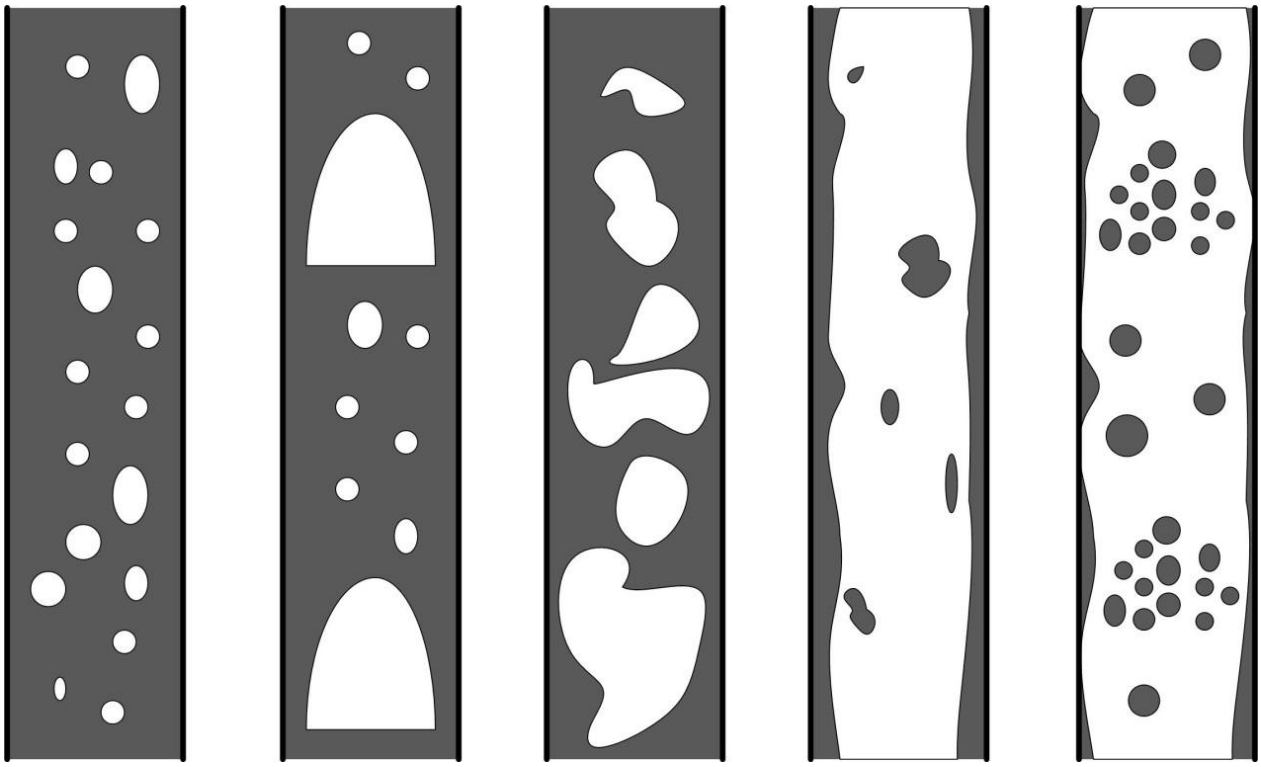

Figure 2.6 Sketches of flow regimes for two-phase vertical fluid flow (from left to right: Bubble flow, Slug flow, Churn flow, Annular flow and Disperse flow)

2.3. Computational Fluid Dynamics (CFD)

2.3.1. CFD Technology

Computational Fluid Dynamics or CFD is the use of numerical methods and algorithms to analyze problems involving fluid dynamics, heat and mass transfer, transport process and so on. As an analysis tool, CFD has the advantages such as the reduction of lead times and costs [32, 33], the ability to study the effect of reactor geometry on hydrodynamics to achieve the optimal reactor design [33], the ability to easily change the operating conditions [34]. In addition, it can provide a great deal of information about the flow data at any position and time [35]. CFD because of its advances in computational performance has become a leading modeling and analysis tool for fluid simulation and is widely applied in the areas [32]: aerodynamics of aircraft and vehicles, hydrodynamics of ships, turbo-machinery, chemical process engineering, bio-medical engineering and many other fields.

2.3.2. Governing Equations

The fundamental governing equations of fluid dynamics, upon which all of fluid dynamics are based, are continuity, momentum and energy equations that are respectively the mathematical statement of foundational physical conservation laws for all of fluid dynamics [36, 37]: the conservation of mass, the newton's second law (or the conservation of momentum) and the conservation of energy. These basic mass conservation laws and momentum conservation law can be described by the following equations [35], respectively:

$$\frac{\partial \rho}{\partial t} + \nabla \cdot (\rho \boldsymbol{u}) = 0 \tag{2-9}$$

$$\frac{\partial (\rho \boldsymbol{u})}{\partial t} + \nabla \cdot (\rho \boldsymbol{u}\boldsymbol{u}) = -\nabla p + \mu \nabla^2 \boldsymbol{u} + \rho \boldsymbol{f} \tag{2-10}$$

Where ρ is the density of the fluid (kg/m^3); $\boldsymbol{u}$ is the fluid velocity (m/s); t is the time (s); p is the pressure (N/m^2); μ is the viscosity of the fluid (Ns/m^2); $\boldsymbol{f}$ are the external volume or body forces per unit volume (m/s^2) [37].

Equation (2-9) is a partial differential equation (PDE) form of the continuity equation. For an incompressible fluids with constant density like water, $\partial \rho / \partial t = 0$, and the equation becomes div($\boldsymbol{u}$) = 0, which can also be written as $\partial u_i / \partial x_i = 0$.

Equation (2-10) is also known as Navier-Stokes equation, which is the representation of the flow motion for incompressible newton's fluid with consideration of the effect of viscosity of the fluid. Suppose that the flow is in-viscid, the dissipative, transport phenomena of viscosity, mass diffusion, and thermal conductivity can be neglected [36]. Then we have the Euler equations, which is expressed as below:

$$\frac{\partial (\rho \boldsymbol{u})}{\partial t} + \nabla \cdot (\rho \boldsymbol{u}\boldsymbol{u}) = -\nabla p + \rho \boldsymbol{f} \tag{2-11}$$

Equation (2-10) can be also expressed in a more general form by the Cauchy momentum equation, which is Cauchy's first law of motion [38]:

$$\rho \frac{D\boldsymbol{u}}{Dt} = \nabla \cdot \boldsymbol{\sigma} + \boldsymbol{F} \tag{2-12}$$

Where $\boldsymbol{F}$ is the body force (N), e.g. gravitational force, buoyancy force, centrifugal force and in some cases electric field force and electromagnetic force. σ is the Cauchy stress tensor (N/m^2), which is from the pressure distribution acting on the surface and the shear and normal stress distributions acting on the surface [36].

Equation (2-10) together can be expressed in a more general form by the conservation law of all the fluid flow, as shown in the following expression [39]:

$$\frac{\partial (\rho \boldsymbol{\phi})}{\partial t} + \mathrm{div}(\rho \boldsymbol{u} \phi) = \mathrm{div}\big(\Gamma_\phi grad \phi\big) + S_\phi \tag{2-13}$$

Where ϕ is the dependent variable, which can be scalar and vector. When ϕ is equal to 1, the conservation of mass equation can be derived. When $\boldsymbol{\phi}$ is $\boldsymbol{u}$, the equation stands for the conservation of momentum. ϕ can also be temperature, and concentration of the fluid, which means respectively heat transport and mass transport. Γ_ϕ is the appropriate coefficient for variable ϕ. In mass transport equation this coefficient can be calculated with $\Gamma_\phi = \rho D$, D is the diffusion coefficient. S_ϕ is the source-sink term.

The integral form of the conservation equation, which is the actual form solved by CFD program, is shown in the following:

$$\frac{\partial}{\partial t} \int_{CV} \rho \boldsymbol{\phi} dV + \int_A \boldsymbol{n} \cdot (\rho \boldsymbol{u} \phi) dA = \int_A \boldsymbol{n} \cdot \big(\Gamma_\phi grad \phi\big) dA + \int_{CV} S_\phi dV \tag{2-14}$$

Given the time dependent problems the transport equation can be expressed as the most generate integrated form as below:

$$\int_{\Delta t}\frac{\partial}{\partial t}\int_{CV}\rho\boldsymbol{\phi}dV+\int_{\Delta t}\int_{A}\boldsymbol{n}\cdot(\rho\boldsymbol{u}\phi)dA=\int_{\Delta t}\int_{A}\boldsymbol{n}\cdot\left(\Gamma_{\phi}grad\phi\right)dA+\int_{\Delta t}\int_{CV}S_{\phi}dV \tag{2-15}$$

2.3.3. Initial and Boundary Conditions

The initial and boundary conditions are a set of additional constraints to specify the solution of simulations. There are three kinds of boundary conditions from the mathematical point of view: Dirichlet boundary conditions, Neumann boundary conditions and Cauchy boundary conditions. Dirichlet boundary conditions prescribe the values of variables, e.g. no-slip condition, while Neumann boundary, e.g. no-penetration condition [40], conditions give values to the derivatives of variables at the boundaries. Cauchy boundary conditions specify both the function values and the derivatives of variables at the boundaries.

The simulated domain always has boundaries, where we have to set some values which imply some certain physical quantities. An improper treatment of boundary conditions can lead to an inaccurate simulation and can negatively affect the stability and the convergence speed [37]. Solid wall, inflow and outflow, symmetry and free surface are the common boundary conditions in the numerical solution of Navier-Stockes Equations. The numerical descriptions of these boundary conditions are listed in Table 2-5.

Table 2-5 Numerical description of boundary conditions

Boundary conditions	Numerical description
Solid Wall for viscous flow	$\boldsymbol{u}=0$ at the surface
Symmetry Plane [37]	$\partial\phi/\partial n=0$ $\boldsymbol{n}\cdot\nabla(\boldsymbol{u}\cdot\boldsymbol{\tau})=0$ $\boldsymbol{\tau}\cdot\nabla(\boldsymbol{u}\cdot\boldsymbol{n})=0$
Inlet [32]	$\rho,\boldsymbol{u}$ must be known as a function of position
Outlet [32]	$F_{\boldsymbol{n}}=-p$ $F_{\boldsymbol{t}}=0$ $\partial u_{\boldsymbol{n}}/\partial n=0$
Free Surface	$p=p_{atm}$ at the surface $\nabla\boldsymbol{u}+\nabla\boldsymbol{u}^{T}=0$

Where $\boldsymbol{\tau}$ denotes a vector tangential to the symmetry boundary.

2.3.4. Numerical Methods

An exact solution of these partial difference equations only exists for easy cases [41]. Appropriate numerical methods must be employed in order to solve the equations. Three main approaches for the numerical solutions are finite difference methods (FDM), finite element methods (FEM) and finite volume methods (FVM). FDM is based upon the Taylor series expansion to solve the differential form of conservation equations on a set of points. The derivatives in the differential equations are approximated by the finite differences. FEM can be regarded as a particular Galerkin form and belongs to the weighted residual methods. With this method the solution region is regarded to comprise many elements and a piece-wise approximation in terms of specified basis functions is applied to the governing equations, which means that the PDEs are replaced by either linear or nonlinear simultaneous equations [42]. FVM is based on a discretization of the integral form as shown in

equation (2-10), in which the divergence term are converted to surface integrals by using Gaussian theory.

FDM is based on the differential form of the conservation equations. There is an artificial creation or destruction of conserved variable [43] and boundary conditions [44]. But FEM and DVM are based on the integral form of the conservation equations. The key step of FVM is the integration of the partial difference equations over a control volume CV to yield a reference point [32], which means that the conservation of mass, momentum and energy are locally and globally ensured [43], resulting in an approximately 33% more accuracy than the finite difference formulation [45]. What's more, FEM and FVM are more suitable than FDM for complex geometries in multi-dimensional problems [44], because they do not require a traditional curvilinear coordinate transformation [43]. FEM equations and FVM equations can be written in unstructured grid, while FEM equations can be only written in structured grid [43].

Compared to FVM, FEM can provide a higher accuracy. However FVM have the advantages of cost reduction and algorithmic simplicity over FEM [43]. With the same model and the same mesh size, A. Cheriet et al. obtained that FVM can provide almost identical accuracy but can save more computational time and require less computer memory capacity than FEM for a 3D magneto-static problem. FEM can be regarded as a standard tool for the simulation primarily in solid mechanics, while FVM is mainly employed for numerical computations in fluid mechanics [46].

2.3.5. Turbulence Modeling

Many flows in engineering practice are turbulent. The turbulent flow shows chaotic and unstable at large the Reynolds number, while the laminar flow with Reynolds number under critical Reynolds number are relative stable. The difference between turbulent and laminar flow is that the turbulence is characterized by vortex generation, instability, irregularity, strong mixing and dissipation. Because of its random nature, the turbulent problems are always statistically treated. The time dependent properties such as velocity, pressure and temperature can be decomposed into time-averaged steady mean component with a time-varying fluctuating component [47], as shown in the following equations:

$$\boldsymbol{u} = \boldsymbol{U} + \boldsymbol{u}' \tag{2-16}$$

$$u = U + u' \tag{2-17}$$

$$v = V + v' \tag{2-18}$$

$$w = W + w' \tag{2-19}$$

$$p = P + p' \tag{2-20}$$

$$\phi = \Phi + \varphi' \tag{2-21}$$

Where $\boldsymbol{u}$ is the velocity and u, v, w are respectively its x component, y component and z component; $\boldsymbol{U}, U, V, W, P, \Phi$ are the time-averaged terms and $\boldsymbol{u}', u', v', w', p', \varphi'$ are the time-varying fluctuating components.

We use the variables above to replace the corresponding variables in the equation (2-4), (2-8) and (2-13), then we have the time-averaged continuity equation, time-averaged transport equation and time-averaged Navier-Stokes equations, which are also known as Reynolds equations. The equations are listed in Table 2-6.

Table 2-6 Turbulent flow equations

Mass conservation [32]
$\frac{\partial \rho}{\partial t} + div(\rho \boldsymbol{U}) = 0$
Reynolds equations [32]
$\frac{\partial(\rho U)}{\partial t} + \mathrm{div}(\rho U \boldsymbol{U}) = -\frac{\partial P}{\partial x} + \mathrm{div}(\mu\ grad\ U) + \left[-\frac{\partial(\rho\overline{u'u'})}{\partial x} - \frac{\partial(\rho\overline{u'v'})}{\partial y} - \frac{\partial(\rho\overline{u'w'})}{\partial z}\right] + S_{\phi x}$
$\frac{\partial(\rho V)}{\partial t} + \mathrm{div}(\rho V \boldsymbol{U}) = -\frac{\partial P}{\partial y} + \mathrm{div}(\mu\ grad\ V) + \left[-\frac{\partial(\rho\overline{u'v'})}{\partial x} - \frac{\partial(\rho\overline{v'v'})}{\partial y} - \frac{\partial(\rho\overline{v'w'})}{\partial z}\right] + S_{\phi y}$
$\frac{\partial(\rho W)}{\partial t} + \mathrm{div}(\rho W \boldsymbol{U}) = -\frac{\partial P}{\partial z} + \mathrm{div}(\mu\ grad\ W) + \left[-\frac{\partial(\rho\overline{u'w'})}{\partial x} - \frac{\partial(\rho\overline{v'w'})}{\partial y} - \frac{\partial(\rho\overline{ww'})}{\partial z}\right] + S_{\phi z}$
Transport equations [32]
$\frac{\partial(\rho\Phi)}{\partial t} + \mathrm{div}(\rho\Phi \boldsymbol{U}) = \mathrm{div}(\Gamma_\Phi\ grad\ \Phi) + \left[-\frac{\partial(\rho\overline{u'\varphi'})}{\partial x} - \frac{\partial(\rho\overline{v'\varphi'})}{\partial y} - \frac{\partial(\rho\overline{w'\varphi'})}{\partial z}\right] + S_\phi$
Turbulent kinetic energy [47]
$k = \frac{1}{2}(\overline{u'u'} + \overline{v'v'} + \overline{w'w'})$

The Reynolds averaged Navier-Stokes (RANS) equations for incompressible newton's flow can be rewritten under assumption of eddy viscosity ν_T model as:

$$\frac{\partial U_i}{\partial t} + U_j \frac{\partial U_i}{\partial x_j} = -\frac{1}{\rho}\frac{\partial\left(P+\rho\frac{2}{3}k\right)}{\partial x_i} + \frac{\partial}{\partial x_j}(2(\nu + \nu_T)\overline{S_{ij}} \tag{2-22}$$

To solve the RANS equations, the eddy viscosity ν_T must be modeled. There are several classic turbulence models, such as mixing length model, $k-\varepsilon$ model and $k-\omega$ model.

The RNG $k-\varepsilon$ model is generally believed to be more suitable for channel flow due to its capacity and accuracy for solving RANS equations at relative lower Reynolds number [47]. However it has a higher computer cost and takes more computation time [47].

Except for RANS, turbulence problem can be approached in two other ways: direct numerical simulation (DNS) and large eddy simulation (LES). When DNS is performed to simulate the flow, the computational domain must be three dimensional and all scales of motion of a flow are directly computed. DNS requires a very large computer memory capacity and takes a lot of time to simulate, which makes it in practice infeasible. LES is based on space filtered equations. In a large eddy simulation, only the large unsteady turbulent motions are directly computed. Compared to DNS, LES has a smaller computer cost, because the small scales of motions are modeled rather than directly computed.

2.3.6. Multiphase flow

There are two approaches to simulate multiphase flow: Euler-Lagrange approach and Euler-Euler approach. Euler-Lagrange Simulation treats the mixed fluid as a continuum while Euler-Euler Simulation treats the all phase of the mixed fluids as interpenetrating continua. Euler-Lagrange method tracks each particle and bubbles individually, resulting in the requirement of high performance computers and large amounts of memory [48]. Compared to the Euler-Lagrange approach, the Euler-Euler approach is more suitable and practical for the application in MBR.

Three models belong to the Euler-Euler approach: Mixture Model, Eulerian Model, and Volume of Fluid (VOF) Model. Eulerian Model is more suitable for dispersed phase where the characteristic length of the interface is smaller than the grid size [49], while VOF is a surface or gas-liquid interface

tracking technology applied to the situation where the characteristic length of the interface is larger than the grid size.

Ansys Fluent 12.0 Theory Guide recommends VOF model for slug flows, which is frequently encountered in gas-liquid flow. VOF that is first published in journal in 1981 by Hirt and Nichols [50], which can be perfectly used to predict the interface and the shape of the two fluids. The basis of the VOF Model is the volume fraction of the phase. For a gas-liquid two phase flow, the sum of the gas volume fraction and liquid volume fraction in a computer cell is equal to one.

$$\alpha_l + \alpha_g = 1 \tag{2-23}$$

Where α_l is the liquid volume fraction and α_g is the gas volume fraction. In any given cell there are three possible conditions [51]:

a) $\alpha_l = 1, \alpha_g = 0$, the cell is full with liquid, but empty of gas;
b) $\alpha_l = 0, \alpha_g = 1$, the cell is empty of liquid, but full with gas;
c) $0 < \alpha_l < 1, 0 < \alpha_g < 1$, the cell is with both liquid and gas, which can be regarded as interface of the two fluids [52].

The tracking of the interface of the two fluids is done by solving the continuity equation for the volume fraction of gas or liquid phase. For the gas phase, the equation is expressed as the following form [51]:

$$\frac{1}{\rho_g}\left[\frac{\partial(\alpha_g\rho_g)}{\partial t} + div\left(\alpha_g\rho_g\boldsymbol{u_g}\right)\right] = S_g + (\dot{m}_{lg} - \dot{m}_{gl}) \tag{2-24}$$

Where ρ_g is the density of the gas, $\boldsymbol{u_g}$ is the velocity of the gas, $S_g$is the mass source term of gas, and is equal to 0 by default. $\dot{m}_{lg}$ is the mass transfer form liquid to gas, and $\dot{m}_{gl}$ is the mass transfer form gas to liquid.

All of the properties (e.g. density and viscosity) of the mixed fluid in the domain are weighted by the volume fraction of the two fluids:

$$\rho = \alpha_l\rho_l + \alpha_g\rho_g \tag{2-25}$$

$$\mu = \alpha_l\mu_l + \alpha_g\mu_g \tag{2-26}$$

Where $\rho_l = const.$; $\rho_g = P/(RT_0)$.

The mass and momentum conservation equations can be then expressed as:

$$\frac{\partial\rho}{\partial t} + \nabla\cdot(\rho\boldsymbol{u}) = 0 \tag{2-27}$$

$$\frac{\partial(\rho\boldsymbol{u})}{\partial t} + \nabla\cdot(\rho\boldsymbol{u}\boldsymbol{u}) = -\nabla p + \nabla[\mu(\nabla\boldsymbol{u} + \nabla\boldsymbol{u}^T) + \rho\boldsymbol{f} \tag{2-28}$$

In the above equations the velocity $\boldsymbol{u}$ is a mass-averaged variable:

$$\boldsymbol{u} = \frac{\alpha_l \rho_l \boldsymbol{u}_l + \alpha_g \rho_g \boldsymbol{u}_g}{\rho} \tag{2-29}$$

On the whole, in the cells without interface regime, the governing equations are solved for the gas phase or the liquid phase respectively. However, in the cell with interface regime, the governing equations are solved for the mixed fluid. Their properties are weighted by the volume fraction of the gas or liquid fluid. And their variables (e.g. velocity, energy and temperature) are mass-averaged variables.

3. Literature review

3.1. CFD Simulation in MBRs

Membrane filtration is widely applied for water and wastewater treatment. However, the membrane performance is limited its application. The study of the factors that affect the membrane performance is necessary. One of the factors is hydrodynamics in MBR. However, monitoring and modeling of it is very difficult due to the complexities in membrane module configurations, the complex rheology of the activated sludge and the highly transient multiphase flow [48]. To investigate the flow conditions in MBR CFD is a widely used effective tool, which is more rapidly and cost effectively [53].

Table 3-1 An overview of precious studies on CFD modeling of MBRs at full scale

Literature	Module Configuration	Research Objective	Multiphase Model	Turbulence Model
Kang et al. (2008) [54]	Full-scale MBRs	Conduct CFD simulation to investigate the global hydrodynamics of MBR process at both pilot and full scale	Euler	Realizable k-ε
Wang et al. (2009) [55]	Full-scale MBRs	Evaluate the mixing and energy of MBRs with different configuration using CFD	Euler	Standard k-ε
Khalili et al. (2011) [56]	Full-scale MBRs	Evaluate the fouling of membrane surface and study the effect of the baffle angle and air flow rate on resistances	Euler	Standard k-ε
Amini et al. (2013) [33]	Full-scale MBRs	Investigate the hydrodynamic characteristics of a full-scale MBR for municipal wastewater using CFD	Euler	Standard k-ε
N. Liu et al. (2015) [57]	Full-scale MBRs	Investigate the effect of coagulant addition in MBR system on bubble induced shear stress	Euler	RNG k-ε

A large number of studies were conducted to use CFD to model MBRs systems. An overview of the previous literatures is displayed in Table 3-1 and Table 3-2. In previous studies the CFD simulation of MBRs was conducted at different scales, i.e. large-scales and small-scales. At large scale the flow dynamics such as the flow rate and the bubble size is investigated to achieve the optimum for design, operation and control in MBRs. At small scale the phenomena such as cake layer formation and shear stress on the membrane surface are studied to have a better understanding of these complicated phenomena. However a lot of studies are focused on the concentration polarization, cake layer formation [35] and spacer geometrical characteristics [58], which are not investigated in this thesis.

Table 3-2 An overview of precious studies on CFD modeling of MBRs at small scale

Literature	Module Configuration	Research Objective	Multiphase Model	Turbulence Model
Drews et al. (2010) [59]	FS	Investigate the bubble movement, aeration intensity and membrane spacing in flat sheet membrane	VOF	Not mentioned
Martinelli et al. (2010) [60]	HF	Quantify liquid circulation and shear stress at the membrane surface and investigate their effect on the cake filtration resistance	Euler-Euler & VOF	Standard k-ε

Buetehorn et al. (2011) [61]	HF	Investigate the effect of irregular fiber arrangement on the aeration efficiency to optimize the design of MBR on aeration requirements in CFD approach	VOF	RNG k-ε
Guenther et al. (2010&2012) [62, 63]	HF	Investigate the effect of packing density of hollow fiber module on fluid flow distribution and filtration performance both for outside/in (O/I) module and inside/out (I/O) module.	COMSOL multiphysics	
Lotfiyan et al. (2014) [64]	FS	Simulate the oil-in-eater emulsion microfiltration in a flat sheet module with a novel Eulerian approach	Euler	Not mentioned
Yan et al. (2015) [65]	FS	Investigate the effect of baffle configuration, location and sizes on the hydrodynamics in a flat sheet module	ANSYS CFX 14	

3.1.1. Modeling of MBRs at Full-Scale

Many studies are focused on the optimal design of MBRs system with CFD simulation. Kang et al. [54] found that the mixed liquor and air velocities could improve approximately 50% by enlarging the size of the MBR tank. Wang et al. [55] studied the effect of membrane module geometry on the mixing and energy of MBRs system at both pilot- and full-scale. It is found that HF membranes are more energy efficient compared to the FS membranes. At the same amount of permeate HF membranes required 20% less of the total energy and 50% less of the aeration energy. Furthermore, they found that the baffle in MBRs system could increase turbulence. The level of internal recirculation in the vessel with baffle was significantly higher than that in the vessel without baffle. Khalili et al. [56] made a further study of the effect of the baffle angle on the resistances, whose data had a high correlation with the shear stresses on the membrane surface. The results showed that the baffle angle from 90° to 85° increased the shear stresses, which can decrease the membrane fouling.

Other studies are conducted to achieve the optimal operation conditions in the MBR unit. Khalili et al. [56] also investigated the effect of inlet air flow rate on shear stresses. It was shown that the averaged shear stress at the membrane surface could increase by increasing the air flow rate and a better distribution of shear stress is obtained by a better distribution of air at the membrane surface. The study of diffuser configuration on the membrane performance is also carried out. Ratkovich et al. [66] studied two kinds of diffusers (ring aerator and disk aerator) in an airlift MBR system. It is observed that the disk aerator could provide a better bubble distribution in the membrane module than the ring aerator. Which also means that compared to the ring aerator, the disk aerator could provide a better mixing and a better shear stress distribution at the membrane surface.

A CFD simulation for two- and three-phase fluid in MBR was carried out by Amini et al. [33] to determine the impact of different hydrodynamic characteristics such as MLSS concentration, cross-flow velocity, aeration rate, the bubble size and the biomass phase, on the MBR performance. An agreement between the simulated results and the experimental data was achieved. It is obtained that larger bubble create lower shear stress and 3 mm is an optimal bubble size for shear stress on the membrane surface. It is also shown that the shear stress at the outmost membrane is the lowest, which makes the outmost membrane most prone to fouling and the cross-flow velocity plays a very important part in

membrane fouling control. As a result increasing the cross-flow velocity for example by inserting a baffle can minimize the membrane fouling at the outmost membranes.

Liu et al. [57] developed a CFD model coupled with an empirically determined rheology model and a porous media model to investigate the effect of the addition of coagulant on the shear stress at the membrane surface. The addition of ferrous salts was found to increase the shear stress by 12% in MBR and to improve the distribution of shear stress at the membrane surface as well. It is also observed that it was better to add the iron salts in the membrane filtration zone rather than in primary anoxic zone.

Some assumptions that should be pay attention to are made to simplify the CFD simulation of MBRs in many researches. Water instead of activated sludge mixture was used in the modeling. The density of water and sludge mixture doesn't have much difference. In terms of viscosity, water is regarded as Newtonian fluid, but a real sludge mixture is non-Newtonian fluid [67], which exhibits a different relationship between its viscosity and shear stress than Newtonian fluid. It is also found that the viscosity was at least 5 times higher than that of water [67]. As a result, sludge rheological model should be incorporated into the CFD model. However, Brannock et al. [67] also revealed that the mixing in full-scale MBR was not affected this non-Newtonian properties of activated sludge.
Other assumptions were frequently made in many studies for the gas phase, for example, the bubbles are spherical; the bubbles have a constant diameter and uniform distributions; there are no collisions, coalescence or break-up of bubbles [54]. Due to the coalescence of bubbles, the shear stress was found to disagree with all of the data from experiments over time [68]. Some models should be developed to minimize the effect of these assumptions on the simulation.

Shear stress is used in almost all of the CFD researches to indicate the filtration performance, i.e. the fouling control. Indeed, a study carried out by [56] showed that membrane fouling and permeate flux in the MBR had a close relationship with the shear stress at the membrane surface and they could be related to the shear stress of air and liquid flows. However, Ratkovich et al. [68] found that compared to the experimental data CFD simulation overestimated the shear stress induced by bubble rising. At high gas rates, the difference between the results from simulation and experiments was exceeding 20%.

In addition, the membrane was treated as rigid wall in many simulations. However in the reality the membrane especially for the hollow fiber is flexible. The movement between the fibers can scour the fouling from the membrane surface. The filtration performance of a multi-fibers module was observed to be enhanced up to 40% with account for the looseness of fibers [54].

Furthermore, the results from the pilot experiments and from the application in practice are always not the same, because some simplicities are made in the pilot study to reduce the effort, such as a pilot MBR system with less flat sheet membrane. Kang et al. [54] simulated the mixed liquor velocity and air velocity at both pilot- and full-scale MBR systems using porous medium model with consideration of the flow resistances, the vertically dependent filtration flux and the effect of MLSS on mixed liquor viscosity. Good agreement between the simulated results and the published experimental data was achieved. However, the averaged liquor velocities in the full-scale unit was found to be 50-80% lower than the results in the pilot system. And the air velocity was found to be 15-40% lower.

3.1.2. Modeling Membrane at small scale

Like the researches at large scale a lot of efforts were made to study on the optimum of geometry and operation conditions in membrane filtration at small scale. Drews et al. [59] studied the bubble movement in flat sheet membrane with different plate distances. It is found that there existed deceleration effect for bubbles caused by the walls. Small bubbles move freely due to less effect of deceleration effect. But above a certain diameter the bubbles slow down due to significant deceleration effect. However, bubble with size larger than 10 mm have an acceleration process because they can

overcome the deceleration effect. They also did a research in the effect of bubble movement, bubble size and plate distance on shear stress and found that the bubbles rising in moving water can create more than 50% shear stress than in a stagnant liquid; and increasing the bubble size can decrease or increase the shear stress, which depends on the gap distance of membrane; but shear stress decreased significantly with increasing the distance between the two plates. The optimal condition for flat sheet membrane is found to be 5 mm bubbles with a gap distance of 5 mm. Furthermore, Drews et al. [59] investigated the effect of gas velocity and cross flow velocity on flux and found an increase of critical flux as the air flow rate increases, however, a decrease in critical flux caused by an increasing in cross flow velocities. This unexpected observation can be explained by the selective particle deposition process. The larger particles are removed, but the small particles are forming the cake layer and in turn increasing a higher specific filtration resistance.

Wei et al. [69] also investigated the optimal gap width between two flat sheet in MBR systems for an industrial application. However, they found the maximal shear stress was achieved with an optimal gap distance of around 8 mm. As for the bubble size, they found that the averaged shear stress increases quickly at first, but above a certain bubble size, it starts to increase more slowly and even stops increasing.

Le Clech et al. [70] and Boehmn et al. [71] found an increase of critical flux with increasing gas flow rate. However the critical flux was not much affected by a further increase of gas flow rate above a certain velocity. Boehmn et al. [71] also found that the maximal shear stress was achieved with an effective velocity of 0.1 m/s in a 7 mm channel.

Yan et al. [65] investigated the effect of baffle configuration, location and sizes on the hydrodynamics in a flat sheet module. It is found that the baffle location and size have a significant impact on the hydrodynamics in MBR. Compared to front baffles, side baffles could create higher shear stress on the membrane surface. However, the highest shear stress was obtained with both side baffles and front baffles installed. This positive effect of using baffles to control fouling was more powerful at low aeration intensities.

Lotfiyan et al. [64] simulated the oil-in-eater emulsion microfiltration in a flat sheet module with a novel Eulerian approach with consideration of the interaction between oil droplets and the membrane. The simulated results showed a good agreement with the experimental data. The oil concentration profile is highly dependent on the trans-membrane pressure, the cake layer, feed velocity and feed concentration.

Martinelli et al. [60] used two models to simulate the fine bubble and spherical cap bubble injection in hollow fiber membrane in order to achieve a better understanding of liquid circulations and shear stress as well as their effects on the fouling resistance. They also obtained that the fouling velocity increases with increasing gas velocity, which is in contrast to the previous studies [59]. This unexpected observation was attributed to the horizontal flow induced by aeration, which results in an increase of the particle transport to the membrane surface and thus higher concentration. They also revealed that the determining parameter controlling filtration performance is the local air rate instead of the kind of bubbles, which means the filtration performance is not dependent on the kind of bubble injected. This conclusion does not agree with the conclusions achieved in a vast of other studies [20, 21, 23, 56]. They thought that a better filtration performance could be achieved with fine bubbles.

Guenther et al. (2010&2012) [62, 63] investigated the effect of packing density of the hollow fiber module on fluid flow distribution and filtration performance both for outside/in (O/I) module and inside/out (I/O) module with the finite element code COMSOL Multiphysics. It is found that the filtration flux would decrease dramatically with increasing packing density of the hollow fiber module. The numerical simulation also showed that at a large packing density the filtration velocity profile

tends to be ununiformed and the penetration rate at the bottom of the fiber is the highest, which leads to uneven particle deposition and thus non-uniform cake formation along the fiber height. The cake layer height increased along the fiber at a low packing density. However, at the high packing density, it shows an inverse particle deposition pattern. As for a moderate packing density, it has a higher filtration flux and relatively more homogenous axial flux profile.

In most of the studies the fiber arrangement was considered as regular. Only a few studies investigated the impact of the irregular arrangement of the hollow fibers on the flow conditions. Buetehorn et al. [61] investigated the irregular arrangement of hollow fibers in bundles and an anisotropic resistance was found to expose to the flow. They developed a method to implement this resistance into CFD model by porosity and friction factor. It is shown that the cross flow velocity distribution and the turbulent viscosity distribution were highly dependent on the local fiber arrangement.

Beyond these reviewed researches, a lot of efforts also were made to study the problems of concentration polarization, cake layer formation [35] and spacer geometrical characteristics [58]. However, they are not discussed in this thesis.

3.2. CFD Simulation for Gas-liquid Flow

Aeration on the one hand can provide necessary oxygen biomass and keep them not to settle down; on the other hand can scour the solid from the membrane surface to control the growth of cake layer by creating turbulence. It is regarded as the most important process, but also the highest energy consumed process in the MBR system. As a result, a lot of efforts were made to optimize the aeration condition in MBR module by studying on the gas flow rate, the bubble size and the bubble distribution and son on. These researches were already reviewed in the above section. In this section the review of CFD simulation for gas-liquid flow is not just limited in MBR system. And the effect of size distribution, break-up and collisions, coalescence of bubbles is also discussed in this section. An overview of the previous studies on CFD simulation of gas-liquid flow is listed in Table 3-3.

Table 3-3 An overview of previous studies on CFD simulation of gas-liquid flow

Literature	Module Configuration	Research Objective	Multiphase Model	Turbulence Model
Taha et al. (2006) [72]	Inclined tubular membrane modules	Investigate the slug flow dynamics and their effect on ultrafiltration performance	VOF	Laminar flow
Ratkovich et al. (2009) [68]	Vertical tubular membrane	Investigate the effect of slug flow on the shear stress numerically and experimentally	VOF	RNG k-ε
Drews et al. (2010) [59]	FS	Investigate the bubble movement, aeration intensity and membrane spacing in flat sheet membrane	VOF	Not mentioned
Wei,P et al. (2013) [69]	FS MBR	Simulate the properties of a single bubble rising in FS membrane channel and investigate the effect of bubble size and the gap distance on the wall shear stress.	VOF	Realizable k-ε

Slug flow plays an important part in two-phase flow regimes in terms of permeability enhancement in the MBR system [70]. In slug flow, when the gas slug rises, the direction of the liquid flow changes, which creates shear stress, as suggested by Ratkovich et al. [68].

Taha et al. [72] undertook a numerical study to investigate the slug flow dynamics and their effect on ultrafiltration performance in the inclined tubular membrane. It is obtained that only the fluid below the Taylor bubble is affected and there existed a mixing zone, whose length was found to be related to the inclined angles of the tubular membrane.

Wei et al. [69] simulated the properties of a single bubble rising in FS module for industrial application with VOF model. The simulated spherical cap shape showed a good agreement with the experimental observation. They also investigated the effect of bubble size and the gap distance on the wall shear stress. It is shown that in the wake region behind the slug bubble, the mass transfer is more intensive enhanced than in the region around the bubble.

Ratkovich et al. [68] investigated the effect of slug flow on the shear stress. It is found out that the slug flow was in transitional regime, which is a regime between laminar and turbulent condition. A periodic slug bubbling was found to be able to provide a better hydrodynamics than free bubbling. A bi-model distribution of shear stress was also found from the experiments: a positive surface shear peak caused by the liquid slug and a negative shear peak exerted by the gas slugs [68]. It is also shown that the coalescence of bubbles affected the shear stress significantly, leading to the numerical results varying against all of the experimental data over time. However, Drews et al. [59] suggested that the calculated shear stresses could be trusted because their numerical results showed good agreement with the bubble shape observed by experiment.

Nearly all the CFD simulation of gas-liquid flow in MBR systems were used a constant bubble size instead of bubble size distribution to simplify the simulation. However, in MBR system the bubble size has a wide distribution during operation. And the bubble size has a great influence on the bubble behavior. The population balance model (PBM) which can be coupled into the CFD, is turned out to be an effective approach to predict the bubble size distribution. Wang et al. [73] developed a CFD-PBM coupled model with consideration of bubble break up and coalescence, which was able to predict the hydrodynamics in complex flow regime. It is found that at a low gas flow rate the bubbles were small and had a narrow size distribution and a relative uniform gas hold-up profile. With increasing gas low rate, the effect of bubble coalescence became stronger and a lot of large bubbles were formed. Wang [74] used this CFD-PBM coupled model to simulate the bubble columns reactors to investigate the fundamental hydrodynamic characters in it. The simulated bubble size distribution and gas hold up for bubble columns both in the homogeneous and heterogeneous regime showed good agreement with operating data.

3.3. Rheology of the MBR Sludge

Activated sludge is a very complex mixture, which includes mainly water, microorganism and nutritious substances for them, for example, organic carbon, nitrate etc. and some substances produced by them such as EPS. Due to its complex composition, the rheological behavior of activated sludge is much more complicated than that of water. Despite that, viscosity which is thought to have a great influence on the hydrodynamics in the bioreactor, oxygen transfer and membrane filtration performance, is a very important property of activated sludge. A lot of studies have carried out on this topic [75-77].

Viscosity can indicate the flow-ability of a fluid and has a great influence on the hydraulic regime and transport phenomena. It is affected by the temperature. When the temperature is high, the molecules are less strongly bound to each other and can more freely move. As a result the fluid is more flowable and the value of viscosity is lower. Viscosity is defined by the following equation [78]:

$$\mu = \frac{\tau}{\dot{\gamma}} \tag{3-1}$$

Where τ is the shear stress (Pa) and $\dot{\gamma}$ is the shear rate (s^{-1}).

For a Newtonian fluid, the relationship between shear stress and shear rate is linear, which means that the viscosity is constant. However, for non-Newtonian fluids, the relationship is non-linear, which means that the viscosity depends on the shear rate. This viscosity for non-Newtonian fluid is referred to as apparent viscosity [78]. A lot of studies were undertaken to predict the apparent viscosity of activated sludge. An overview of the rheological model is exhibited in Table 3-4.

Table 3-4 Overview of rheological model of activated sludge in previous studies

Literature	Model
Krauth et al. (1993) [79]	$\mu = \mu_w \cdot 1.044625 \cdot e^{0.081151MLSS}$
Laera et al. (2007) [76]	$\mu = \frac{28.939MLSS}{\dot{\gamma}} + 0.233MLSS + 1$ Bingham model
	$\mu = e^{0.822MLSS^{0.494}} \cdot \dot{\gamma}^{(-0.050MLSS^{0.631})}$ Ostwald model
Yang et al. (2009) [75]	$\mu = 1.0024 \cdot MLSS^{1.644} \cdot T^{-0.206}$
	$\mu = 32.36MLSS^{1.359} \cdot \dot{\gamma}^{-0.807}$
	$\mu = 0.0126 \cdot MLSS^{1.644} \cdot e^{9.217/R_g(T+273.15)}$
	$\tau = \tau_0 + K\dot{\gamma}^n$ Herschel-Bulkley model
	$\tau = ({\tau_0}^{0.5} + K_C\dot{\gamma}^{0.5})^2$ Casson model
Garakani et al. (2011) [77]	$\tau = K\dot{\gamma}^n$ Power law or Ostwald model
	$\tau = \tau_0 + \mu_p\dot{\gamma}^n$ Bingham model
	$\mu = 5.7 \times 10^{-6} \cdot \frac{MLSS^{1.5}}{U_{Gr}}$ $(\dot{\gamma} = 5000U_{Gr})$
	$\mu = 4.05 \times 10^{-4} \cdot MLSS^{1.5} \cdot e^{-7.7/R_g(T+273.15)}$
	$\mu = 2.86 \times 10^{-2} \cdot \frac{MLSS^{1.5}}{U_{Gr}} \cdot e^{-7.7/R_g(T+273.15)}$ $(\dot{\gamma} = 5000U_{Gr})$

Where R_g is the universal gas constant (8.3145 $JK^{-1}mol^{-1}$); T is the temperature (°C); U_{Gr} is the gas velocity (m/s); K, K_C, μ_P, μ_w are constants.

From the above equations, we know that, the viscosity of the fluid mixture is not only affected by the MLSS concentration in the MBR system, but also affected by the aeration rate. The viscosity of Newtonian fluid and the apparent viscosity of non-Newtonian fluid have a huge difference. A lot of studies were carried out to compare the hydrodynamic results of MBR systems with water and activated sludge [67, 69, 71].

Boehmn et al. [71] undertook a study on the shear stress in both water and non-Newtonian fluid. He found that the fluctuation of shear stress, which is thought to be good for fouling control, is stronger in water than in non-Newtonian fluid. However the effect of rheology of the mixture is minor in the MBR system. Wei et al. [69] compared the averaged shear stress of bubbles in water and in activated sludge to estimate the effect of viscosity and surface tension on the shear stress. It is found out that the activated sludge viscosity was minor. The shear stress was slightly increased (2.9%), even when the viscosity increased by 10.7%. Brannock et al. [67] coupled the HBP model (the Herschel-Buckley relationship with Papanastasiou's adaption) into CFD to investigate the effect of the activated sludge rheology on the hydrodynamics in the MBR system and found that the effect was small compared to the turbulent viscosity in high energy systems such as MBR systems. On the other hand, the use of the coupled HBP model in the CFD model requires a lot of computational resources. As a result, water can be used for the CFD simulation of MBR systems.

3.4. ASM-CFD Model for MBRs Simulation

CFD can simulate the hydrodynamic characteristics in MBR system, while ASM model (Activated Sludge Model) can simulate the biological reaction. The description of the processes of the ASM model is summarized in Table 3-5.

Table 3-5 Description of the processes of the ASM model (adopted from [80])

Description	Kinetics expression	Notation
Aerobic growth of heterotrophic biomass	$\rho_1 = \mu_H(\frac{S_S}{K_S+S_S})(\frac{S_O}{K_{O,H}+S_O})X_{B,H}$	ρ_1 Process equation for process 1 μ_H Growth rate for heterotrophic biomass S_S Soluble biodegradable pollution $K_S, K_{O,H}$ half-velocity constant S_O Dissolved oxygen $X_{B,H}$ Heterotrophic biomass
Anoxic growth of heterotrophic biomass	$\rho_2 = \mu_H\eta_g(\frac{S_S}{K_S+S_S})(\frac{K_{O,H}}{K_{O,H}+S_O})(\frac{S_{NO}}{K_{NO}+S_{NO}})X_{B,H}$	η_g correction factor for μ_H under anoxic condition S_{NO} Nitrate and nitrite K_{NO}half-velocity constant
Aerobic growth of heterotrophic biomass	$\rho_3 = \mu_A(\frac{S_{NH}}{K_{NH}+S_{NH}})(\frac{S_O}{K_{O,A}+S_O})X_{B,A}$	μ_A Growth rate for autotrophic biomass $X_{B,A}$ Autotrophic biomass S_{NH} Ammonium
Decay of heterotrophic biomass	$\rho_4 = b_H \times X_{B,H}$	b_H specific decay rate for heterotrophic biomass
Decay of autotrophic biomass	$\rho_5 = b_A \times X_{B,A}$	b_A specific decay rate for autotrophic biomass
Ammonification	$\rho_6 = k_a \cdot S_{ND} \times X_{B,H}$	k_a Ammonification rate S_{ND} Soluble organic nitrogen
Particulate biodegradable pollution hydrolysis	$\rho_7 = k_h\left(\frac{\frac{X_S}{X_{B,H}}}{K_X+\frac{X_S}{X_{B,H}}}\right)\left[\left(\frac{S_O}{K_{O,H}+S_O}\right)+\eta_h\left(\frac{K_{O,H}}{K_{O,H}+S_O}\right)\left(\frac{S_{NO}}{K_{NO}+S_{NO}}\right)\right]X_{B,H}$	k_h Maximum specific hydrolysis rate X_S Particulate biodegradable pollution η_h correction factor for hydrolysis under anoxic condition
Particulate organic nitrogen hydrolysis	$\rho_8 = \frac{X_{ND}}{X_S}\rho_7$	

Incorporating ASM model into CFD can optimize the hydrodynamic conditions to achieve an effective removal of pollutants in the bioreactor. A lot of studies have been undertaken to couple the two models. An overview of the previous researches on this topic is displayed in Table 3-6. In many studies the author coupled the biological model can be coupled into CFD model through the following equation [81]:

$$\frac{\partial(X_{species})}{\partial t} + \mathrm{div}\left(\boldsymbol{u}X_{species}\right) = \mathrm{div}\left(\Gamma_t grad X_{species}\right) + S_{species} \quad (3\text{-}2)$$

Where $X_{species}$ is the mass fraction concentration of the species; Γ_t is the turbulent diffusion factor and $S_{species}$ is the source and sink term caused by the biological reaction.

Table 3-6 An overview of the previous studies on the ASM-CFD model

Literature	Bioreactor type	Kinetic model
Brannock (2003) [81]	Mixed anoxic wastewater treatment vessels	Simplified ASM-1 Model
Moullec et al. (2010) [82]	Activated sludge channel reactor	ASM-1 Model
Moullec et al. (2011) [80]	Activated sludge reactor	ASM-1 Model

In an early study carried out by Brannock [81] the simplified ASM-1 model was used to incorporate into CFD model to simulate the biological and hydrodynamic characteristics in a mixed anoxic wastewater treatment vessels. The CFD simulated removal rates showed only 10% error against the experimental data. Moullec et al. [82] used the CFD model coupled with ASM-1 model to simulate the COD (Chemical Oxygen Demand) concentration profile, the oxygen concentration profile, the nitrate concentration profile and ammonium concentration profile in an activated sludge channel reactor. Only the simulated and experimental values of nitrate concentration and COD concentration showed good agreement. Moullec et al. [80] compared the experimental and simulated results and found that the predictions of nitrate concentration, oxygen concentration and COD concentration were reasonable. However the prediction for ammonium is not reasonable.

There are not so many studies on this topic at the moment. However, it is predicted that more and more researchers will study on this.

4. Modeling

In this chapter the software FLUENT in combination with ANSYS ICED MESH and CFD-POST, which are a commercial computational fluid package, is used for the simulation. Because of the computational cost it is impossible to simulate the whole membrane in one modeling. So the modeling is divided into three parts. Each part has a different mission and therefore a different geometry and mesh grid sizes.

The first part of the model is the formation of a single bubble. In this part the shape and the velocity of the bubble will be calculated. The second part is to simulate the motion of a single bubble rising in the membrane channel. The diameter of the single bubble is based on the results of the first part. The velocity and the shear stress distribution along the membrane will be numerically studied. The last part of the modeling is a numerical study of the bubble running out of the membrane. The shearing force will be calculated.

VOF method with constant surface tension and turbulent method (RNG k-ε Model) will be used for all of the parts to simulate the multiphase fluid (air/water). The geometric reconstruction scheme will be applied to the reconstruct the interface of gas and liquid phases. The PISO (pressure implicit with splitting of operators) scheme is chosen for the pressure-velocity coupling, because it is good for the calculations and convergence improvements of transient flow [69]. For the spatial discretization the following schemes are used to improve the calculation quality and accuracy. The Body Force Weighted scheme is chosen for the pressure and QUICK scheme are chosen for momentum, turbulent kinetic energy and turbulent dissipation rate.

4.1. Assumptions and Simplifications

Like in many other studies, some assumptions are made to simplify the problem. Otherwise, it will be a highly computational resource and time consuming. However unreasonable assumptions will increase the risk of deviation between the real situation and the numerical results. The following assumptions that are made in this thesis also can be found in many other researches.

a) Assumptions for bubble simulation
   It is a single bubble that is simulated in this study. So the effect of collisions, coalescence or break-up of bubbles can be neglected. However the bubble that is used in the last two parts is considered as a spherical bubble with a constant diameter.
b) Assumptions for the membrane
   In the reality the membrane is flexible. Despite the fact that the movement of membrane can scour the fouling from the membrane surface, the membrane is treated as a rigid wall in this simulation. In the further work the effect of the membrane movement will be studied.
c) Assumptions for the liquid phase
   Water instead of the activated sludge mixture was used in the first part of the modeling. It is believed that the density of water and sludge mixture doesn't have much difference. In terms of viscosity, water is a Newtonian fluid, and a real sludge mixture is non-Newtonian fluid, which exhibits a different relationship between its viscosity and shear stress than Newtonian fluid. So a liquid which has the same viscosity as the activated sludge in the membrane reactor will be used for the other parts of modeling.

All of the assumptions are made in order to reduce the computational cost and shorten the time.

4.2. Bubble Formation in 2D

In this section the simulation is focused on the bubble formation. The shape and the velocity of the bubble are of interest. What's more, the effect of some parameters like pressures and viscosity will be researched.

4.2.1. Model Geometry and Boundary Conditions

The domains were drawn with Design Modeler and the structured meshes were generated by Meshing [ANSYS ICEM CFD]. Two computational domains were created with different dimensions of the inlet. The dimension of the larger inlet is 0.6×2 mm. And the other one is 0.2×2 mm. The other part of the two domains is same. It's 8 mm wide and 20 mm high. The detailed information about the geometry and the mesh is presented in Figure 4.1.

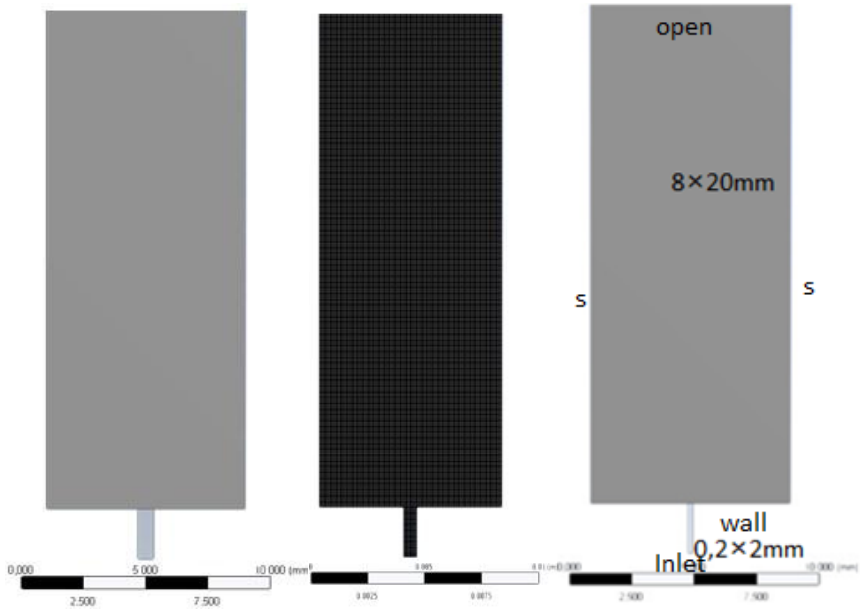

Figure 4.1 Sketch of geometry and mesh for 2d model (from left to right: Domain with larger inlet; Mesh of the domain with larger Inlet; Domain with small Inlet)

To form a single bubble, the inlet is set to be velocity-inlet with a velocity of 15 m/s in 0.003 s. The left and right boundaries are set to be symmetry to minimize the wall effect. Specified settings of boundary conditions are listed in Table 4-1. The operating pressure is 101325 Pa and the operating density is 1.225 kg/m. The simulation is with gravity in Y direction. For the domain with a bigger hole, the velocity was set to be 5 m/s and the time of aeration is 0.003 s, so that the amount of both situations are still the same.

Table 4-1 Boundary conditions settings

ID	Boundary Conditions
Inlet	Velocity-inlet with a velocity of 15 m/s and time of 0.003 s for the small inlet, and for the bigger inlet the velocity is 5 m/s and last for 0.003 s
Open	Pressure-outlet with very small turbulent intensity to make sure that the turbulence there don't have much influence
S	Symmetry
Wall	No slip Wall with constant surface tension and wall adhesion

4.2.2. Independence Test

The numerical results are highly dependent on the grid. Coarse grids may lead to wrong results. Fine grids on the other hand can cost too much computational resource and time. An appropriate grid size is very important to the simulation. With the grid independence test the maximal allowed element size can be found when a certain results remain constant with a grid size smaller than it. Four types of meshes with different element sizes are applied to the independence test. A summary of mesh sizes and numbers is displayed in Table 4-2.

Table 4-2 Summary of mesh sizes and numbers

Mesh	Element size	Grids number
Mesh 1	0.00005 m	64000
Mesh 2	0.0001 m	16000
Mesh 3	0.0002 m	4000
Mesh 4	0.0004 m	1000
Mesh 5	0.00002 m	400000

To test the mesh independence the shapes of the bubbles compare with different mesh element size in Figure 4.2. It's observed that the interface between two phases becomes sharper and sharper with decreasing element size. The result with the finest mesh is the most accurate. However, given the time and computational resource it is not used in this thesis. Instead Mesh 1 is used for the calculation in 2d Model. Because the interface between the gas and liquid is in the Mesh 1 already sharp enough. Mesh 1 is applied to the simulation normally to get a better visual effect.

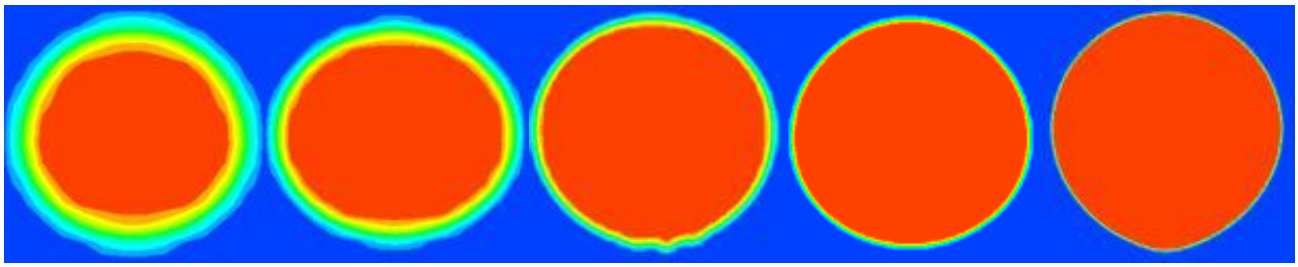

Figure 4.2 Snapshot of bubble obtained from different Meshes (from left to right: Mesh4, Mesh3, Mesh2, Mesh1, Mesh5)

The bubble terminal velocity is also a very good parameter, which can be used to indicate the mesh structures. However the domain in this phase is too small to achieve the terminal velocity. Instead of the terminal velocity the velocity of different mesh structures is compared and plotted against the flow time in Figure 4.3. In the following figure a huge difference between the result of Mesh4 and the results of the other meshes can be obtained. The deviation of the results from the other three meshes is very small and acceptable. It is concluded that good results can be achieved with the mesh element size of 0.0002 m.

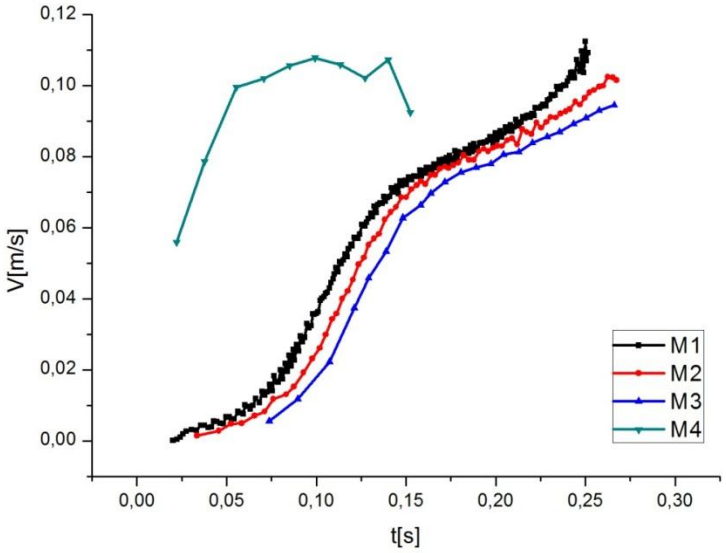

Figure 4.3 Mesh independence test using velocity

The bubble aspect ratios E, which can indicate the deformation of the single bubble, is defined as the maximal vertical dimension divided by the maximal horizontal dimension [26]. It's also used as an Indicator to analyze the sensitive of mesh structures. It's similar with the velocity. When the condition is relatively stable, a terminal E can be achieved. However, the terminal velocity is not yet obtained. So it's believed that the relatively stable condition is not achieved in the domain. Similar with the velocity, instead of the terminal E the aspect rations of different mesh structures are compared and plotted against the flow time. The results are shown in Figure 4.4.

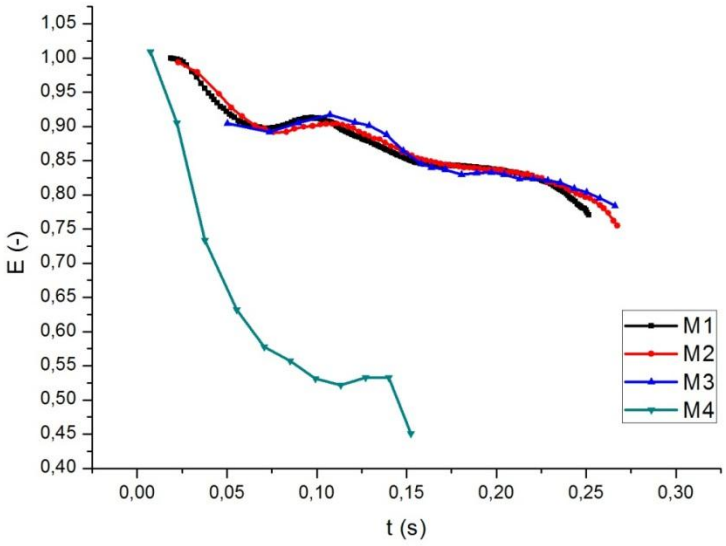

Figure 4.4 Mesh independence test using bubble aspect ratios

The results of bubble aspect ratios are similar to the results of velocity. A huge difference between the result of Mesh4 and the results of the other meshes can be obtained from the above figures. The deviation of the results from the other three meshes is very small and acceptable. It is concluded that the result is no longer dependent on the grid element size when the size is smaller than 0.2 mm.

It is known from the mesh independence test that the effect of the grids can be neglected, when the element size is below 0.0002 m. The mesh size of 0.2 mm can be used for simulation inspect of velocity and bubble aspect ratios. However to achieve a better visual effect a smaller size, e.g. Mesh 1 is also used in the following study in 2d model.

4.3. Bubble Formation in 3D

In this section the simulation is also focused on the bubble formation. However the simulation is in a 3 dimensional model carried out. The shape and the velocity of the bubble will be investigated in this section as well. Due to the high cost of computational resource and time, the influence of the parameters, e.g. pressure and temperature will not be studied in a 3d model. Out of the same reason the independence test will not be carried out in 3 dimensional simulations either. 0.0001 m will be chosen for the mesh element size and it can be known from the last section that the element size of 0.0001 m has been already fine enough.

4.3.1. Model Geometry and Boundary Conditions

In order to compare the results from the 2d simulations two computational domains were created with different inlets. The dimension of the larger inlet is 0.2×1.6×1 mm. And the other one is 0.2×0.2×1 mm. The other part of the two domains is same. It's 8 mm long, 8 mm wide and 20 mm high. The domain is presented in Figure 4.5. All of the meshes are hexahedron. At the top of the model air is patched and the bubble can be formed because the air is given through the inlet.

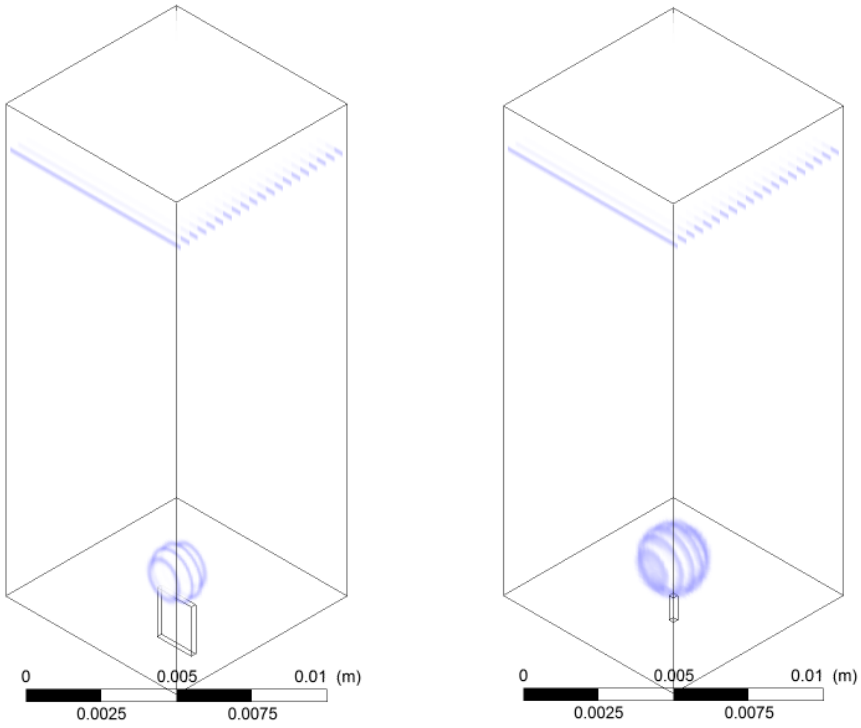

Figure 4.5 Sketch of geometry for 3d model: Domain with larger inlet (left); Domain with small Inlet (right)

To form a single bubble, the large inlet is set to be velocity-inlet with a velocity of 3 m/s in 0.04 s. In order to have the same dimension of the to be formed bubble the inlet velocity of the domain with smaller inlet is set to be 3 m/s in 0.32 s. The vertical boundaries are set to be symmetry to minimize the wall effect. Specified settings of boundary conditions are listed in Table 4-3. The operating

pressure is 101325 Pa and the operating density is 1.225 kg/m. And the simulation is with Gravity in Y direction.

Table 4-3 Boundary conditions settings

ID	Boundary Conditions
Inlet	Velocity-inlet with a velocity of 1 m/s
Open	Pressure-outlet with very small turbulent intensity to make sure that the turbulence there don't have much influence
S	Symmetry
Wall	No slip Wall with constant surface tension and wall adhesion

To investigate the effect of the inlet dimension on the bubble size the velocity at the inlet for both models was set to be 3 m/s. And to study the relationship between the inlet velocity and the bubble size the velocity were set to be 1 m/s, 2 m/s and 3 m/s respectively in the model with larger inlet. The other boundary conditions stay the same.

4.4. Bubble Motion in MBR Channel in 2D

In the second phase is the modeling of bubble motion in MBR channel. In this section the relationship between bubble rising velocity and shear stress will still be investigated. Some results from last phase will be used. The whole domain, rather than only part of it will be simulated. However, considering the computational time, mesh grid independence test, which is already studied before, will not be carried out in this section. And the mesh element size of 0.0002 m will be chosen, since a relative good result can be obtained with this element size. And it is already known from mesh grid independence test for 2d model in the last section that the derivation of the results from the mesh element size of 0.0002 m is acceptable.

To get a whole understanding of the bubble motion, the simulation in 2d model in this section will not be divided into bubble motion and bubble run off. On the other hand, the bubble formation in a 2d model takes a lot of time and requires huge computational resources. So instead of simulating the bubble formation from the nozzle a single bubble is patched in the water.

4.4.1. Model Geometry and Boundary Conditions

The model and the meshes were produced by the commercial software package ANSYS. The domain for the simulation is 0.008×0.66 m. The length of the membrane is 0.5 m, which is identical with the Experiment Set-up. A sketch of the model is displayed in Figure 4.6. A single bubble with the diameter of 2 mm is patched at the position of 3 mm above the bottom. At the top of the domain is air as well. The thickness of this region is 10 mm. The membrane, which is represented by the blue line, is set to be no-slip wall. The other vertical boundaries were set to be symmetry, so that the simulation in this area will not be affected by the wall. The top boundary of the domain is pressure-outlet, where only air can go through.

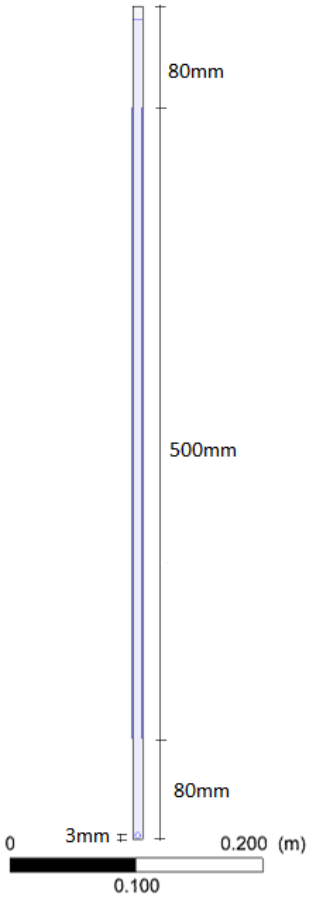

Figure 4.6 Sketch of the 2d model for the simulation of bubble motion

In this section the relationship of the wall shear stress and the other parameters is studied. In order to get a reliable value of wall shear stress y^+ is applied to indicate if the meshes are fine enough to solve the boundary layer. Two kinds of meshes are compared in this section. One of them is structured grid with the element size of 0.2 mm. The other one is an unstructured grid with finer element size near the wall. A sketch of the two kinds of meshes is displayed in Figure 4.7.

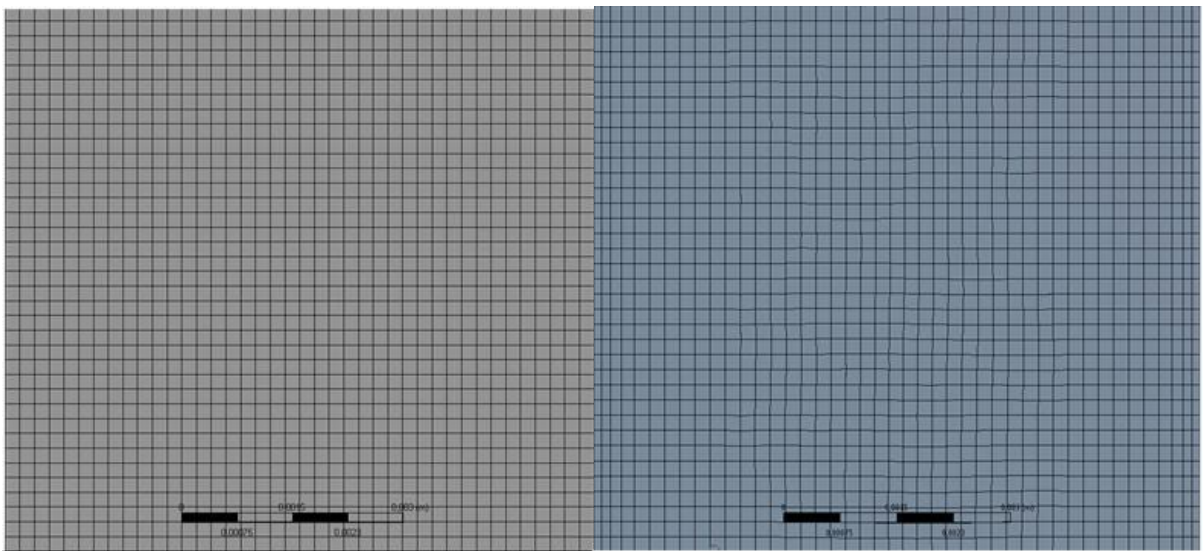

Figure 4.7 Sketch of meshes for 2d model (left: structured grid; right: unstructured grid with finer element size near the wall)

y^+ is a very important indicator for different turbulence model. RNG k-ε Model with enhanced wall treatment is applied for the simulation. This model guarantees the modeling results for small and large y^+ cases. If the y^+ falls in the $3<y^+<30$ region, also called buffer region, the reasonable representation can be obtained through this model. However the results are not certain to be correct. So the y^+ value should be less than 3 or greater than 30 for the application of the model. In order to make sure the y^+ lies in the reliable region, the element size near the wall can be manipulated. The following table shows the results of the model with two different meshes as shown above.

Table 4-4 Comparison of results from model with structured and model with finer grid at the first layer

Parameters	Structured grid	Unstructured grid with finer element at the first layer
Averaged y^+	0.1337	0.0655
Max. y^+	6.8316	4.0222
Bubble rising velocity [mfs]	0.0837	0.0829
Max. shear stress [Pa]	4.7035	6.5218
Time averaged shear stress on the left membrane [Pa]	1.2250	1.4763
Time averaged shear stress on the right membrane [Pa]	1.4706	1.4509

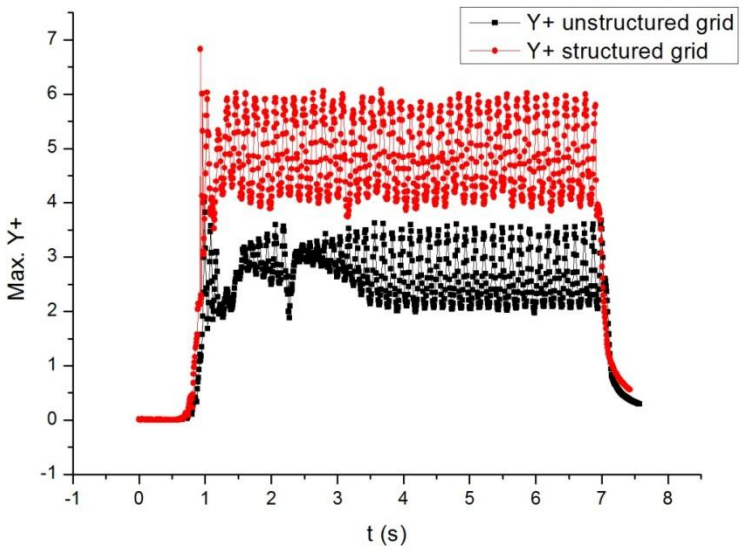

Figure 4.8 Max. $y+$ for both models (red: structured grid; black: unstructured grid with finer element size near the wall)

From the table above, we can see that the maximal y^+ for both models lies in the buffer region (3-30). However, the average y^+ value for both models are much smaller than 3 and y^+ is even smaller when the first layer is thinner. Since both the averaged and the maximal y^+ for the model with finer element size at the first layer are less than the y^+ for the model with structured grid, the modeling result with structured grid is considered to be worse than the other one. Besides, the majority of the maximal y^+ obtained from the model with structured grid are above 3. On the contrary, the majority of the maximal y^+ of the other model is below 3, which is shown in Figure 4.8. So it is recommended to use the results obtained from the model with a finer grid at the first layer because it is believed to be more reliable. However, except for the maximal shear stress the other parameters obtained respectively from both models are pretty much the same. The reason for the huge difference in maximal shear stress

probably is that the y^+, when the maximal shear stress occurs, lies in the buffer region. So the maximal shear stresses for both cases are not reliable. To be concluded the results from both models are about the same and the model with a finer grid near the wall is slightly better. However, both models may be not reliable when it comes to the maximal shear stress and the model with finer element size at the first layer may lead to more reliable results.

4.5. Bubble Rising in MBR Channel in 3D

Bubble motion in MBR channel is also simulated in this section. Compared to the simulation in the last section the simulation in this section is 3 dimensional. The shape and the velocity of the bubble will still be investigated in this section. But most importantly the shear stress and its affecting parameters will be studied. The initial velocity and the bubble diameter are chosen based on the results from last sections. Unlike the 2d model and due to the high cost of computational resource and time, the domain for 3d model is smaller will be chosen and tested to ensure that it is large enough to carry out the modeling. Then the mesh element size independence will be also analyzed.

4.5.1. Model Geometry and Boundary Conditions

The domains for 3d Modell were also drawn with Design Modeler and the meshes were generated by Meshing [ANSYS ICEM CFD] as well. To reduce the computational cost only a part of the domain was chosen. However the geometry of the domain can affect the numerical results greatly. In addition, the numerical result is also dependent on the mesh size. So before the simulation is carried out, we have to find the appropriate domain and the mesh size of the simulation. In order to find the optimal domain and the optimal mesh for the simulation different domains and different mesh elements are applied to test the mesh and geometry independence. A sketch of one of the domains is shown in Figure 4.9.

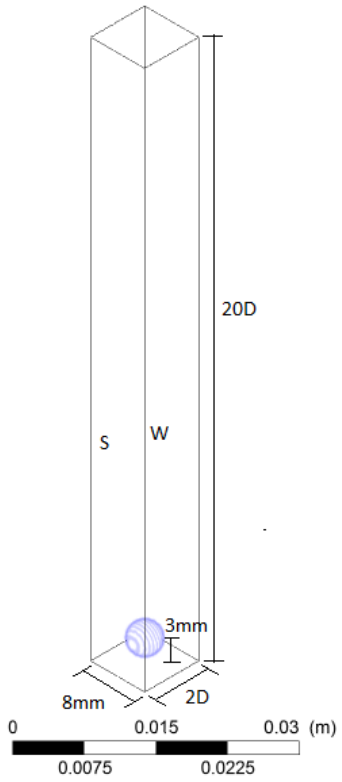

Figure 4.9 Sketch of the one of the domains

To test the effect of the length of the domain, the length of the domain is variable. However the width and height of the domain fixed which are set to be 8 mm and 20D respectively. D is the diameter of the bubble patched in the domain and the bubble diameter is chosen as 4 mm. The initial position of the bubble is 3 mm above the bottom. The other settings of the different cases are the same. The detailed information about the domains which are applied for different cases can be found in Table 4-5.

Table 4-5 Domains used to test the effect of the length

Cases	Width	Length	Height	Bubble Size	Mesh Size
Case 1	8 mm	1.5D	20D	4 mm	0.2 mm
Case 2	8 mm	2D	20D	4 mm	0.2 mm
Case 3	8 mm	3D	20D	4 mm	0.2 mm
Case 4	8 mm	4D	20D	4 mm	0.2 mm
Case 5	8 mm	5D	20D	4 mm	0.2 mm

The effect of the height of the domain was also analyzed. In the analyses the height of the domain is variable and the other conditions are fixed. The boundary conditions stay the same as that for the length test. All the domains used for the height independence test are displayed in Table 4-6.

Table 4-6 Domains used to test the effect of the height

Cases	Width	Length	Height	Bubble Size	Mesh Size
Case 1	8 mm	2D	10D	4 mm	0.2 mm
Case 2	8 mm	2D	15D	4 mm	0.2 mm
Case 3	8 mm	2D	20D	4 mm	0.2 mm
Case 4	8 mm	2D	25D	4 mm	0.2 mm

Apart from the domain geometry the mesh size can also affect the numerical results greatly. An optimal grid size is looked for this simulation on the one hand to save the computational time and resource, on the other hand to guarantee the quality of the results. Three different mesh sizes are applied to the independence test. A summary of mesh sizes and the domain used for the mesh independence test is listed in Table 4-7.

Table 4-7 Domains used for mesh independence test

Meshes	Width	Length	Height	Bubble Size	Mesh Size
Mesh 1	8 mm	2D	20D	4 mm	0.4 mm
Mesh 2	8 mm	2D	20D	4 mm	0.2 mm
Mesh 3	8 mm	2D	20D	4 mm	0.1 mm

For the simulation in this phase not all of the vertical boundaries are set to be symmetry to minimize the wall effect. The vertical planes which stand for the membranes are set to be no slip wall because the wall shear stress is investigated with this model. The plane at the top of the domain is set to be Pressure-outlet. In this region the pressure is set to be the atmospheric pressure. Unlike the settings in the 2 dimensional models only water allowed to go through the boundary. Specified settings of boundary conditions are listed in Table 4-8.

Table 4-8 Boundary conditions settings for the simulation of bubble motion

ID	Boundary Conditions
Open	Pressure-outlet with very small turbulent intensity and only water is allowed to go out
S	Symmetry
W	No slip Wall with constant surface tension and wall adhesion

To investigate the effect of the bubble size on the bubble motion and shear stress. Different sizes of bubble are applied for the simulation. The domains for this simulation are chosen based on the results of the geometry and mesh size independence test in order to minimize the effect of the geometry of the domain and the mesh sizes, so that a plausible result can be obtained. The detailed information about the domains which are used to study the effect of bubble sizes is displayed in Table 4-9.

Table 4-9 Domains used to study the effect of bubble sizes

Cases	Width	Length	Height	Bubble Size	Mesh Size
Case 1	8 mm	5D	20 mm	2 mm	0.2 mm
Case 2	8 mm	5D	30 mm	3 mm	0.2 mm
Case 3	8 mm	5D	30 mm	4 mm	0.2 mm
Case 4	8 mm	5D	30 mm	5 mm	0.2 mm

To investigate the effect of the parameters, e.g. pressure, temperature and viscosity on the shear stress a domain of 8 mm×8 mm×80 mm is used. Considering the trend of these parameters are more interesting and a better experimental result can be achieved with the small model, so a small domain of the model is applied to assess the effect of these parameters. In the domain a single bubble with the diameter of 4 mm is patched at the position of 3 mm above the bottom. The meshes are hexahedron with a size of 0.2 mm. The settings stay the same. Only the parameter, which is studied, is variable.

The distance between two plates has certainly great effect on the velocity profile and shear stress profile. Different gap distances are set in the model to investigate this effect. Considering the length effect on the simulation, the models in the following table were applied to study the effect of different gap widths of the membranes. All of the results will be compared and the best result will be used.

Table 4-10 Additional models used to study the effect of gap distances

Gap distances	Width	Length
6 mm	20 mm	6 mm
7 mm	20 mm	7 mm
8 mm	20 mm	8 mm
9 mm	20 mm	9 mm

4.5.2. Independence Test

The independence test was carried out regarding the length of the domain, the height of the domain, and the mesh size of the model. The models which are applied for the independence analysis were displayed above. And the results of the independence test were shown respectively in the following subsections.

The Length of the Domain

The bubble terminal velocity can be used to analyze the effect of the domain geometry and the mesh sizes. In the domain applied for the simulation the terminal velocity is already achieved. So the terminal velocities are compared and plotted against the different lengths in Figure 4.10. The number in the X-axis stands for how many times is the length as much as the bubble diameter. The terminal velocity in the domain with the length of 1.5D is obviously deviated from the terminal velocities in the other domains. The deviation of the results from the domain with the length of 2D is considered to be acceptable. Therefore, the 2D length will be used only when the value of the parameter is not important, but the trend of the parameter plays a more important role. In respect of the value of the affecting parameters the 5D length will be applied to the simulation, because it is more precise.

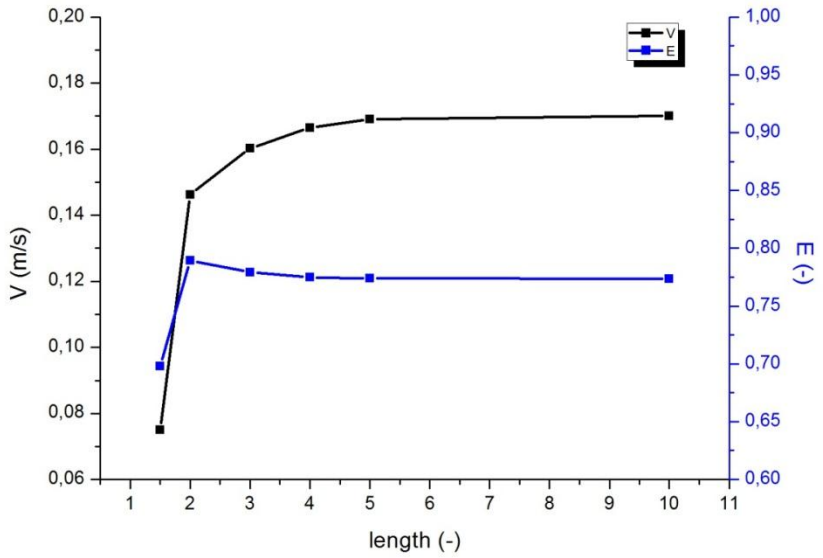

Figure 4.10 Length independence test using terminal velocity and bubble aspect ratios

The bubble aspect ratio E is also used as an indicator to analyze the sensitive of domain geometry and the mesh sizes. Similar to the velocity, the aspect rations E are compared and plotted against the different lengths in Figure 4.10. A huge difference existed between the result from the domain with the length of 1.5D and the results from the domain with the other lengths. So it can be concluded that the derivation of the result obtained with the length of 2D is acceptable and can be used for the following simulations.

The Height of the Domain

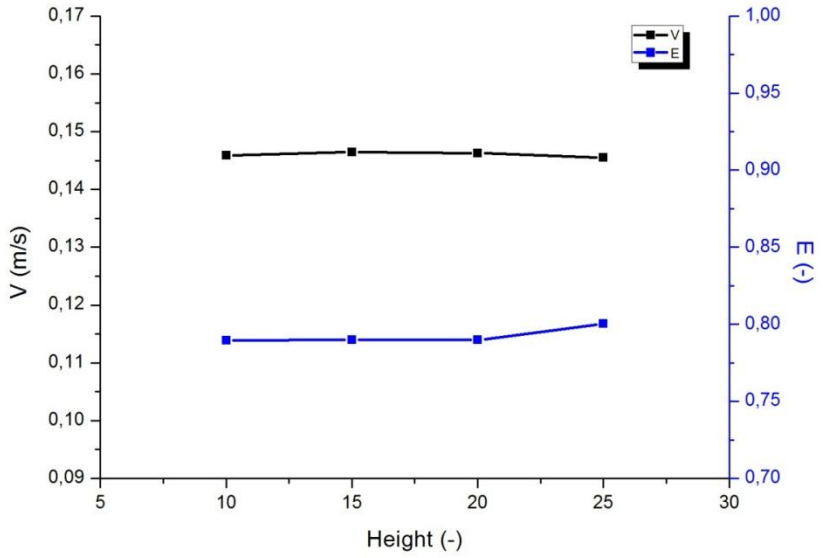

Figure 4.11 Height independence test using terminal velocity and bubble aspect ratios

The bubble terminal velocity and the terminal bubble aspect ratios are also applied to indicate the dependence of the numerical results on the height of the domain. The results are displayed in Figure 4.11. It is seen from the figures that the height of the domain doesn't affect the terminal velocity and the bubble aspect ratios much. In fact, after rising about 3 mm the bubble has already come to a stable state. At all the heights, which are used to analyze the sensitive, the bubbles can get to the stable state. That's why the terminal rising velocities and the terminal bubble aspect ratios at all of the heights are almost the same.

Mesh Element Size

For mesh element size analyses the terminal bubble rising velocity and the aspect rations E are applied as an indicator as well. They are compared and plotted against the different mesh sizes in Figure 4.12. As shown in the figures that the deviation of the results from the mesh size of 0.2 mm and from the size of 0.1 mm is small and acceptable. Both terminal velocities are fast the same and there is little difference in the terminal bubble aspect ratio. However a huge difference existed in the results of the coarsest grid and the other finer grids. It could be concluded that the 0.2 mm can be used as an optimal grid size to do the simulation. That also has a good agreement with the mesh size independence test which is carried out for the 2d model in the last section.

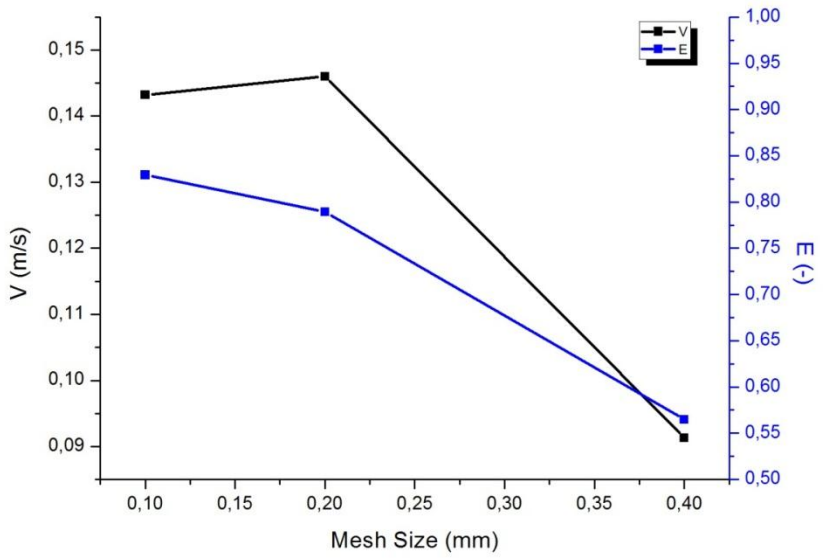

Figure 4.12 Mesh size independence test using bubble rising velocity and bubble aspect ratio

4.6. Escape Zone

4.6.1. Model Geometry and Boundary Conditions

Since 3d models in this section were treated the same as the model in the last section and the independence test was already carried out in the last section, the independence test of the model in this section will be skipped. Two kinds of models were applied to the simulation. A sketch of the two models is shown in Figure 4.13. The first model was applied for small bubbles to assess the effect of the distance between the water surface and the upper edge of the membrane and the second model was developed for bubbles with consideration of the effect of the length of the domain on the numerical results.

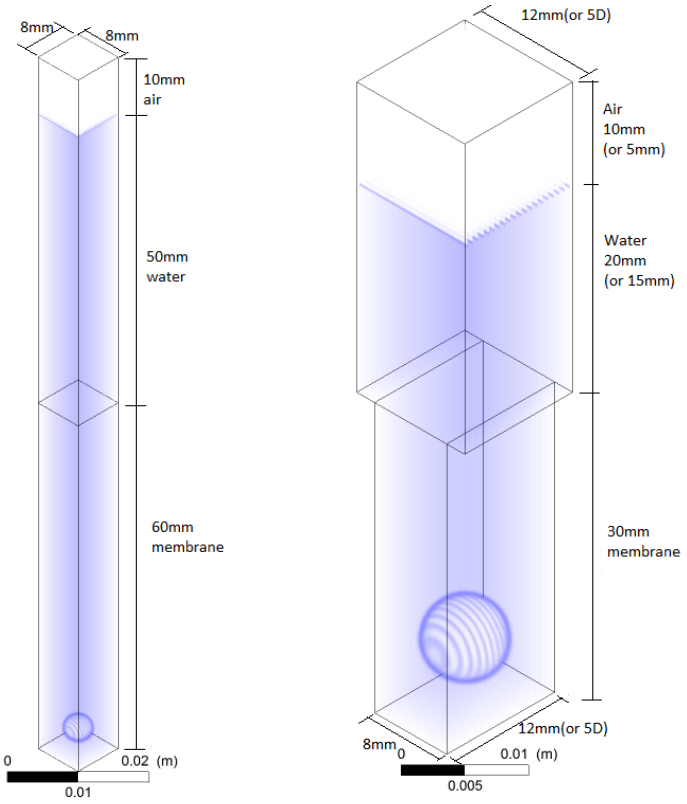

Figure 4.13 Sketch of two models (left: model for the small bubbles; right: model for the large bubbles)

The settings of the boundary conditions in for the simulation in this chapter are similar to the settings for the model in the last section. The membranes and the bottom were set to be wall and the top of the domain was Pressure-outlet. Symmetry was applied to the other planes. It should be noted that the planes above the membranes were set to be symmetry as well.

In this section the effect of the height above the membrane was examined. To investigate this effect the height was set to be 10 mm, 20 mm, 30 mm, 40 mm and 50 mm. The other settings for all the simulations remain the same. Besides various bubble sizes were applied to study the influence of the bubble sizes on the shear force, when the bubble goes out of the gap.

5. Experiment

5.1. Experimental Set-up

The apparatus was supplied by Microdyn NADIR GmbH. The module configuration in Figure 5.1 consists of the MBR modeling apparatus (center), the membrane plates (inside the apparatus), the aeration device (also in the apparatus), the scalar (at the back of the apparatus) and the light sources (left and right). A Casio Exilim EX-ZR100 with a high-speeding recording function was placed in front of the apparatus to record the bubble movement as shown in the left side of Figure 5.1.

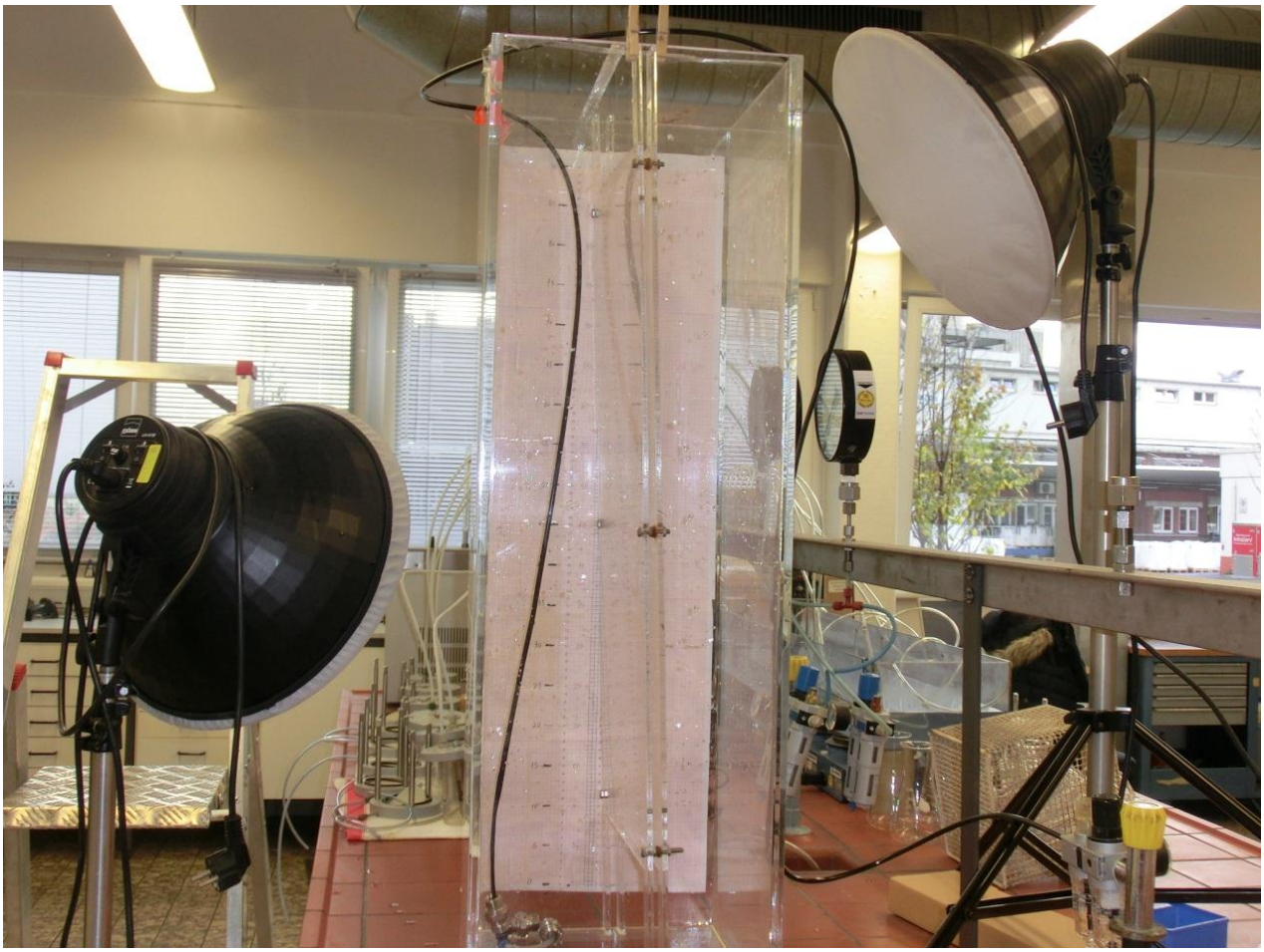

Figure 5.1 Photo of experimental module

The apparatus is 300 mm long, 300 mm wide and 1000 mm high as shown in Figure 5.1. The gap distances of the two membrane plates can be adjusted using hex nuts and stainless steel disk spring. Instead of membrane the plates with transparent materials were used so that the movement of the bubble in the channel can be recorded by the camera. Bubbles were generated from the self-made aeration device, which is made from a hose in the form of a ring. Various holes with different sizes were made in the house of the ring to generate different bubbles and two heavy stainless steel hex nuts were carried through it, so that the device can submerge into the water and be placed at the bottom of the apparatus and in the place where the formed bubble can rise through the gap. A hose connects the aeration device and the pressured gas pipe or a syringe depends on if more than one bubble can be formed at the same time with gas pipe. If it is in this situation the syringe instead of the gas pipe will be used because the syringe can be better controlled. With the scalar at the back of the apparatus the distance is known and with the recording by a high-speed video camera the time is known as well. Based on the time and the distance the velocity of the bubble can be calculated.

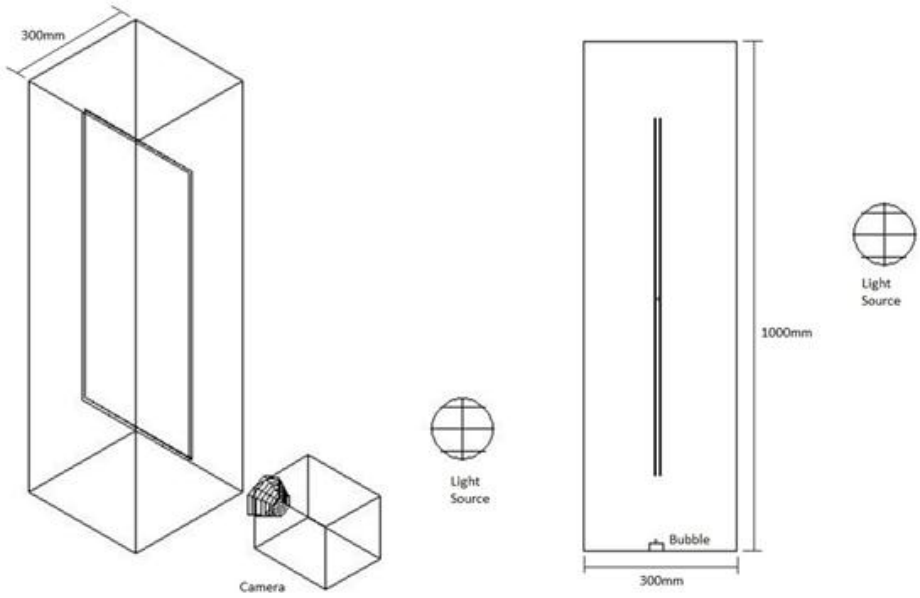

Figure 5.2 Schematic drawings of the experimental module (left: 3d view; right: from the right view)

The nitrogen gas was directed into the stagnant water through different holes, through which the bubbles with a diameter of 1 mm, 2 mm, 3 mm, 4 mm, 5 mm and 6 mm can be generated and then these bubbles were recorded by a high-speeding video camera. To assess the influence of the gap width the distances of the two membrane plates were adjusted as 6 mm, 7 mm, 8 mm, 9 mm and 10 mm respectively. In each case the bubble with the same size was applied. In order to investigate the viscosity of the fluids on the movement of the bubbles xanthan solutions with different concentrations were used for the experiments with 8 mm gap width and the bubble of the same size.

Figure 5.3 Photo of the small experimental module

In order to reduce the computational cost the model in the simulation is very small. It's only 8 mm long, 8 mm wide and about 100 mm high, which is very small compared to the experimental model. So the experimental result and the modeling result may not agree with each other given the different

geometry. So a small experimental model, which was the same as the model in the simulation and displayed in Figure 5.3, was made by a 3D printer. The problem of this model is that the material is ABS plastic and the roughness of the wall is not the same.

5.2. Viscosity Measurement

There are so many methods to measure the fluid viscosity. The viscometer is shown in Figure 5.4. The principle of vertical falling ball viscometer is based on stock's law.

$$\mu = \frac{(\gamma_s - \gamma_f)d^2}{18u_t} \tag{5-1}$$

Where γ is the specific weight; u_t is the terminal velocity and d is the diameter of the sphere ball. The equation can be further simplified to the following formula.

$$\mu = K \cdot (\rho_s - \rho_f) \cdot t; \text{with } K = \frac{g \cdot d^2}{18l} \tag{5-2}$$

Where K is the constant of the falling ball; ρ_s is the density of the falling ball; ρ_f is the density of the fluid to be measured and t is falling time of the sphere with a certain distance l.

Figure 5.4 Vertical falling ball viscometer (left) and analytical balance (right)

In the experiment the volume and the weight of the fluid were measured to calculate the fluid density. The weight was measured by analytic balance shown in Figure 5.4. And the falling time was measured with a mobile phone when the sphere falls from the upper curve to the bottom curve in the vertical falling ball viscometer as shown in Figure 5.4.

5.3. Data Analysis

5.3.1. Viscosity

The weight of the falling ball was measured by the analytical balance and the diameter of the sphere was measured with the calipers. With these data the density can be calculated and the ball constants and measuring range of the ball also can be found out in the literature. The results are displayed in Table 5-1.

Table 5-1 Constants and measuring ranges of every falling ball

Falling Balls	Weight [g]	Diameter [cm]	Density [g/cm^3]	Ball constant	Measuring range [cp]
Ball 1	4.9425	1.58	2.393	0.008	0.2-2.5
Ball 2	4.7865	1.565	2.385	0.06	2 - 20
Ball 3	16.271	1.56	8.185	0.09	15-200

The samples come from the xanthan solution, in which the bubble was rising. The samples have different viscosities. The measuring range of each ball was displayed in Table 5-1. And the Ball 1 was used for the measurement of viscosity in the sample 1 to sample 4. The Ball 2 was used to measure the viscosity of the fluids in the sample 4, the sample 5 and the sample 6. The Ball 3 was applied to the last sample. The viscosity of each fluid was shown in Table 5-2. If the difference of the measured falling time of the ball is small, then the experiment only repeated twice. If not, the experiment will be carried out five times.

Table 5-2 Viscosities of the fluids

Nr	Weight [g]	Density [g/cm^3]	t1 [s]	t2 [s]	t3 [s]	t4 [s]	t5 [s]	averaged t[s]	Viscosity [cp]
1	153.4140	0.9836	86.11	87.51	86.73	85.53	86.80	86.54	0.976
2	153.3190	0.9826	103.04	103.46	103.20	103.20	103.41	103.26	1.166
3	153.2395	0.9818	101.30	101.08	101.20	101.29	101.64	101.30	1.144
4	153.3775	0.9832	116.31	117.23	117.25	116.33	116.21	116.67	1.316
5	153.4836	0.9831	28.83	28.43	28.30	-	-	28.52	2.397
6	153.5514	0.9849	41.53	41.14	41.19	-	-	41.29	3.468
7	153.6753	0.9862	183.08	184.16	182.59	-	-	183.28	15.382
8	153.6391	0.9858	39.87	39.44	40.17	-	-	39.83	25.806

5.3.2. Terminal Velocity

To explore the external factors that affect the experiment, different zoom range of the camera, different horizontal distances that the camera was placed away from the front side of the apparatus and different heights of the camera place were applied for the experiment. The results are shown in the following tables, from which can be seen that these factors named before don't have much influence on the results.

Table 5-3 Terminal velocity of large bubbles and small bubbles with different zoom ranges

	Large Bubbles			Small Bubbles		
Zoom range	63 mm	96 mm	124 mm	63 mm	96 mm	124 mm
N	181	195	256	186	182	182
v [m/s]	0.29	0.29	0.29	0.25	0.25	0.25
Deviation [m/s]	0.02	0.02	0.02	0.02	0.02	0.02

In Table 5-4 the terminal velocity of large bubbles shows some trend. With increasing height, where the camera was placed, decreases the terminal velocity. However, for the small bubbles there is no trend. So maybe it's just an accidental event for the large bubbles.

Table 5-4 Terminal velocity of large bubbles and small bubbles with different heights

	Large Bubbles			Small Bubbles		
Height	21.0cm	49.5cm	69.2cm	21.0cm	49.5cm	69.2cm
N	209	204	283	185	184	181
v [m/s]	0.30	0.29	0.28	0.25	0.25	0.25
Deviation [m/s]	0.02	0.02	0.02	0.02	0.02	0.02

In the table below the terminal velocity shows little dependence on the horizontal distances and the height.

Table 5-5 Terminal velocity of large bubbles and small bubbles with different horizontal distances

	Large Bubbles			Small Bubbles		
Height	10 cm	20 cm	30 cm	10 cm	20 cm	30 cm
N	222	187	187	182	185	183
v [m/s]	0.29	0.29	0.28	0.25	0.25	0.25
Deviation [m/s]	0.02	0.02	0.02	0.02	0.02	0.02
	Viscosity of 0.98 cp			Viscosity of 1.17 cp		
Height	10 cm	20 cm	30 cm	10 cm	20 cm	30 cm
N	68	61	57	63	61	60
v [m/s]	0.21	0.22	0.22	0.24	0.24	0.24
Deviation [m/s]	0.01	0.01	0.01	0.02	0.02	0.01
	Viscosity of 1.14 cp			Viscosity of 1.32 cp		
Height	10 cm	20 cm	30 cm	10 cm	20 cm	30 cm
N	61	57	51	60	60	60
v [m/s]	0.24	0.24	0.24	0.22	0.22	0.22
Deviation [m/s]	0.01	0.01	0.01	0.02	0.00	0.01

6. Results and Discussions

6.1. Validation of the Model

The results from the experiment were compared with the simulation results. However, a good agreement between the two results is not observed. In the experiment the terminal velocity increases with the increasing bubble size. However the velocity increases only slightly. According to the stock's law the larger bubble rises faster, which corresponds to the experimental results. However, the terminal velocity in the stock's law is in direct proportion to the square of the bubble diameter, which means the bubble diameter has a more influence on the terminal velocity than it is in the experiment. The reason for this disagreement is that the larger bubble has a lower shape aspect ratio, which can affect the terminal velocity significantly as well. In the simulation, it has a similar trend. With the increasing bubble size the rising velocity increases. Although the terminal velocity is about proportional to the root of the bubble diameter instead of the square of the bubble diameter, the diameter has a more powerful influence on the terminal velocity in the simulation. Comparing the experimental and numerical results, the velocity in the simulation is much lower than that in the experiment. The main reason for that lies probably in the size of the model. As explained in the chapter 4, the terminal velocity becomes higher when the length of the domain increases. The experimental apparatus was large, but the simulation model was very small. If we use the same domain in the simulation as in the experiment, a more accurate result can be obtained.

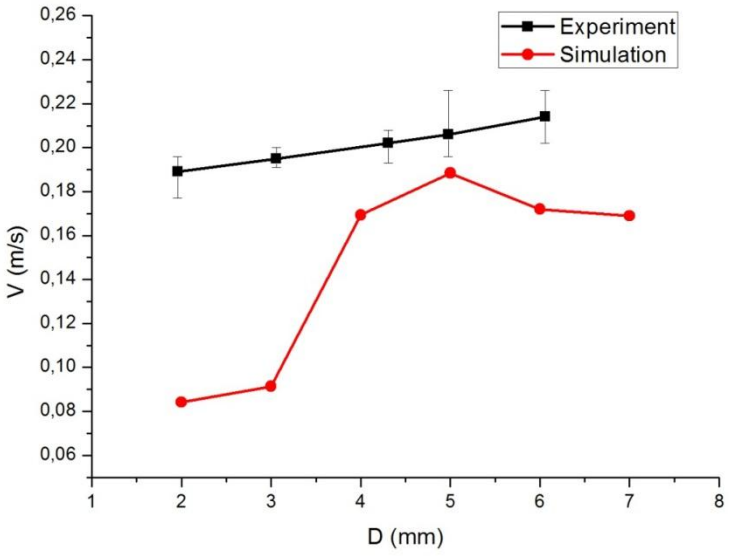

Figure 6.1 Validation results of the experimental terminal velocity of bubbles with different sizes against modeling terminal velocity

In Figure 6.1 it doesn't show any good agreement between the experimental and numerical results. The reason may lie in the experiment. So the results from the CFD simulation will be further checked against the calculated terminal velocity by a model proposed by A.Tomiyama et al. [83]. His model agrees well with the measured terminal velocity in his experiment.

$$V_T = \frac{sin^{-1}\sqrt{1-E^2}-E\sqrt{1-E^2}}{1-E^2}\sqrt{\frac{8\sigma}{\rho_L d_e}E^{4/3}+\frac{\Delta\rho g d_e}{2\rho_L}\frac{E^{2/3}}{1-E^2}} \tag{6-1}$$

Table 6-1 Computational data

Parameters	Value	Unit
bubble equivalent diameter d_e	2-10	mm
Bubble aspect ratio E	0.5-0.95	-
water density ρ_L	998.2	kg/m^3
gas density ρ_g	1.225	kg/m^3
Density difference $\Delta\rho$	996.98	kg/m^3
surface tension σ	0.073	N/m

With this equation (6-1) and the data from Table 6-1, the relationship between the bubble size and the aspect ratio is calculated by Mat Lab and can be shown graphically. The terminal velocity from the direct from the simulation and the velocity obtained based on the graph differs greatly for small bubbles, but for the large bubbles, a good agreement can be achieved.

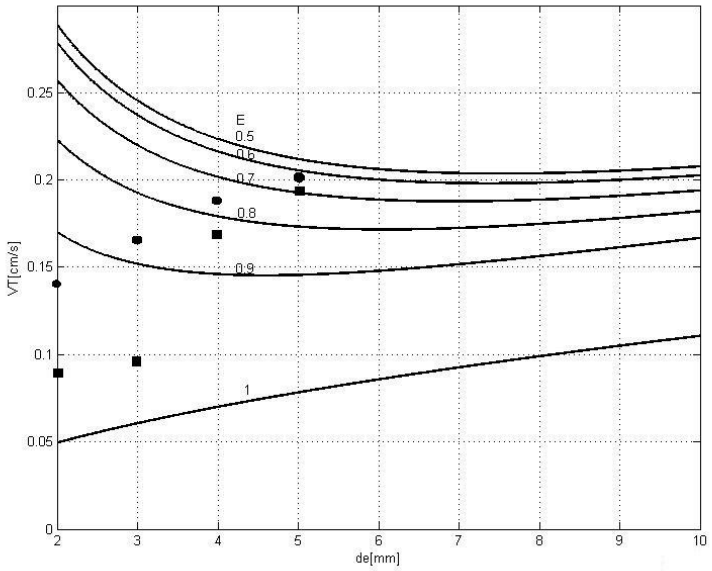

Figure 6.2 The relationship between the terminal velocity, bubble size and the aspect ratio (circle points: location based on the simulated bubble aspect ratio and bubble size; square points: location based on the simulated velocity and the bubble size)

Wellek et al. [84] developed an empirical correlation for the aspect ratio (E) in terms of Eotvos number (Eo), as indicated in the equation below. This model was originally developed for the non-oscillating drops in contaminated liquids, however, L.S. Fan et al. [85] found out that this model can be used for the oscillating bubbles in low-viscosity liquids.

$$E = \frac{1}{1+0.163E_o^{0.757}} \tag{6-2}$$

The calculated bubble aspect ratio and the aspect ratio obtained from the simulation were compared with each other in the following table. Only small bubbles are used for the comparison, because the model above is for free moving bubbles. With an increasing bubble diameter, the wall has a more powerful effect on the motion of the bubble. Therefore, only bubbles with a diameter of 2 mm, 3 mm and 4 mm are used. And from the table the errors in the both results are within 1%, based on which it can be concluded that a good agreement can be achieved.

Table 6-2 Comparison of bubble aspect ratios

Bubble Size	Eo	Calculated aspect ratio	Aspect ratio from simulation	Error(%)
2 mm	0.54	0.907	0.911	0.368
3 mm	1.21	0.842	0.833	0.976
4 mm	2.14	0.775	0.769	0.771

As analyzed in chapter 4 the geometry of the model has a significant effect on the simulating results. In the experiment the bubble movement in a channel and just in the container without the plates was compared in Figure 6.3. Without plates the bubbles can move faster than with plates. For the 6 mm bubble it can be about 30 faster. That also proves that the size of the model affects the results greatly. And without the restraint of the plates the bubble can move freely. Compared to the results from the literature [26], most results are in the valid region.

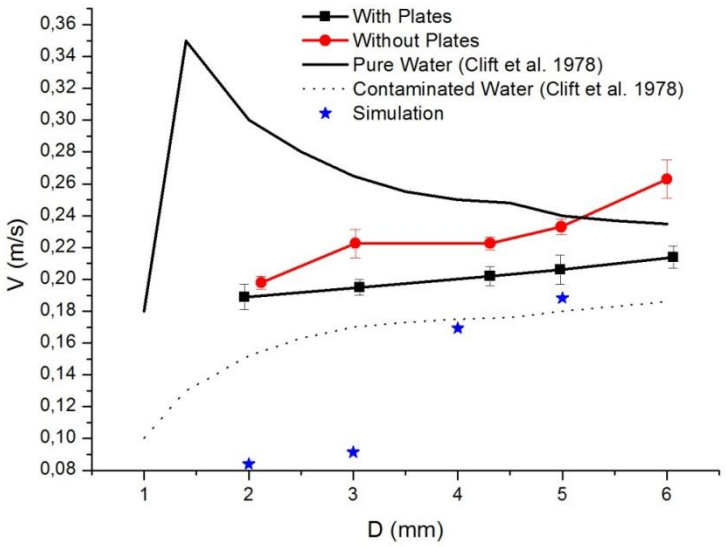

Figure 6.3 Comparison of the terminal velocity with (black) and without (red) plates

Comparing the numerical results with the results from the contaminated water, for large bubbles they agree with each other. So the initial setting of the fluid may be for contaminated water instead for pure water. This also can be proved by the validation of bubble aspect ratio in Table 6-2. The simulated results agree with the calculated aspect ratio from the correlation proposed by Wellek et al. [84], which is suitable for contaminated fluids.

But for small bubbles, huge difference exists between them, as shown in Figure 6.3. The reason for this difference may lie in the more powerful wall effect on the small bubbles. As analyzed in this chapter in the section of the trajectory of bubbles, the small bubbles tend to swing more severely. The existence of the wall may slow down the small bubbles more than the large bubbles. It may also slide along the wall. In this case, the velocity of this bubble is definitely not high.

Table 6-3 Validation results of 4 mm bubble rising in the model without membrane

Simulation [m/s]	Correlation [m/s]	Error [%]
0.226	0.225 [87]	0.58
0.226	0.218 [86]	3.81
0.226	0.240 [26]	5.71
0.226	0.223	1.35

Table 6-4 Validation results of 4 mm bubble rising in the gap of membranes

Simulation [m/s]	Experiment [m/s]	Error [%]
0.169	0.200	15.45

The results of a 4 mm single bubble rising in the stagnant water without membrane were checked against the numerical results from other authors, e.g. Ma et al. [86] and M. T. Islam et al. [87] and the experimental results from my experiment and from the experience [26]. The numerical result of a 4 mm bubble rising in the gap of membranes was compared with the result obtained from my experiment with large apparatus. At last the numerical result and experimental result obtained with the small apparatus were compared with each other. These comparisons were shown in the following tables respectively. The result from the simulation was checked against the other results. In Table 6-3 and Table 6-4 a very good agreement was shown.

Table 6-5 Validation results of 4 mm bubble rising in a small model

Simulation [m/s]	Experiment [m/s]	Error [%]
0.146	0.145	0.41

In Table 6-5 the modeling terminal velocity is 0.146 m/s. It's worth mentioning that if the equation of Davidson and Harrison model [27] was applied to predict the terminal velocity, a very good agreement can be achieved as well. The calculated result was 0.141 m/s, which only has an error of 2.42% in comparison of the numerical result. However, the Davidson and Harrison model was for spherical-cap bubble, which usually has a diameter greater than 15 mm. With the influence of the wall effect and the geometry of the small model a 4 mm bubble probably already belongs to the spherical-cap bubble in this situation.

From Table 6-3, Table 6-3 and Table 6-5 it can be seen that all of the results except the results of 4 mm bubble rising in the gap of membranes agree with the experimental results and the numerical results in the literature perfectly, which means the CFD simulation is capable of predicting an accurate result. The huge difference of the results for a bubble rising in the gap of membrane plates may lie in the inaccurate experimental result. In the experiment serial bubbles instead of a single bubble were pumped into the water. When bubbles rise upward, the flow under the bubble is already affected by this bubble. And the bubble size also depends on the gas flow, which is not stable in the experiment. What's more, the bubble was generated from the hole of the hose, whose size is related to the pump pressure. At higher pressure it has a large hole, which can create a larger bubble. The results of small bubbles are not that much reliable, because of the relative coarse mesh size. Despite the difference, the trends in the simulation and in the experiment are similar. Besides, the numerical results are in agreement with the results from the previous literature and the experimental result of contaminated water by other authors. In a whole, the CFD simulation is capable of predicting an accurate result.

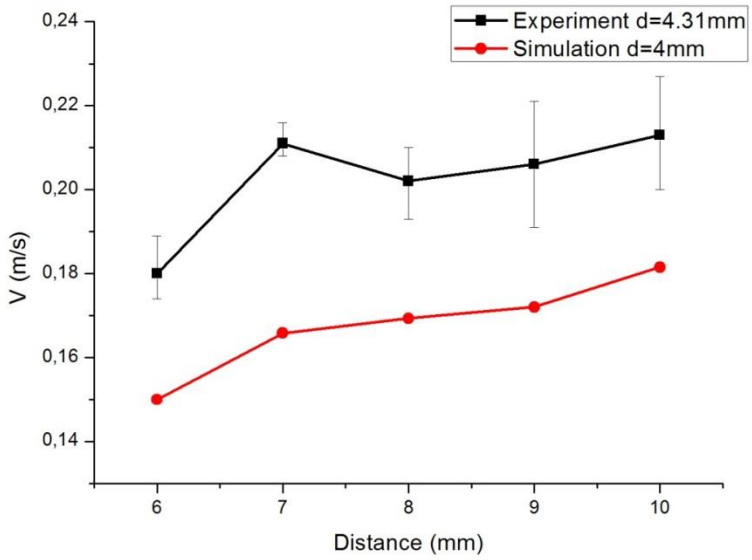

Figure 6.4 Validation results of the experimental bubble terminal velocity in models with different gap widths against modeling terminal velocity

The trends of the both results are similar to Figure 6.4. Both in the experiment and in the simulation, the lowest terminal velocity occurs at the narrowest gap, and the maximal terminal velocity is at the widest gap distance. However, the value of velocity at each gap width doesn't match. The velocity values obtained the simulation is lower than that in the experiment. Considering that the length of the model affects the results significantly as shown in Figure 4.10 in the chapter 5, the phenomenon described above is reasonable. Another explanation of the lower velocity in the simulation lies in the fact that the fluid in the simulation might not be pure water as expected, but contaminated water, in which bubble rises slowly, as shown in Figure 6.3.

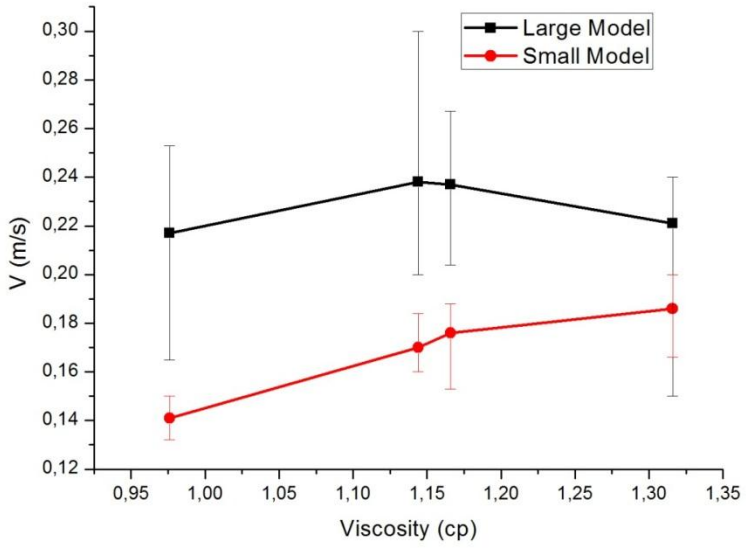

Figure 6.5 Comparison of the results from the large model (black) and small model (red) in the experiment

Since the results from the experiment and the simulation cannot agree with each other, a small model was built, which has the same domain as modeling domain, to overcome the disadvantage caused by the geometry. The experimental terminal velocity of the large model and the small model is compared in Figure 6.5. Still huge difference exists between both results. Firstly the size and the material of the apparatus may cause this difference. Secondly the xanthan solution in the large model may not be uniform. The upper layer may have a higher concentration than the bottom layer. So the viscosity in the zone, where the video was filmed, was probably not the same as the viscosity in the sample, which was taken from the relative upper zone. But in the small model the solution was mixed very well. Last not least, the samples were stored for about two weeks before measuring the viscosity. After two weeks the viscosity of the xanthan solution may be changed. However, the experiment in the smaller model was carried out in the same day, when the viscosities of the fluids were measured. So the results obtained from the small model are more representative than that of the large model. Therefore the results from the small model were applied to the following validation of the experimental and numerical results in Figure 6.6.

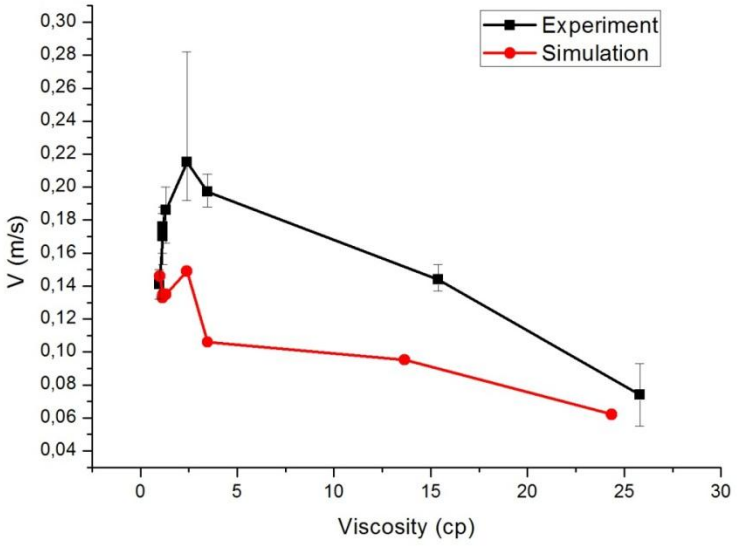

Figure 6.6 Validation results of the experimental terminal velocity of bubbles at different viscosities against modeling terminal velocity

In Figure 6.6 the terminal velocity against the viscosity shows the same trend. At low viscosity about 1 cp and high viscosity about 25 cp a very good agreement between the experimental and the numerical results can be observed. At other viscosities the agreement is not good. The reason lies probably in the bubble size. In the simulation the bubble is set to have a diameter of 4 mm. However, in the experiment the bubble diameter cannot be accurately guaranteed to be 4 mm. Sometimes the syringe needle produces larger bubbles, sometimes smaller bubbles. Bubble size can affect the terminal velocity as well. Generally speaking the experimental results from the small model and the numerical results agree with each other well.

The results obtained from the simulation and the experiment only agrees with each other at low viscosity of the fluids. Following reasons may cause this problem. Firstly, the surface tension of water and air was set to be 0.073 N/m in the simulation. But this value changes with temperature and viscosity. Thus, at high viscosity, the difference between the real value of surface tension and the value in the simulation could be huge. And surface tension affects the shape of the bubble greatly and which in turn affects the terminal velocity significantly. Secondly, in the simulation the small apparatus is

made of ABS plastic. The roughness of the wall and the wall effect may have a very powerful effect on the bubble motion. At last, in the simulation only a bubble rises in the model, whereas in the experiment a series of bubbles is in the small apparatus at the same time. And the existences of the other bubbles definitely have an effect on the motion of the bubble.

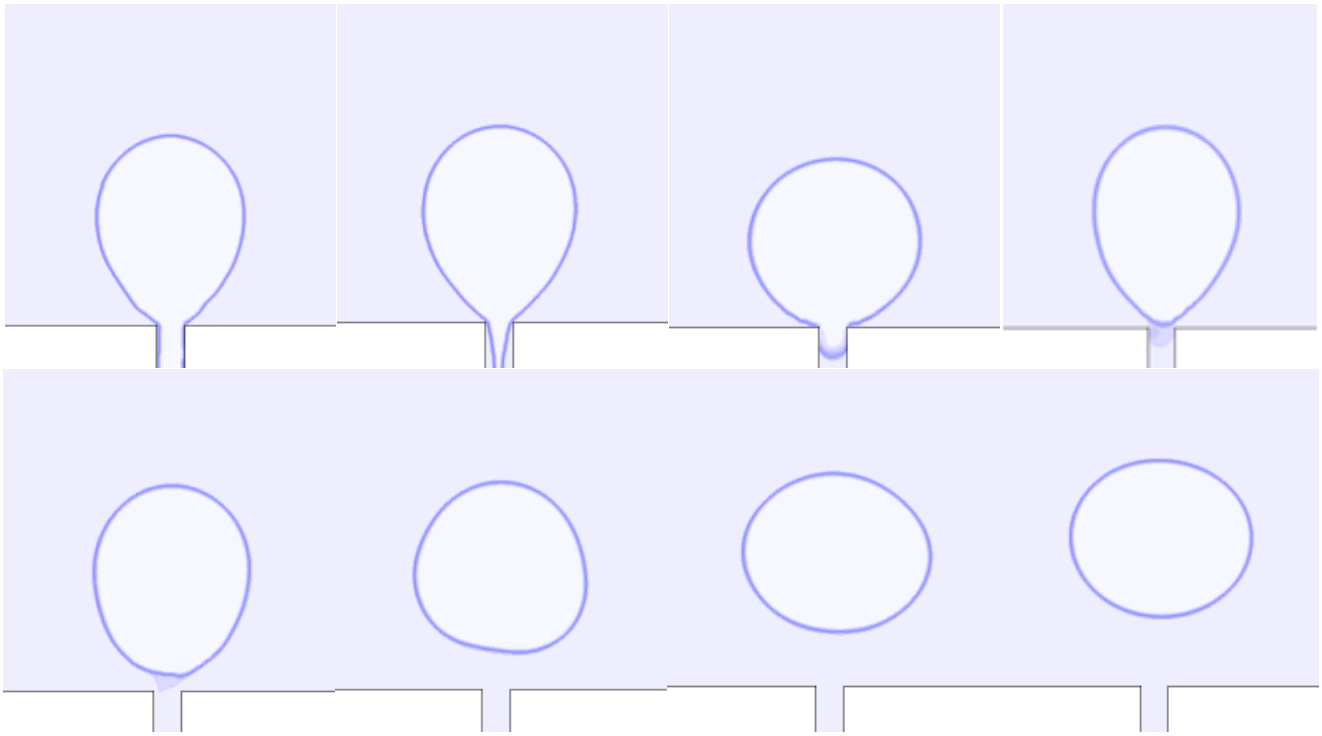

Figure 6.7 Bubble formation pictures

For the bubble formation in 2d simulation, the results were checked against the experimental results found from literature [88]. A good agreement between the two results can be achieved.

To be concluded, a good agreement between the experimental results from the small model and from the simulation can be gained, which means the settings of the simulation is correct. The results for the experiment were found in the valid region in literature [26]. And similar results for the modeling also can be found in literature [89]. However, the two results don't match because the size of the model in the simulation and the size of the model in the experiment have a huge difference. If the model in the simulation had the same domain as in the experiment, a very good agreement could be gained.

6.2. The Affecting Factor of Bubble Formation

In this section, the effect of operating pressures, the effect of inlet geometry, the effect of the inlet velocity and the effect of the way the gas was injected into the system ware exanimated respectively as below.

6.2.1. Pressure

The simulations were performed with different operating pressures, which were 101325 Pa, 11325 Pa and 12325 Pa respectively. 11325 Pa was chosen, because the atmospheric pressure plus the pressure produced by 1 m water is equal to about 11325 Pa. Out of the same reason 12325 Pa was chosen as well.

It could be seen from the figures above that pressure doesn't have much influence on the bubble shape and bubble rising velocity. Reason of which is that the pressure difference is not large enough to affect the bubble shape and rising velocity. It can also be concluded that in practice the static pressure produced by the liquid phase is not so important for the formation of the bubbles.

Another reason may be that the pressure was applied to the gas phase. It is like a very high gas column was added at the top of the water surface. In fact the gas column is infinitely high in reality. Besides, the gauge pressure at the water surface is 0 Pa. Therefore, no matter how high the gas column is, the gauge pressure at the water surface remains the same. That's why the operating pressure doesn't have any influence on the bubble formation. The curve at each operating pressure should be identical. However, in Figure 6.8 and Figure 6.9 the curves are not identical. The reason is because of the different first time step.

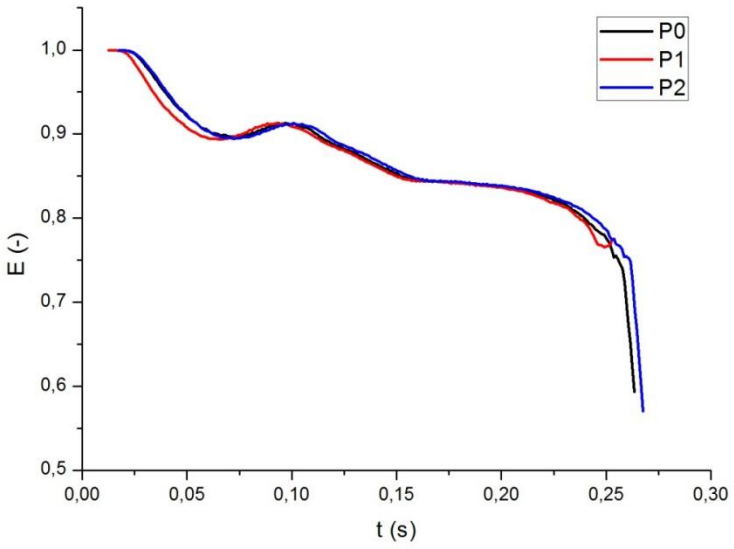

Figure 6.8 Comparison of bubble aspect ratios in different operating pressures

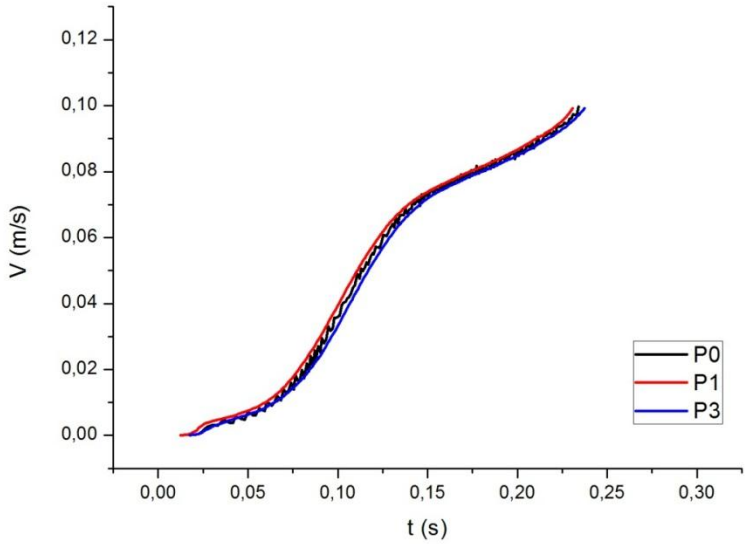

Figure 6.9 Comparison of bubble rising velocity in different operating pressures

6.2.2. 2D Inlet Dimension

As the same amount air was injected into the domain, the generated bubbles for both situations are almost of the same size. The equivalent diameter of both bubbles is about 3.56 mm. However, the bubble formed by the smaller inlet is slightly bigger than the other one. Because of the small inlet, only a little amount of gas remains in the inlet at the bottom of the domain. And for the bigger inlet, there is more gas in the inlet. In respect of the bubble size, it is considered that the geometry of the inlet doesn't have much influence on it. Instead of it, the amount of air, which is injected into the domain to form the bubble, is essential.

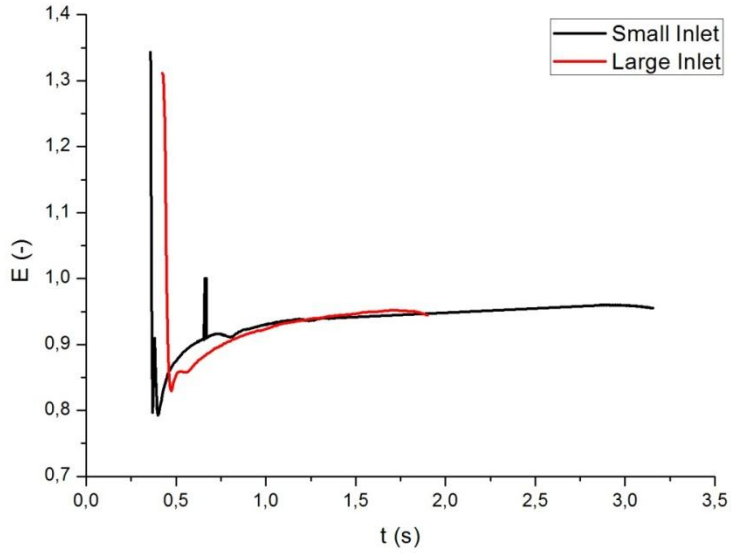

Figure 6.10 Comparison of bubble aspect ratios for big inlet and small inlet

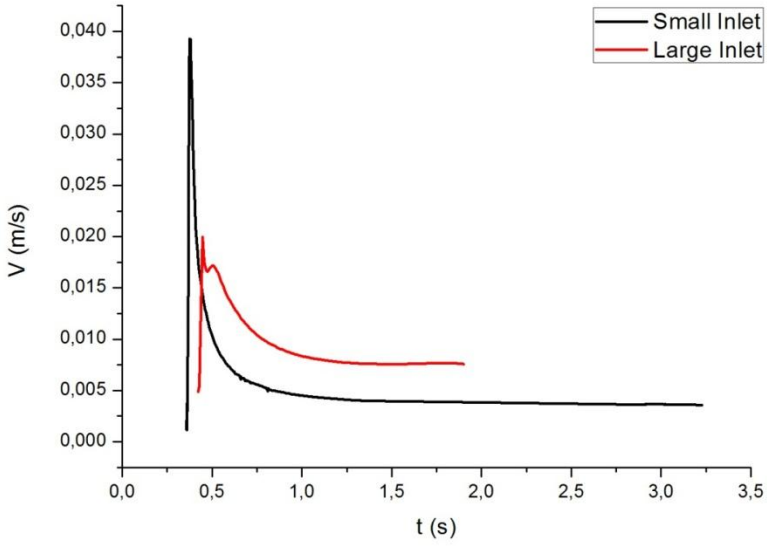

Figure 6.11 Comparison of bubble rising velocity for big inlet and small inlet

As for the shape, it could be seen from Figure 6.10 that the bubble aspect ratios for both situations showed the same pattern. At first the vertical diameter becomes larger and larger. And when the bubble leaves the wall, the vertical diameter comes to the maximum. Then it decreases dramatically to

its minimum in 0.05 s. At last it comes to its stable state slowly. The terminal aspect ratios for the bubbles are still the same.

It seems that the geometrical figure of the inlet is completely irrelevant. However, it may affect the bubble formation. During the simulation with the bigger inlet, the bubble was broken several times. But the bubble generated by the smaller inlet was never broken during its simulation. So the probability of bubble break-up may increase with the increasing inlet.

In order to form bubbles of the same size, the same amount of gas was injected into the domain. The aeration time was the same. Only the velocity inlet was different. The smaller inlet had a larger velocity of 15 m/s, while the inlet velocity for the big inlet is 5 m/s. Normally, it is supposed that the velocity of the bubble generated through the smaller inlet will be larger, because it has a larger initial velocity. However, it is interesting that bubbles with larger initial velocity also encounters more resistance .The velocity of these bubbles drops quickly and the stabilized velocity is lower than that of the bubbles formed by the larger inlet. This phenomenon can be seen from Figure 6.11. From the figure it can also be seen that the velocity of big inlet is always larger than that of a small inlet. The reason of which is that the computational domain is not large enough for the bubble to get to its terminal velocity. Thus the bubble rising velocity for both situations still showed a decreasing tendency.

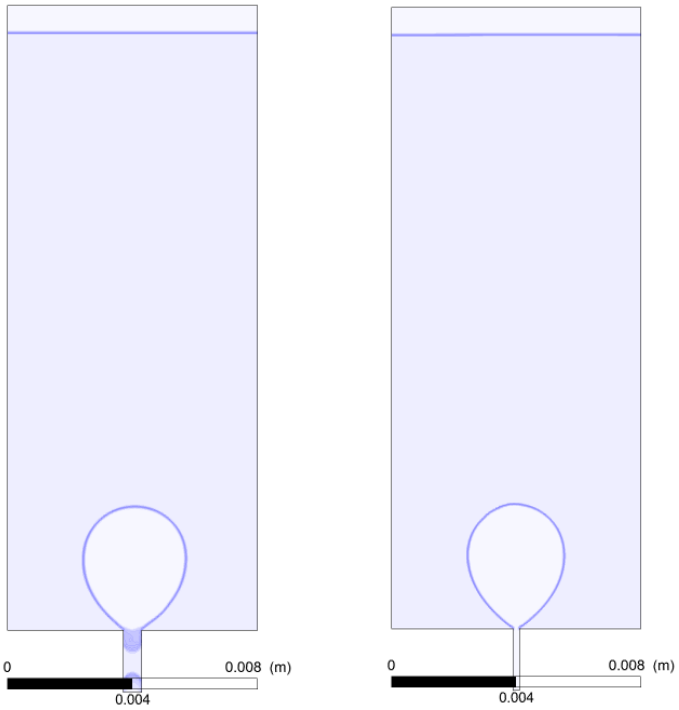

Figure 6.12 Snapshot of bubble obtained from larger inlet (left) and smaller inlet (right) in 2d model

If the aeration is discontinued, the amount of the gas injected into the liquid instead of the hole size is essential to the bubble size and bubble shape. The inlet velocity doesn't have an effect on the bubble formation either. However, it is suggested that a smaller velocity is applied to the system so that it on one hand can save the energy cost, and on the other hand the bubble can obtain a higher velocity.

6.2.3. 3D Inlet Dimension

In order to investigate the effect of the inlet dimensions the form and sizes of bubbles, which are generated by two kinds of inlets, are compared in the following pictures. It is well known that bubbles

generated through smaller inlet hole are smaller, which can be seen in Figure 6.13. The volume of a single bubble generated through the smaller is about 71 mm^3. And the volume of a bigger bubble is 393 mm^3. The area of the larger inlet is 7 times larger than that of the smaller one, which means the gas flow rate at the larger inlet is 8 times of that at the smaller inlet. However the large bubble volume is only about 5.5 times the size of the smaller bubble volume.

It is also can be seen from the following figure that the distances between two bubbles are different in the two situations. The distance between two smaller bubbles is longer than that of two larger bubbles. Because of the larger gas flow rate at the larger inlet the bubble can be quickly formed.

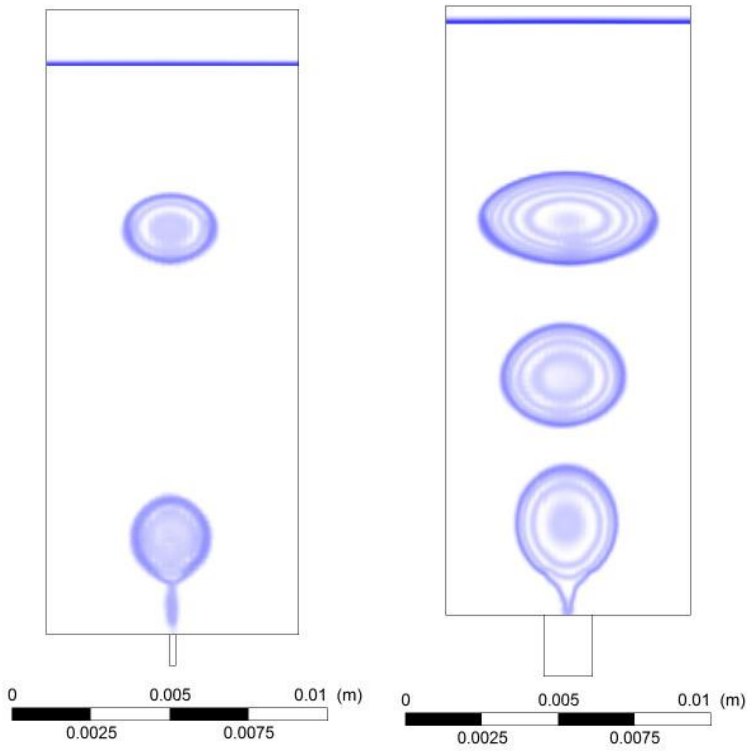

Figure 6.13 Snapshot of bubble obtained from the smaller inlet (left) and the larger inlet (right) in 3d model at the velocity of 3 m/s.

As for the shape of the bubbles, a detailed comparison is listed in Table 6-6. Compared to the smaller bubble the large one has more deformation. The maximal vertical dimensions of the two kinds of bubbles are not quite different. However, there exist large differences in maximal horizontal dimension. The horizontal dimension of the large bubble is about twice as much as that of the small one.

Table 6-6 Comparison of the shape of bubbles formed through two kinds of inlets

Inlet Dimension	Small Inlet	Large Inlet
Bubble volume [mm^3]	71	393
Max. horizontal dimension [m]	0.0028	0.0057
Max. vertical dimension [m]	0.0020	0.0029
Bubble aspect ratio	0.721	0.508

So it can also be concluded that the dimension of the inlet has a great influence on the bubble sizes and shapes. A similar conclusion can be drawn from the simulation with single bubble. Generally speaking, a bigger bubble can be produced through a larger inlet, when the inlet velocities for both conditions stay the same.

Table 6-7 Comparison of the bubble size at two kinds of inlets

Inlet Dimension	Small Inlet	Large Inlet
The first Bubble volume [mm^3]	66.03	102.64

Compared to the Table 6-6 and the Table 6-7, it is found out that at the same injection velocity the bubble size is about the same no matter the air is continuously given or just injected into the model in a short period through the smaller inlet. However, for the large inlet, it is not the case. It seems that huge difference exists in the bubble volume. The reason of smaller bubble in the model with shorter aeration doesn't lie in the shortage of air amount, since more than one bubble is formed in this model. So the way which gas is injected into the system also has an effect on the bubble formation and the bubble size.

6.2.4. Inlet Velocity

1 m/s, 2 m/s and 3 m/s were set in the inlet for the model with larger dimension to investigate the effect of the gas flow rate on the bubble sizes. The snapshot of obtained bubbles is displayed in Figure 6.14.

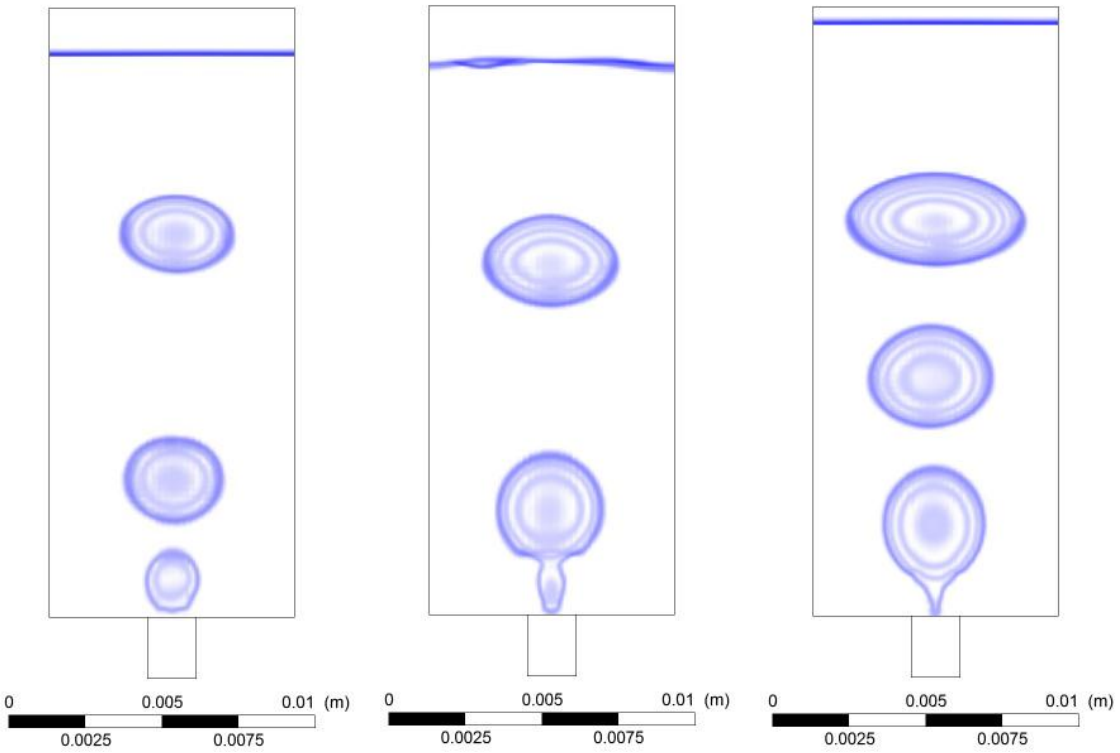

Figure 6.14 Snapshot of bubbles obtained at different inlet velocity (from left to right: the velocity is 1 m/s, 2 m/s and 3 m/s respectively)

It is known from the pictures that the bubble size increases with the increasing velocity and the shape of the bubble is severely more deformed with increasing bubble size. To achieve a better comparison of the bubbles generated at different velocities the equivalent diameter is used to measure the bubble size.

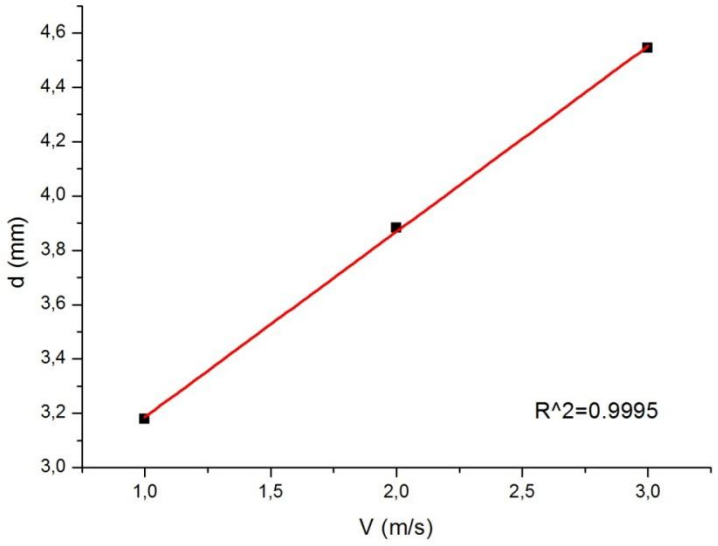

Figure 6.15 Comparison of the bubble sizes obtained at different velocities

The equivalent diameter of a single bubble is plotted against the velocity at the inlet in Figure 6.15. It is shown in the figure that the bubble equivalent diameter and the velocity at the inlet have a linear relationship. The linear correlation is nearly 1. However, the relationship between the equivalent diameter and velocity is not correct. When the velocity equals to 0 m/s at the inlet, then based on the functional relation the equivalent diameter should be 2.5 mm. However, this is contrary to the fact that bubbles could not be formed when the gas flow rate is equal to 0 m^3/s. So this expression may be valid only when the velocity is larger than 0 m/s.

A detailed comparison of the shape of bubbles obtained at different inlet velocities is displayed in Table 6-8. There is more deformation with increasing bubble sizes. The differences in maximal vertical dimensions of different sizes of bubbles are small. However, the differences in maximal horizontal dimension are huge. This phenomenon can also be observed from Figure 6.15.

Table 6-8 Comparison of the shape of bubbles obtained at different velocities

Inlet Velocity [m/s]	1	2	3
Bubble volume [mm^3]	135	245	393
Equivalent diameter [mm]	3.18	3.88	4.55
Max. horizontal dimension [m]	0.0037	0.0047	0.0057
Max. vertical dimension [m]	0.0024	0.0027	0.0029
Bubble aspect ratio	0.665	0.570	0.508

For the simulation with single bubble the conclusion is also similar. When the aeration time is the same, the larger the velocity is, the bigger the bubble will be formed. The amount of the injected gas into the system and the initial gas amount in the inlet together determine the bubble size, as shown in Table 6-9. The bubble volume at 1.00 m/s is not twice as large as the volume at 0.50 m/s, because the bubble takes more air from the inlet at lower velocity.

Table 6-9 Comparison of the single bubble size at different velocities

Case	1	2	3
Inlet Velocity [m/s]	0.50	1.00	3.00
Aeration Time [s]	0.01	0.01	0.04
Bubble volume [mm^3]	18.47	28.37	102.64
Air volume in inlet before [mm^3]	4.86	4.86	4.86
Air volume in inlet after [mm^3]	0.14	2.74	2.53
Bubble Volume from aeration [mm^3]	13.75	26.24	100.31

However, the aeration time also plays a critical role in bubble formation. When the aeration time lasts too long, several bubbles instead of a large bubble will be formed. Compare case 3 and case 1, the amount of injected gas in case 3 should be 12 times as much as that in case 1. However, the gas from the aeration, which is used to form the first bubble, is much less than the total injected gas. This is because after the generation of the first bubble, another bubble is formed. There is more than one bubble in the system for case 3.

So it can also be concluded that the inlet velocity or the gas flow rate has a direct relationship with the bubble size, which affects the bubble shapes. Aeration time can also play an important part in bubble formation.

6.3. The Affecting Factor of Terminal Velocity

Pressure, bubble size, the gap distances of membranes, the viscosity and temperature and the velocity of the fluid around the bubble were estimated to check out their effect on the bubble behavior in respect of bubble terminal rising velocity and bubble shape aspect ratio.

6.3.1. Bubble Size

The snapshots of bubbles with a diameter from 2 mm to 10 mm were displayed in Figure 6.16. It can be seen that the bubbles were deformed more severely with the increasing diameter. In the chapter 2 we have discussed that based on the shape of the bubbles three kinds of bubbles can be divided: spherical bubbles, ellipsoidal bubbles and spherical-cap bubbles. In the simulation bubbles with the diameter of 2 mm and 3 mm belong to the spherical bubbles. 4 mm-7 mm Bubbles can be regarded as ellipsoidal bubbles and 8-10 mm bubbles are spherical-cap bubbles. In the literature, only very large bubbles with diameter greater than 15 mm belong have the spherical-cap shape. However, in this simulation 8 mm bubbles have already shown this character. The reason for this contradiction is that the bubble movement is constrained by the membrane in the simulation. When the bubble diameter is smaller than the gap width, the deformation occurs mainly in the horizontal dimension of the bubble. From the shape of the bubble, these bubbles belong to the free bubble. However, when the bubble diameter is equal and greater than the gap width, the deformation occurs mainly in the vertical dimension of the bubble. These bubbles are in the slug bubble regime.

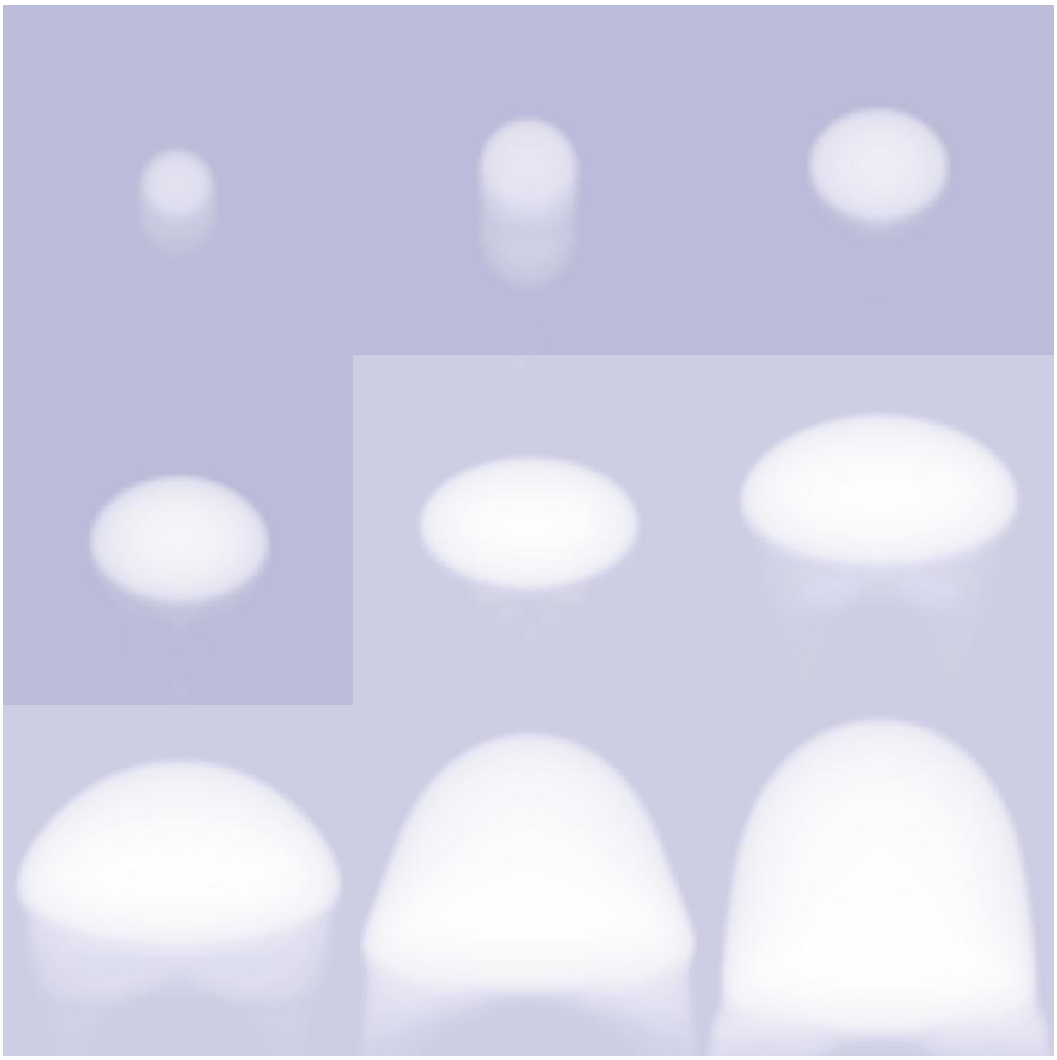

Figure 6.16 Snapshot of bubbles with different sizes (from 2 mm to 10 mm)

As analyzed in the chapter 3, several dimensionless numbers and Grace Diagram can be applied for the estimation of the bubble shape regime. In this simulation, the simulation data were displayed in Table 6-10. These data were used to calculate the dimensionless variables e.g. Eotvos number (*Eo*) and Morton number (*M*) using the following equations:

$$Eo = \frac{F_b}{F_s} = \frac{\Delta\rho g d^2}{\sigma} \tag{6-3}$$

$$M = \frac{F_\mu^4 F_b}{F_s^3 F_i^2} = \frac{\Delta\rho g \mu_L^4}{\rho_L^2 \sigma^3} \tag{6-4}$$

Table 6-10 Computational data

Parameters	Value	Unit
bubble equivalent diameter d_e	2-10	mm
water viscosity μ_L	0.001003	kg/m-s
water density ρ_L	998.2	kg/m^3
gas density ρ_g	1.225	kg/m^3
Density difference $\Delta\rho$	996.98	kg/m^3
surface tension σ	0.073	N/m

The results of these numbers were calculated and displayed in Table 6-11. With these data the bubble can be located in the bubble shape regime diagram of Grace, as shown in Figure 6.17, the bubble shape regime can be read from the graph.

Table 6-11 Eotvos number (Eo), Morton number (M) and bubble shape regime for bubble with different sizes

Bubble Size	*Eo*	*M*	Bubble Regime
2 mm	0.54	2.55×10^{-11}	Wobbling bubble
3 mm	1.21	2.55×10^{-11}	Wobbling bubble
4 mm	2.14	2.55×10^{-11}	Wobbling bubble
5 mm	3.35	2.55×10^{-11}	Wobbling bubble
6 mm	4.82	2.55×10^{-11}	Wobbling bubble
7 mm	6.56	2.55×10^{-11}	Wobbling bubble
8 mm	8.57	2.55×10^{-11}	Wobbling bubble
9 mm	10.85	2.55×10^{-11}	Wobbling bubble
10 mm	13.40	2.55×10^{-11}	Spherical-cup bubble

From Figure 6.17 we can see that all of the bubbles except for the 10 mm bubble are in the wobbling regime, which doesn't match the conclusion based on the shape that smaller bubbles are ellipsoidal and larger bubbles are in the spherical-cup regime. The reason for the difference may be in the existence of the membrane, which may have a wall effect on the bubble motion. Comparing the Reynolds number from the simulation and the number from the Grace bubble diagram, the modeling Reynolds numbers are always less than that from the Grace diagram. It is also because of the fact that the membrane affects the bubble rising significantly. The Grace diagram is for the rise of bubbles without consideration of wall effect. However, in the simulation, bubbles are rising between the gap of membranes, which have a strong wall effect on the dynamics of bubble motion.

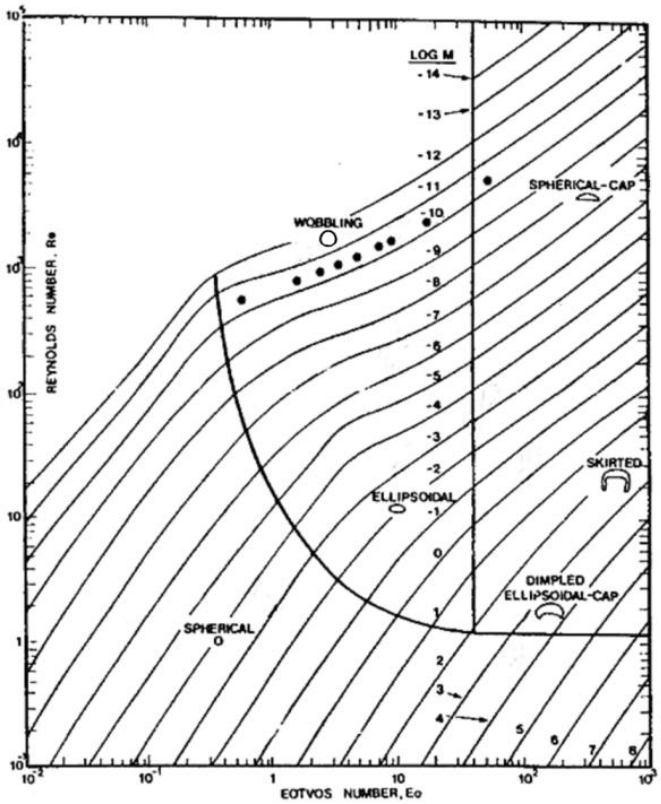

Figure 6.17 Bubble shape regime map of Grace [28] (adapted from Annaland M. V. et al. [29])

The effect of the bubble size was investigated by patching a single bubble with the diameter of 2 mm, 3 mm, 4 mm and 5 mm respectively into the stagnant water. The terminal shape aspect ratio and the bubble rising velocity were compared and shown in Figure 6.18.

From the following figure we can know that the smaller the bubble is, the higher the aspect ratio will be. The surface tension pulls the gas together and keeps the bubble's shape spherical. However, when the bubble is big enough and rises fast enough, the force of the water pushing on the top of the bubble becomes large enough to make the bubble flat. The larger the force, the flatter the bubble becomes. Thus the smaller bubble tends to have a more near-spherical shape and the larger bubbles are normally flat and have a cap shape.

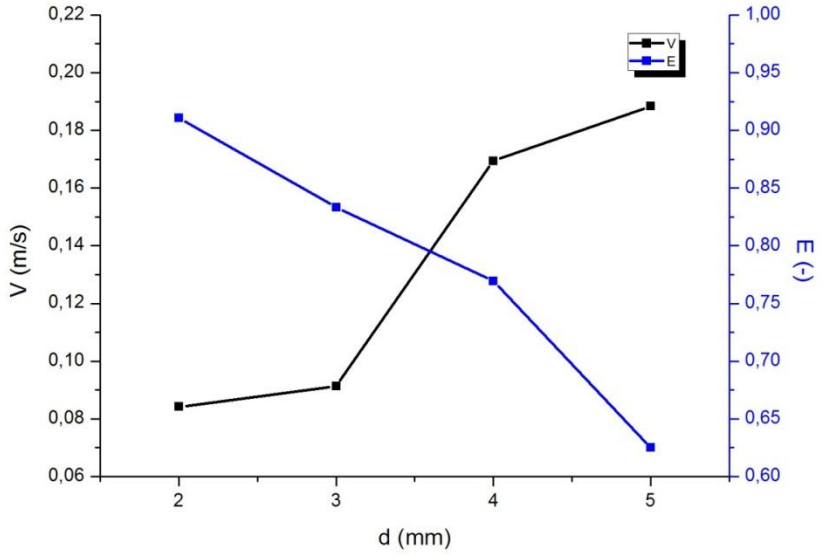

Figure 6.18 The effect of bubble size on the terminal velocity and the aspect ratio

The effect of the bubble size on the terminal velocity was indicated in Figure 6.18 by patching bubble with diameters from 2 mm to 5 mm in the stagnant water. To study this effect the Stokes's law is always applied to the terminal velocity, which is directly proportional to the squared diameter of the bubble. In other words, the bigger the bubble is, the larger the velocity will be. The result in the Figure 6.18 is the case; however, the relationship between the velocity and the bubble diameter is not the same. The terminal velocity is about proportional to the root of the bubble diameter. This is because the bubble shape also plays a critical role in the terminal velocity. As we all know that one of the assumptions of the Stoke's law is spherical shape of the bubble. And we have analyzed above and it is also indicated in the figure above that only small bubbles have a near-spherical shape. Large bubbles are believed to suffer more resistance as they rise. As a result, the relationship between the bubble rising velocity and the bubble diameter doesn't follow the Stoke's law. Another reason lies probably in that the stock's law was applied for the free bubble rise without any membrane plates. The movement of the bubble in the membrane plates must be affected by the membranes.

It is not just the shape was affected by the gap distance, but also the terminal velocity. It shows clearly that the bubble velocity increases with the increasing bubble size and it reaches its maximum at the bubble diameter of 5 mm. Then it decreases slowly and at a certain bubble size, the bubble rises with a constant terminal velocity. The terminal velocity in the graph above shows this trend because of the gap distance. When the bubble diameter is greater than the gap distance, the velocity stays almost the

same. For large bubbles with a diameter greater than 5 mm but less than the gap distance, the bubble was slowed down because of the existence of the membrane.

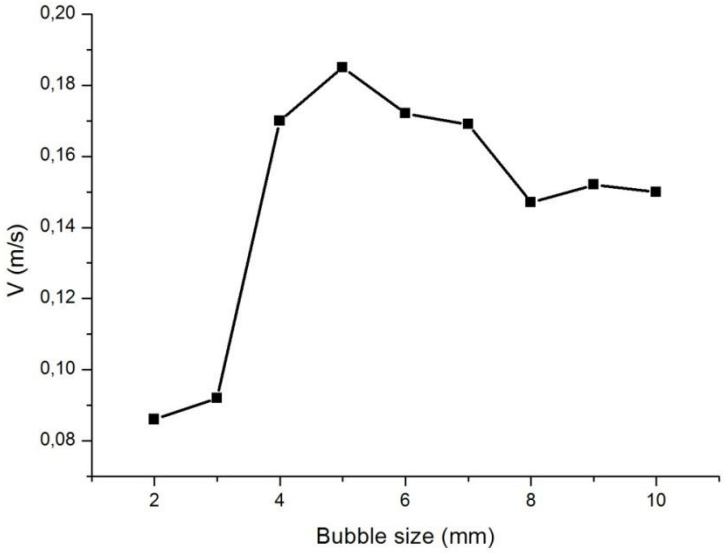

Figure 6.19 The effect of bubble size on the terminal velocity

As shown in the Figure 6.20 and in Figure 6.21, with increasing bubble size the terminal velocity becomes greater, however, the aspect ratio keeps decreasing. This phenomena and the relationship between the bubble diameter, aspect ratio and terminal velocity was displayed in the following graph, which is created with Matlab using the correlation proposed by A.Tomiyama [90]. This graph further proves that the terminal velocity depends not only on the bubble size, but also on the aspect ratio.

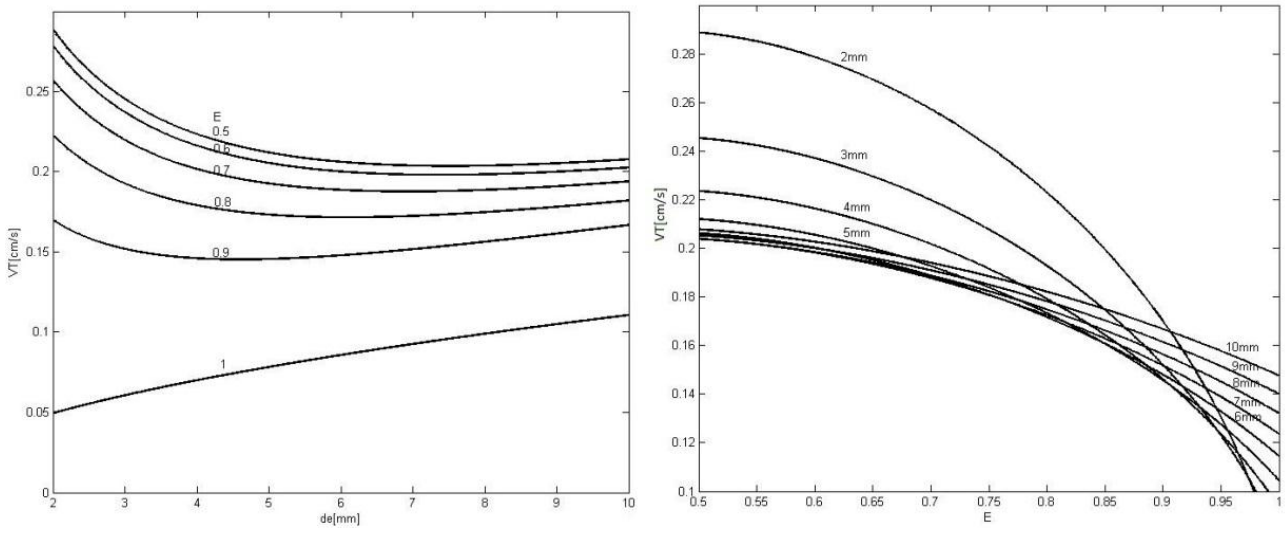

Figure 6.20 The effect of bubble size (left) and aspect ratio (right) on the terminal rising velocity for the rise of single bubble in stagnant water

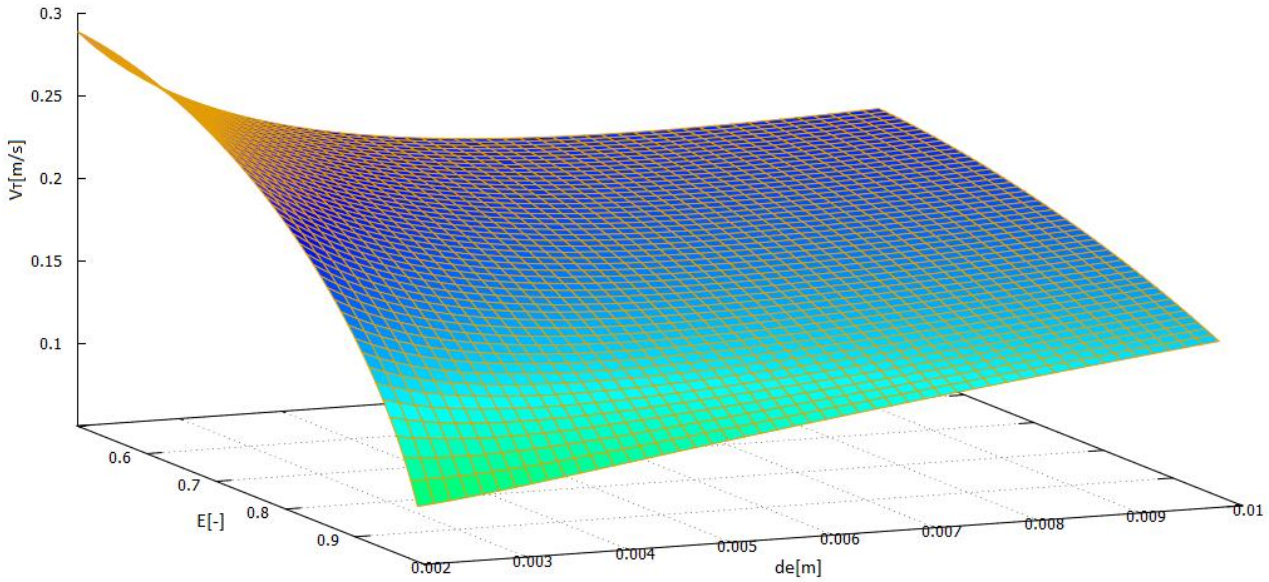

Figure 6.21 3D plot of the effect of the aspect ratio and bubble size on the terminal rising velocity for the rise of single bubble in stagnant water

From these graphs, some conclusions can be drawn that the aspect ratio of bubble shape has a more powerful impact on the small bubbles than the large ones. For the spherical bubbles the terminal velocity increases with the increasing bubble diameter. However, when the bubble deforms severely, the rule doesn't fit.

6.3.2. Operating Pressure

As analyzed in the chapter 7.3.1 and indicated in Figure 6.22 that the operating pressure doesn't have any effect on the terminal velocity and the bubble aspect ratio. It can also predict that, the operating pressure won't have any effect on the shear stress along the membrane created by the rise of a single bubble either.

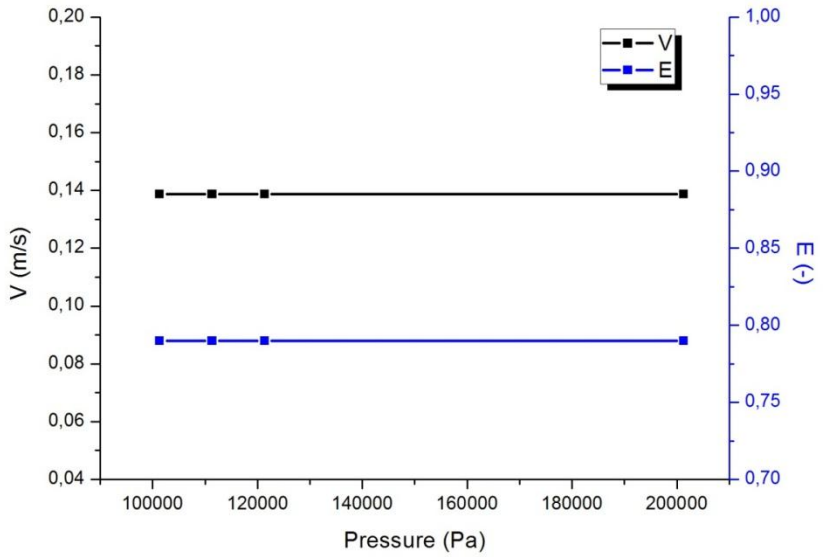

Figure 6.22 The effect of operating pressure on the terminal velocity and the aspect ratio

6.3.3. Viscosity

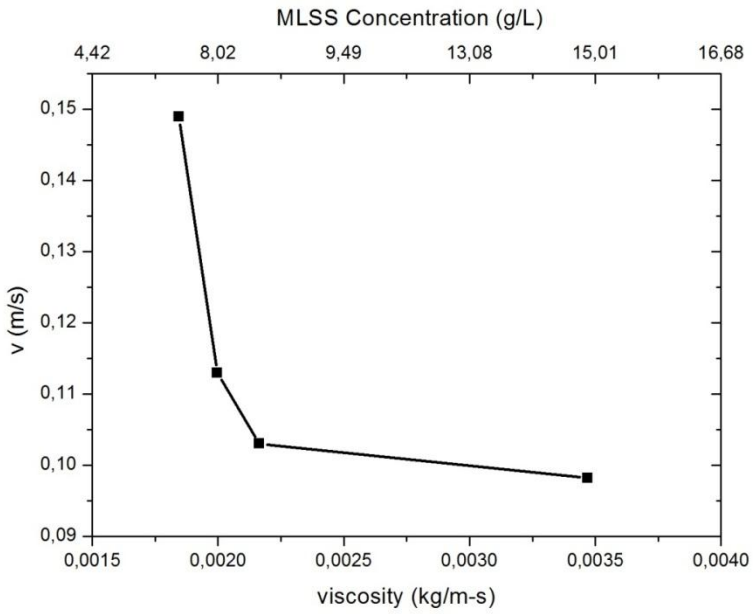

Figure 6.23 The effect of viscosity on the terminal velocity and the aspect ratio

As discussed in the chapter 5, there are so many expressions of the relationship between MLSS concentration and viscosity of the fluids. In this simulation the equation from Krauth et al. (1993) [79] was applied because the viscosity measured by vertical ball falling viscometer which doesn't involve the shear rate and this formula doesn't involve the shear rate either. In the simulation 0.001844 kg/m • s, 0.001997 kg/m • s, 0.002164 kg/m • s and 0.003468 kg/m • s were chosen because they stand for the MLSS concentration of 7 g/L, 8 g/L, 9 g/L and 14.9 g/L respectively. The results of the viscosity effect or the MLSS concentration effect on the terminal velocity was displayed in Figure 6.23. The terminal velocity decreases with increasing MLSS concentration and increasing viscosity.

6.3.4. Temperature

Temperature is a very important parameter for the dynamics of bubbles. It affects not only the viscosity of the fluids, but also the surface tension. The surface tension water differs slightly with temperature from 274 K to 303 K. And the equation between the surface tension and temperature of a solution is very complicated. So the surface tensions for all the simulations stay the same. This study doesn't include the effect of temperature on surface tension. And the effect of temperature on the terminal velocity, the bubble shape aspect ratio and the shear stress on the membrane may be not that much reliable.

The equation used for the viscosity in the last section is the following expression:

$$\mu = \mu_w \cdot 1.044625 \cdot e^{0.081151MLSS} \tag{6-5}$$

In this equation the temperature effect is neglected. But the temperature plays a very important part in the viscosity of the fluids, as indicated in the equation 6-5 (from Wikipedia).

$$\mu_w = 2.414 \times 10^{-5} \times 10^{247.8/(T-140)} \tag{6-6}$$

To assess the temperature effect on the water and sludge with the MLSS concentration of 8 g/L, 274 K, 283 K, 293 K and 303 K were chosen for the simulation. These temperature values cover the temperature range in a MBR system during all the seasons in the whole year.

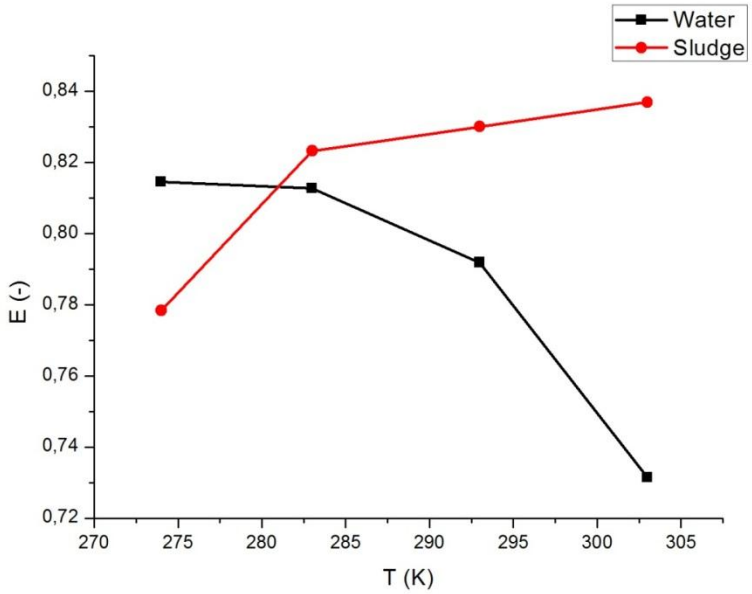

Figure 6.24 The effect of temperature on the terminal velocity for water and sludge

The results of the effect of temperature on the terminal velocity and the bubble aspect ratio of water and sludge were displayed in Figure 6.24 and in Figure 6.25 respectively. As indicated in Figure 6.24, temperature has a similar effect on the terminal velocity both for water and sludge. The velocity becomes lower as the temperature becomes higher, which lead to an increasing terminal velocity. However, for bubble aspect ratio in water and sludge it shows different trend.

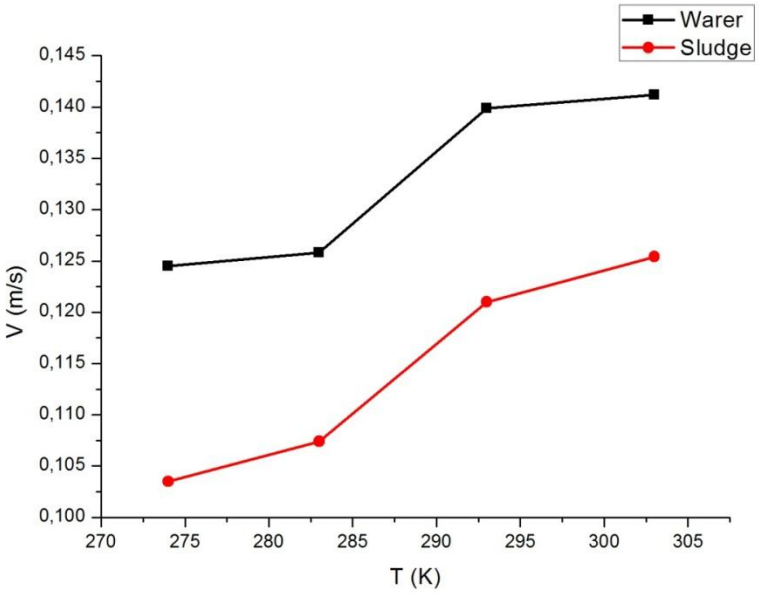

Figure 6.25 The effect of temperature on the aspect ratio for water and sludge

6.3.5. Initial Velocity

The bubble was patched with different initial velocity in the simulation in the beginning. But as shown in the following figure, the initial velocity of bubbles doesn't have any effect on the bubble motion. Because in the simulation the bubble was patched in the stagnant water, the bubble has the initial velocity as patched at the first step. But after a few steps, the velocity becomes 0 because the water velocity is 0. It's just like a bubble without any velocity was patched in the simulation. So it looks like the initial velocity doesn't have any effect on the bubble motion.

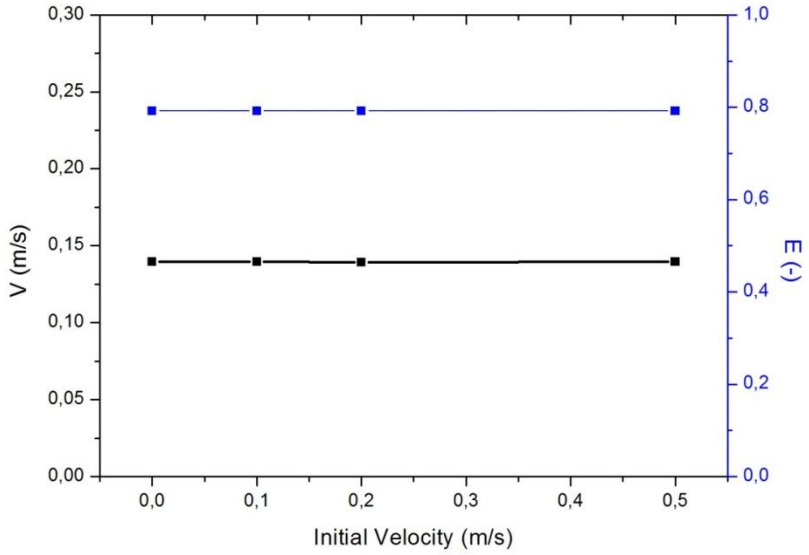

Figure 6.26 The effect of initial velocity on the terminal velocity and bubble aspect ratio

6.3.6. Gap Width

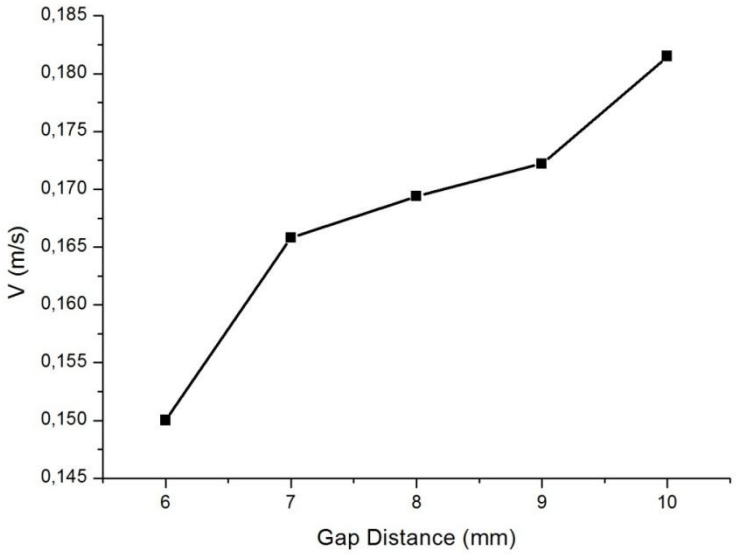

Figure 6.27 The effect of gap width on the terminal velocity in two models

As analyzed in the chapter 4 the geometry affects the results greatly. Two different models were applied to assess the gap width effect. One model has the domain with quadrate cross-section; the other one has a domain with fixed length of 8 mm. The numerical results for both cases have a huge difference between narrow channels and for the wide gap the results are about the same (not shown here). That means that small domain rather than large domain has a more powerful influence on the simulation. And the results are not reliable. So the models with a fixed length of 5D and the variable widths of 6 mm, 7 mm, 8 mm, 9 mm, 10 mm respectively are applied for the simulation to study the effect of gap width on the terminal velocity. The terminal velocity shows clearly a rising trend in respect of gap distance.

6.3.7. Fluid Velocity

The effect of the velocity of the fluid around the rising bubble was investigated in this section. The bottom of the domain was set as velocity-inlet. The fluid velocity will nearly equal to the inlet velocity with enough time steps. The result of this effect was graphically shown in the following figure.

The absolute bubble rising velocity shows a linear dependence on the velocity of fluid around the bubble. But the relative terminal rising velocity stays the same.

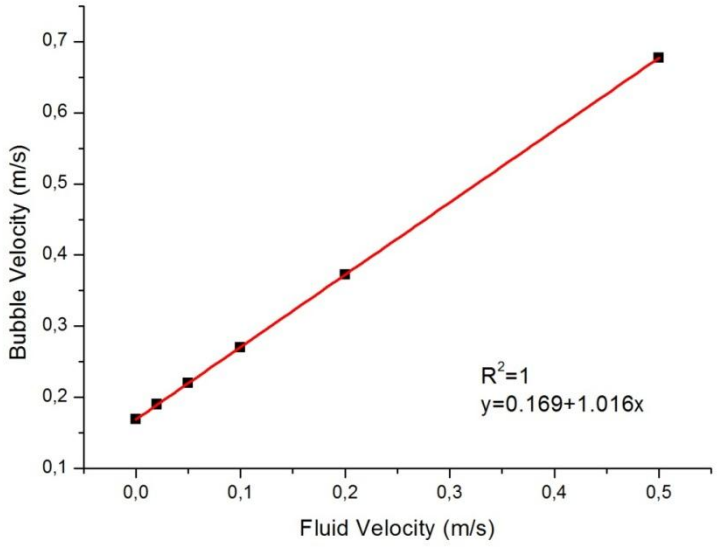

Figure 6.28 The effect of fluid velocity on the bubble terminal rising velocity

6.4. Trajectory of Bubble

The trajectory paths of rising bubbles for small and large bubbles are shown in the following two figures. Small bubbles tend to have a spherical shape. The motion of this bubble with small deformation is apt to be zigzag, whereas the motion of large bubbles with ellipsoid shape tends to be helical. This behavior of bubbles is also reported in previous literature [83, 91]. However, it should be noticed that the two graphs above don't have the same scale. The bubble trajectory in the second graph will become a straight line, if it has the same scale as in the first one. From this point, it may be concluded that the large bubbles are apt to swing less severely.

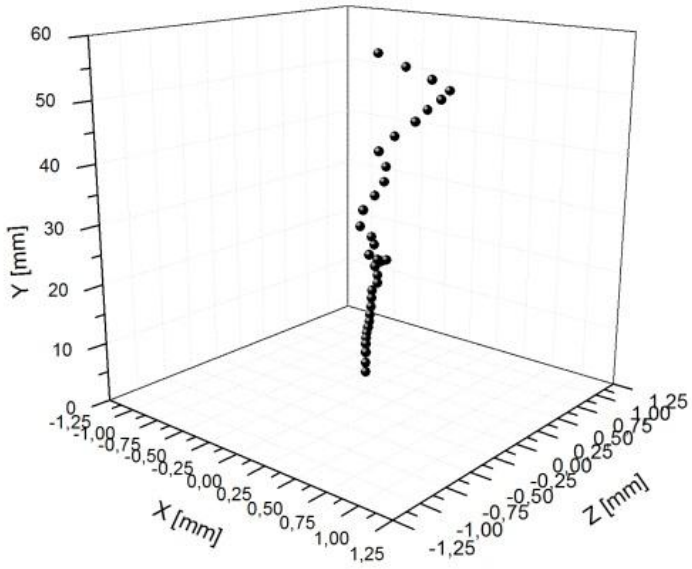

Figure 6.29 The path of a smaller bubble

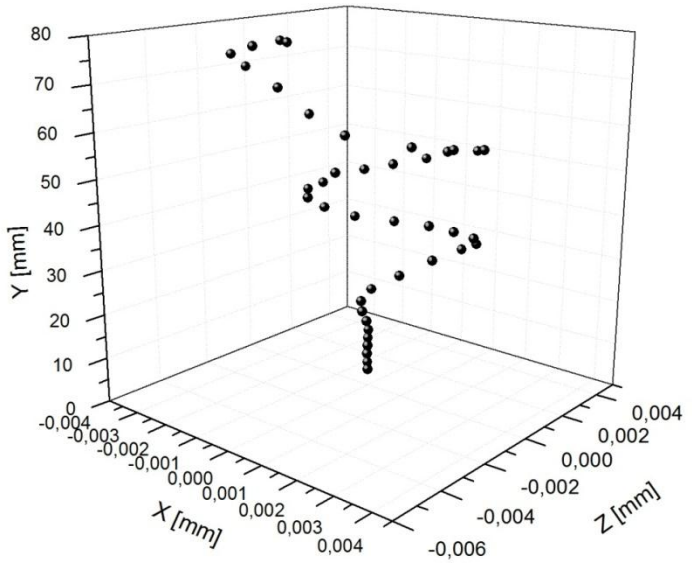

Figure 6.30 The path of a larger bubble

The trajectory of bubbles doesn't only indicate the bubble dynamics, but also has a powerful effect on the shear stress. Two simulations of the rise of the bubble diameter of 2 mm were carried out in this study. In one of them the bubble swings less severely, and in the other one the bubble moves more freely. The values of wall the shear stress are very different for the two simulations. It shows that the maximal shear stress is about 0.227 Pa induced by the bubble with more free movement. This value is about three times higher than that induced by the bubble, which swings less severely. And it is also greater than the wall shear stress induced by a 3 mm bubble.

6.5. The Affecting Factor of Shear Stress

In the following section, the shear stress profile induced by the rise of a single bubble was firstly presented. Then the effect of parameters, e.g. the operating pressures, bubble sizes, temperature, the

viscosity of the fluid, the gap distances of the membranes, the velocity of the fluid on the shear stress on the membrane surface were investigated respectively.

6.5.1. Shear Stress Profiles

Figure 6.31 shows the shear stress distribution on the whole membrane surface with respect to the bubble position. It is obvious that the shear stress near the bubble is the much higher. At the top part of the membrane surface the shear stress is nearly 0 Pa. That means the bubble movement along the membrane doesn't have much influence on this part. However, the influence was stronger in the part below the bubble location. It is also revealed in Figure 6.31 that the maximal shear stress occurs almost at the same height of bubble location. It is always less than 1 mm lower than the center of the bubble. The relationship between the position where the maximal shear stress occurs and the bubble center was demonstrated in Figure 6.32. It shows a very good linear dependence.

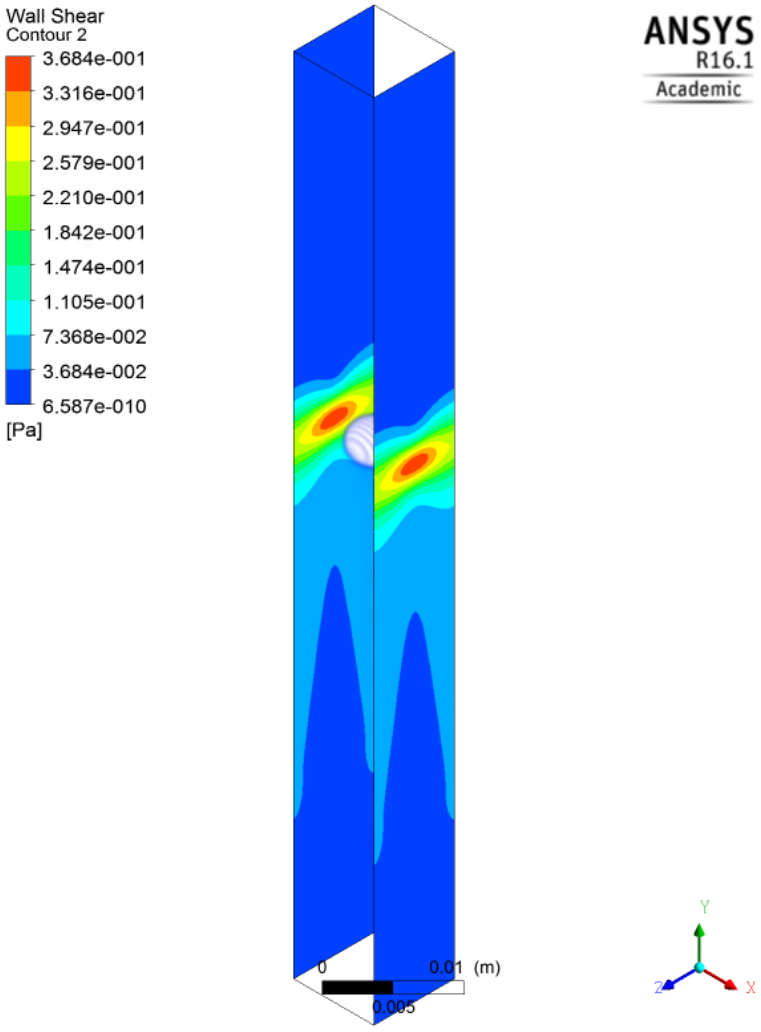

Figure 6.31 Wall shear stress contour along membranes

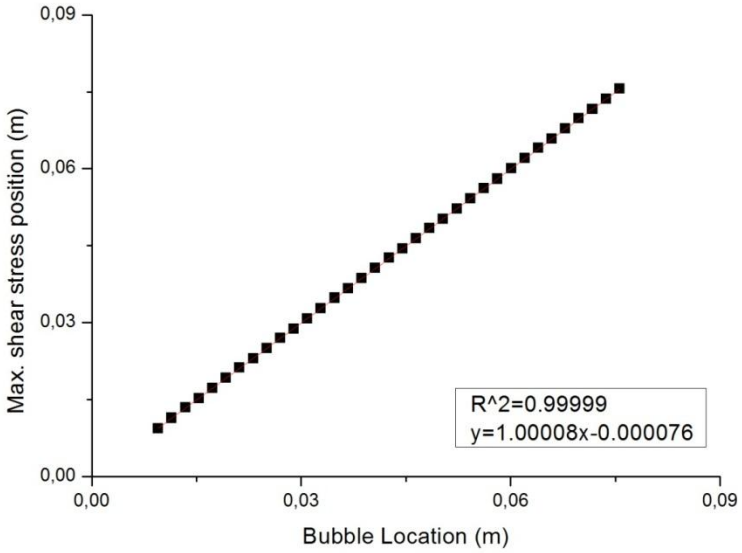

Figure 6.32 The position of max. shear stress vs. bubble vertical position

The shear stress distribution profile was reflected in Figure 6.33. The shear stress was from 0 to 0.5 Pa, which has a same magnitude with the experimental results obtained by previous researchers ([6]). Shear stress values are much higher at the bubble location. This is also agreed with the contour pictures of the wall stress distribution in the Figure 6.31. It is generally accepted that the shear stress on the membrane contributes to the flux enhancement at the filtration and the shear stress values induced by bubbles are much higher. The values in a two-phase flow can be at least three times higher than that in a single-phase flow [92].

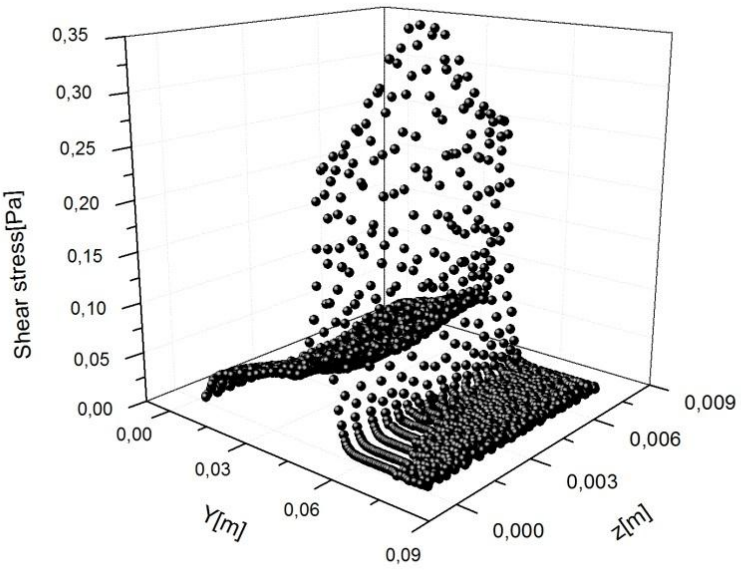

Figure 6.33 Wall shear stress distribution along one of the membranes

The relationship between shear stress at the membrane and the velocity near the membrane was shown in the following below:

$$\tau_w = \rho u_\tau^2 \tag{6-7}$$

This equation also indicates that the maximal shear stress occurs where the bubble appears. The gap distance between the bubble and the membrane is much smaller than the gap distance of the membranes. Based on the following equation, the velocity at the place where the bubble appears is much higher. Therefore, the value of the wall shear stress is much higher than that at any other locations. Thus the maximal shear stress always occurs at the location near the bubble.

$$u = \frac{Q}{A} \tag{6-8}$$

From the analysis above the relationship between the locations of the maximal shear stress at the membrane and the bubble vertical positions is already known. And in the graph above, it shows how the bubble horizontal position affects the shear stress. Actually, this effect is minor when we compare the value of the maximal shear stress (about 0.35 Pa) and the value of the maximal shear stress difference between the two membranes (about 4×10^{-5} Pa). However, in Figure 6.34 it shows clearly that the difference of the maximal shear stress is related to the horizontal location of the bubble. The peaks of the two curves in the graph occur at the same time.

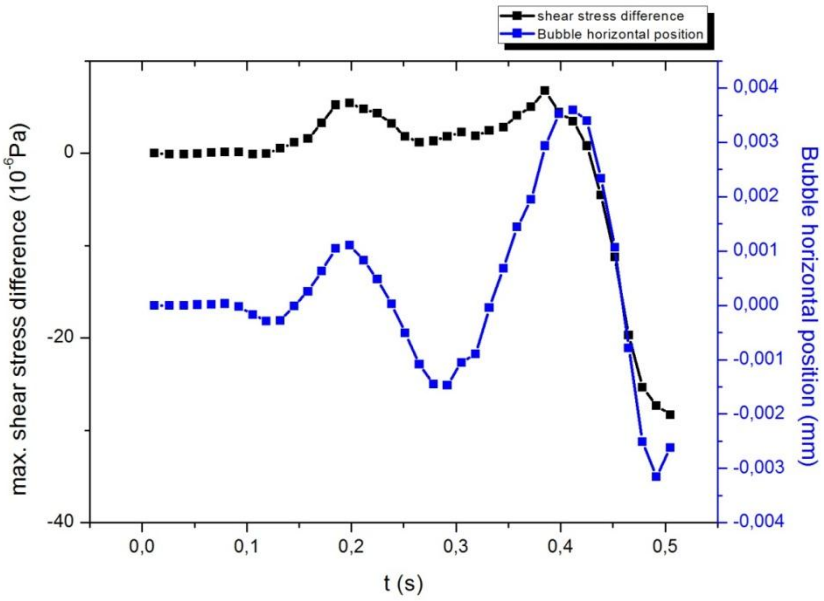

Figure 6.34 Comparison of the max. shear stress difference of two membranes against the bubble horizontal position

y^+ is a very important parameter to evaluate the simulation, as we already analyzed in the chapter 5. And from the numerical results it is noticed that the maximal y^+ and the maximal shear stress occurred always at the same time. To investigate the relationship of the maximal shear stress and the maximal y^+, the figure was made, from which it can be seen that the shear stress has a quadratic dependence on y^+. This relationship can be theoretically proved as well.

$$\tau_w = \rho u_\tau^2 \tag{6-9}$$

$$y^+ = \frac{\rho u_\tau y}{\mu} \tag{6-10}$$

Where τ_w is the wall shear stress; u_τ is the velocity near the wall; y is the distance of the center of the first cell to the wall. In this simulation the mesh size is set to be 0.2 mm. Therefore, y equals to 0.1 mm. Using the same values of the fluid density $\rho = 998.2\ \mathrm{kg}/m^3$ and the viscosity of the fluid $\mu = 1.003 \times 10^{-3}\ \mathrm{kg/m \cdot s}$ as in the simulation, following equations can be obtained, which also indicated the quadratic relationship between the wall shear stress and y^+.

$$\tau_w = 0.101 \times (y^+)^2 \tag{6-11}$$

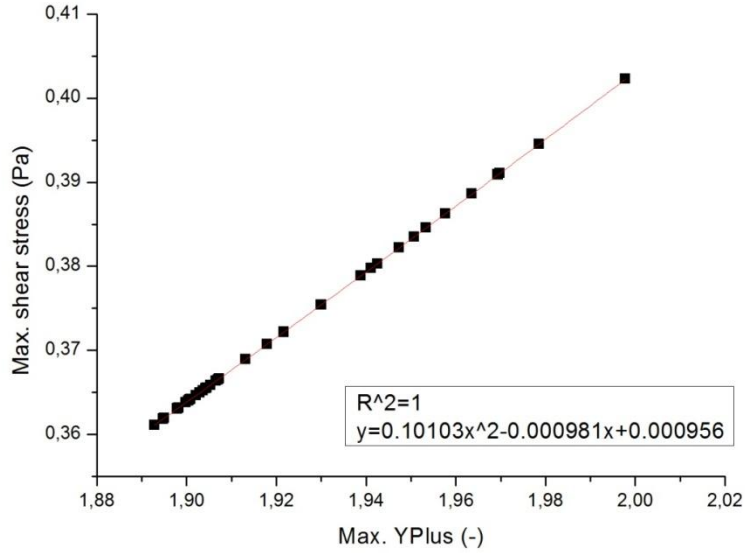

Figure 6.35 The relationship between max. shear stress and max. y^+

Comparing the theoretical equation and the equation obtained from data fitting in Figure 6.35, a very good agreement was achieved.

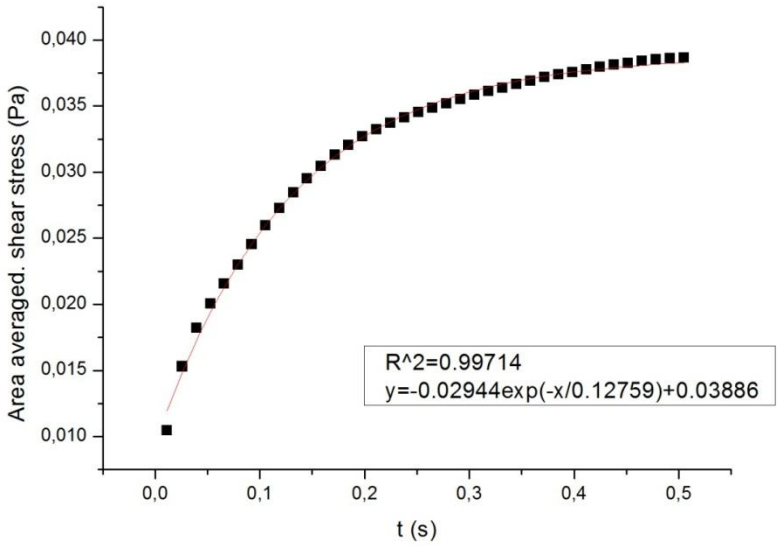

Figure 6.36 Time dependent area averaged shear stress induced by 4 mm bubble

A 4 mm bubble was patched in the stagnant water. At first the bubble starts to rise, the mixing behavior of the fluids starts increasing quickly. So is the water velocity near the wall. Based on the relationship between the shear stress and the velocity, the area averaged shear stress increased quickly at the beginning. Then the bubble becomes stable, rising with a relatively constant terminal velocity and its influence area on the membrane also becomes relative constant, as shown in the counter graph of the wall shear stress. Therefore, the area averaged shear stress on the membrane increases very slowly with the increasing time. The area averaged shear stress function of time was shown in the figure above by data fitting. And it also shows clearly that they have a very good correlation.

6.5.2. Bubble Position in 2D Simulation

The 2d simulation was an examination of the bubble rising into and out of the gap of the membranes. The averaged shear stress of each plate was displayed in Figure 6.37. It is obvious that the shear stress is much larger when the bubble is between the two plates. Before it reaches the channel the shear stress is about 0 and when it gets out of the channel it still has some influence on the shear stress but the influence is very small. Compared to the two models, the results obtained from the model with structured grid doesn't show any trend, but the results of the other model show that the shear stress increases until it reaches its maximum, and then it decreases to about 1.6 Pa and the stays there although with fluctuation. The model with finer mesh size at the first layer is more reliable, as analyzed in the chapter 4. It is believed that the bubble has more influence on the shear stress when it rises into the channel rather than gets out of the channel.

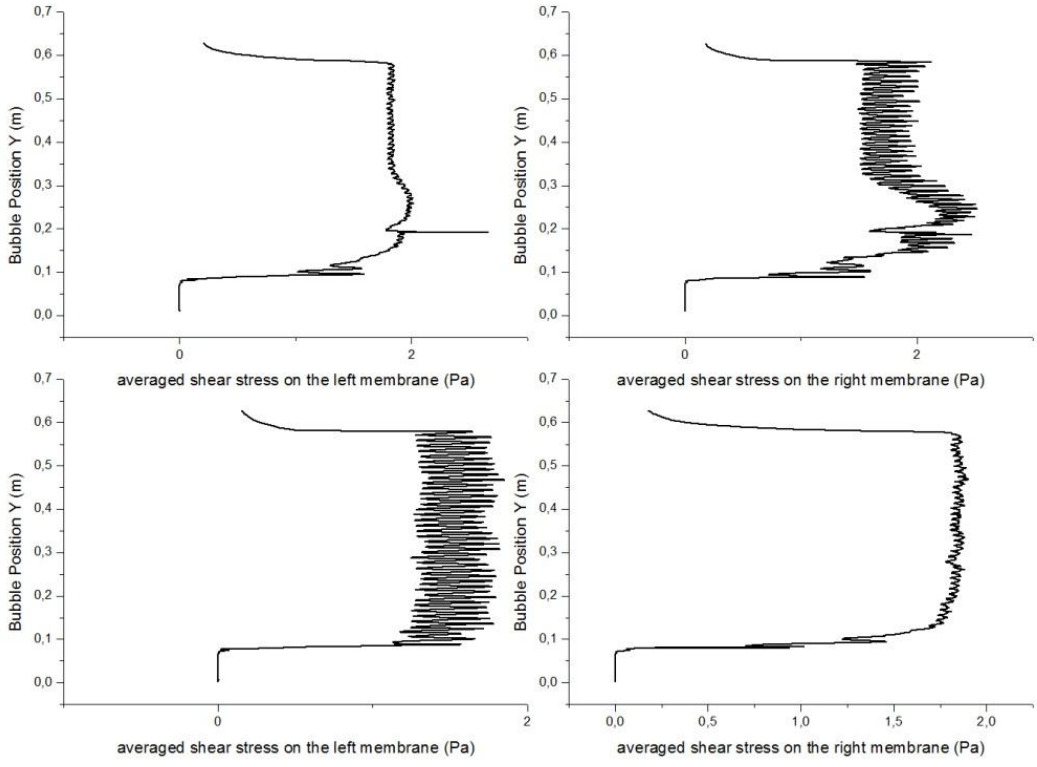

Figure 6.37 The averaged shear stress of each plate for models with two meshes (above: unstructured grid with finer element size near the wall; below: structured grid)

In Figure 6.37 we can observe the fluctuation of shear stress on each membrane. The following picture shows that the bubble position in the horizontal direction has a great effect on the shear stress of each membrane. It is obviously shown in the figure that the shear stress reaches its maximum when the bubble is nearest to the membrane and the shear stress decreases with bubble moving away from the membrane.

It is worth mentioning that in Figure 6.37 and Figure 6.38 huge difference exists in the fluctuation of shear stress on the left membrane and on the right membrane. In order to find out why there is such a difference the following figure was made. It is observed from the figure combined with some pictures that the bubble touches one of the plates and then moves away from it repeatedly. When it touches the membrane, the maximum of shear stress occurs. The shear stress decreases with the bubble moving away from the membrane. As for the other membrane, the bubble doesn't touch it and the distance between the bubble and the membrane keeps changing, so that the shear stress changes correspondingly but with less fluctuation. Figure 6.38 also shows the effect of the plates on the bubble movement. Without the plates the bubble moves more freely.

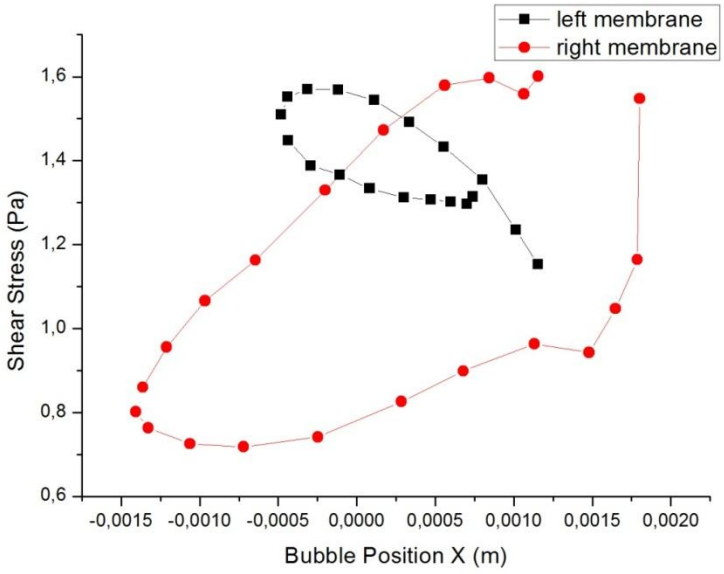

Figure 6.38 The averaged shear stress of each plate in one period

From the graph above, we can see that the bubble bounce against one of the membranes repeatedly. The phenomena of bubble bouncing against the vertical wall is also modeled and validated by the experiment by B.Podvin et al. [93]. They proved that the bubble will be repeated bouncing the wall when the wall inclination is greater than 55°. And it is also can be observed from the experimental results by Vires [88], the bubble in the experiment bounced against one of the walls repeatedly.

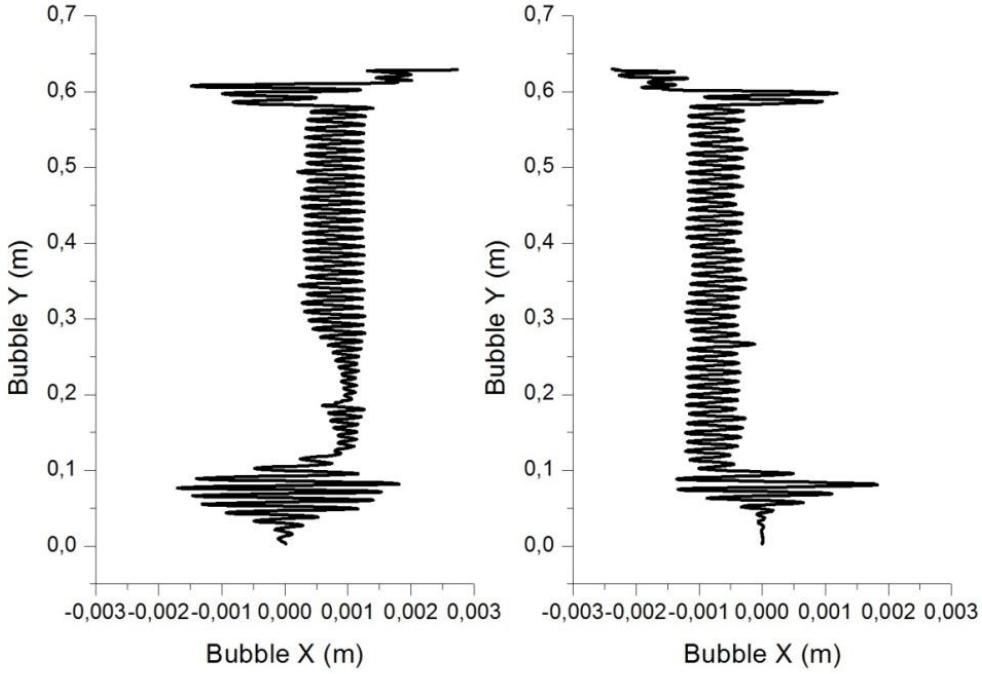

Figure 6.39 Bubble path for both models (left: unstructured grid with finer element size near the wall; right: structured grid)

6.5.3. Bubble Size

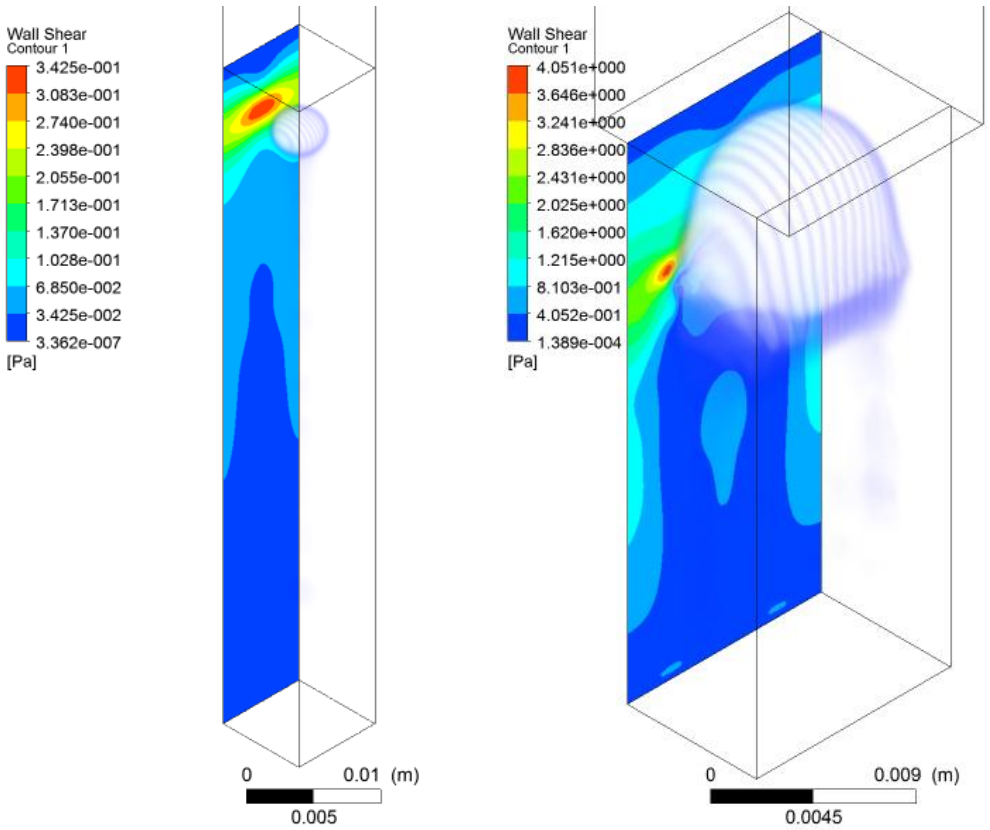

Figure 6.40 Comparison of the wall shear stress distribution induced by a 4 mm single bubble (left) and by a single bubble with an equivalent diameter of 9.8 mm (right)

The left picture shows the wall shear stress distribution induced by a 4 mm single bubble, whose size is smaller than the gap distance of membranes. The wall shear stress distribution on the right site was obtained from a very large bubble, which has an equivalent diameter larger than the membrane gap distance. The shape of the two bubbles was already quite different. The small bubble has a nearly spherical or ellipsoidal shape, whereas the large bubble is a typical Taylor bubble with a shape of spherical cup. The small bubble and the large bubble belong to different shape regime and the shear stress distributions caused by the two bubbles are definitely quite different, as shown in the figure above.

It is also worth mentioning that the scales of wall shear stress in the two cases above are different. The maximal shear stress induced by the large bubble is at least ten times higher than that obtained from the small bubble. If the two pictures are on the same scale of wall shear stress, it will be clearly seen that, the area of high shear stress in the model with larger bubble is much higher than the value in the model with small bubble.

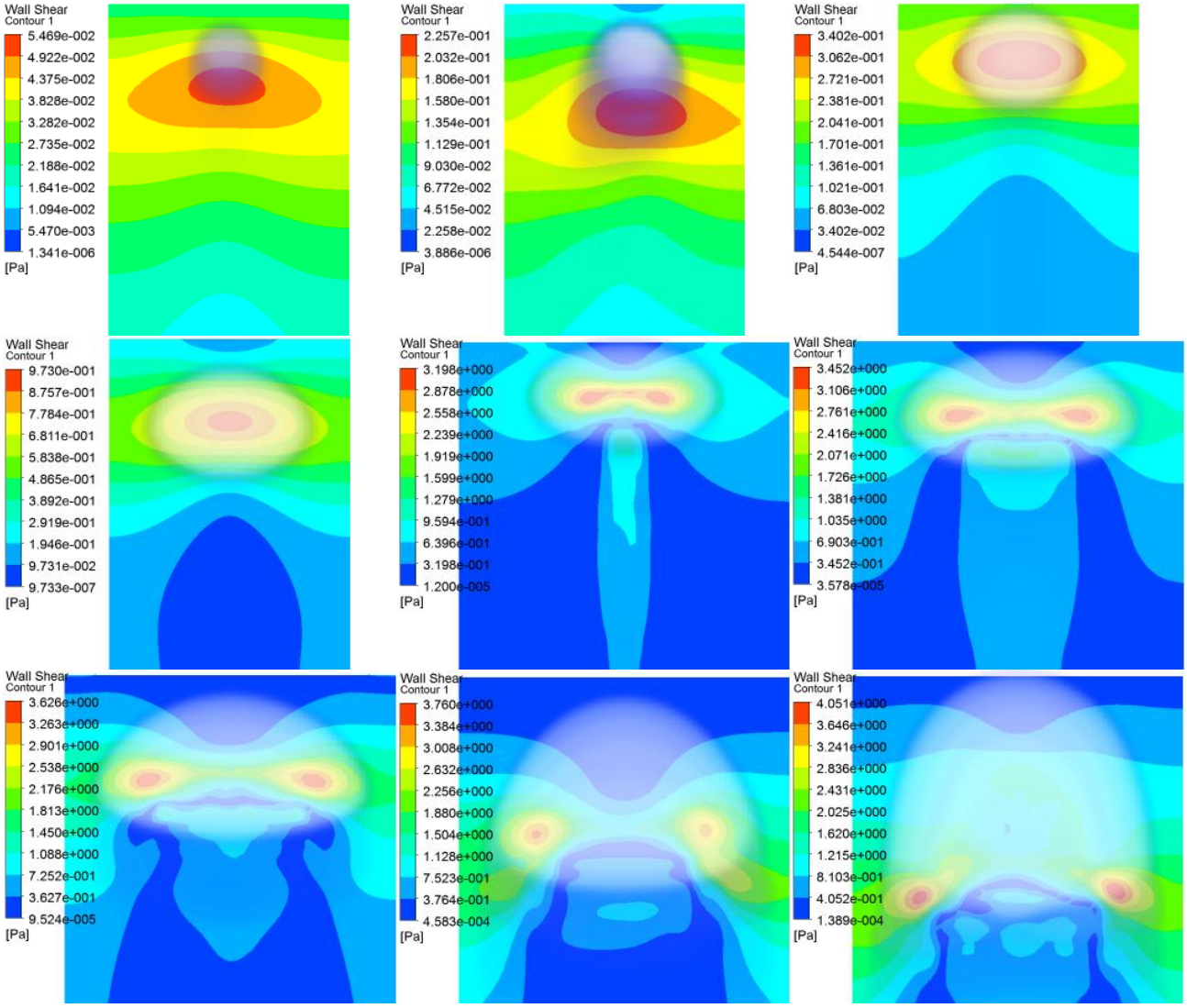

Figure 6.41 Wall shear stress distribution on the membrane induced by bubbles with different diameters (2 mm; 3 mm; 4 mm; 5 mm; 6 mm; 7 mm; 8 mm; 8.93 mm; 9.8 mm respectively)

All the pictures in the figure show the wall shear stress distribution on the membrane. Comparing the legends on the left side of each picture, we can know that the maximal shear stress improves with the increasing bubble size and it increases quickly at first when the bubble size increases, but at a certain

bubble size the shear stress increases very slowly with increasing bubble size. This phenomenon also agrees with the studies by Ndina et al. [94] and by H. Prieske et al. [92]. They also found out that the shear stress increases when the bubble size increases. For all the maximal shear stress it occurs where the bubble appears. For small bubbles with a size of less than 6 mm, the maximal shear stress only occurs in the middle of the gap. For large bubbles with the size equals to and greater than 6 mm, the maximal shear stresses exist both on the left and the right side of the gap. When the bubble's shape is ellipsoidal, the two maximal shear stresses occurred at the center of the bubble in the vertical direction. But for the bubbles with the shape of spherical cup, they occurred at the bottom of the bubble. And it shows clearly that at the top of large bubbles, the value of shear stress is low.

The relationship between the shear stress induced by the rise of a single bubble and the bubble size can be indicated and observed from the figure above. However, the exact relationship of them cannot be found out. So the following figure was made to study the exact relationship of shear stress and bubble size.

Since the bubbles belong to another regime at the diameter larger than 6 mm. So bubbles with a diameter from 2 mm to 6 mm are chosen to investigate the effect of small bubble sizes on the shear stress, as shown in Figure 6.42. The effect of large bubbles with the diameter equal to and greater than 6 mm on the maximal shear stress is also studied; the relationship was shown in Figure 6.43.

Comparing the two graphs, a very good correlation between data for both cases can be observed. And the maximal was shear stress shows an exponential dependence on the bubble diameter for both large and small bubbles. However, the formulations for both cases are not the same. For small bubbles the shear stress increases very quickly with the increasing bubble size. However, at the bubble size of 6 mm, the increasing rate slows down. It still increases when the bubble becomes larger. However, compared to the growth rate of small bubbles, the growth rate for large bubbles is really low.

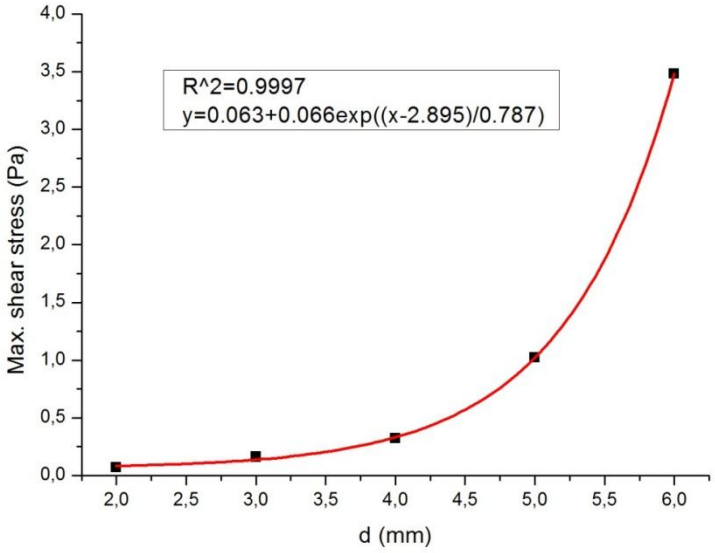

Figure 6.42 The relationship of shear stress and bubble size for small bubbles

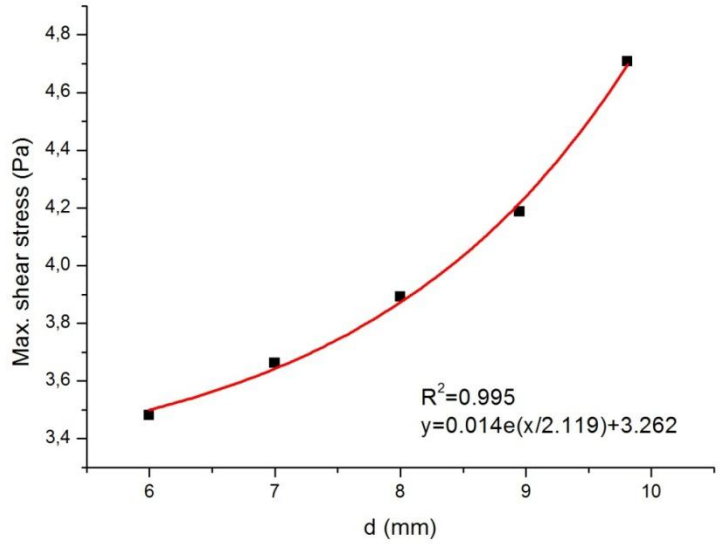

Figure 6.43 The relationship of shear stress and bubble size for large bubbles

6.5.4. Operating Pressure

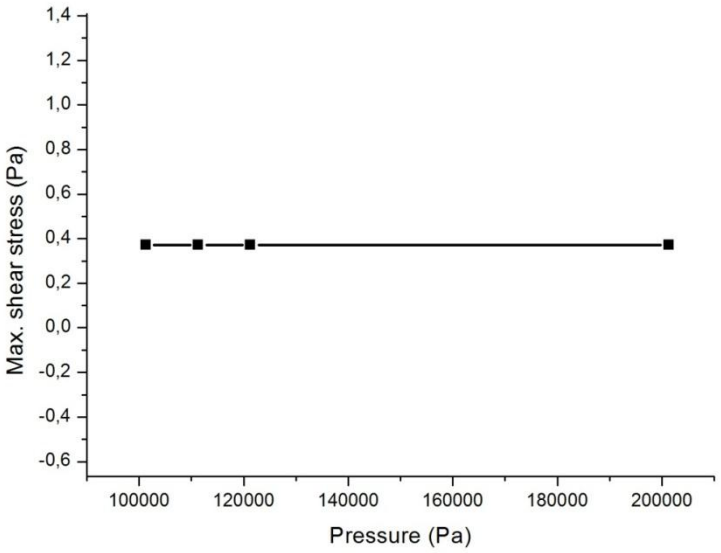

Figure 6.44 The effect of operating pressure on the maximal shear stress

As analyzed in the section of 7.2.1, the operating pressure won't have any effect on the bubble aspect ratio, the terminal rising velocity and the shear stress on the membrane. Because the pressure, which is applied to the gas phases in the simulation, is like adding a very high gas column at the top of the water surface to the atmosphere. The gauge pressure at the same pressure outlet will be 0 Pa, no matter how high the pressure was set at the operating pressure. So the curve in the following graph is so.

6.5.5. Viscosity

0.001844 kg/m • s, 0.001997 kg/m • s, 0.002164 kg/m • s and 0.003468 kg/m • s which stands for the MLSS concentration of 7g/L, 8 g/L, 9 g/L and 14.9 g/L respectively, were chosen for the simulation to study the effect of viscosity or MLSS concentration on the shear stress. This effect was shown graphically in the figure below. The shear stress decreases with increasing MLSS concentration and increasing viscosity. However, at the viscosity of 0.003468 kg/m • s the shear stress for this simulation shows a high fluctuation. The averaged shear stress depends greatly on the shear stresses which are chosen.

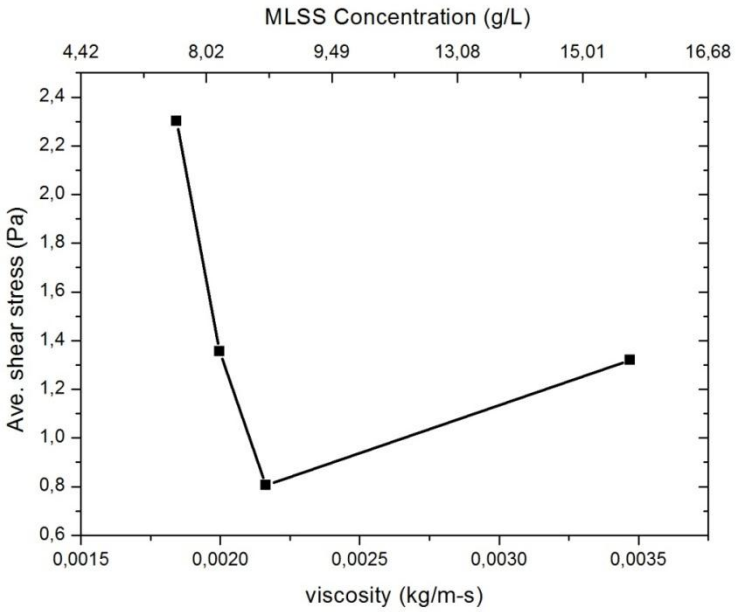

Figure 6.45 The effect of viscosity or MLSS concentration on the shear stress

As shown in the figure above, the shear stress decreases with the increasing viscosity. But at a certain viscosity the shear stress starts to increase. This trend could be explained by the following expressions.

$$y^+ = \frac{\rho u_\tau y}{\mu} \tag{6-12}$$

$$\tau_w = \rho u_\tau^2 \tag{6-13}$$

$$u^+ = \frac{\bar{u}}{u_\tau} \tag{6-14}$$

Based on the boundary theory and the small value of y^+, the following relation between u^+ and y^+ can be obtained:

$$u^+ = y^+ \tag{6-15}$$

Based on all the equations above, we can get the equation showing the relationship between the wall shear stress and the viscosity μ, the averaged velocity $\bar{u}$.

$$\tau_w = \frac{\mu \bar{u}}{y} \tag{6-16}$$

So when the viscosity increases, the velocity decreases. The change of velocity is greater than the change of viscosity. It is the velocity that domains in this relationship. Therefore, the wall shear stress decreases with the increasing viscosity. But above a certain viscosity, the effect of viscosity is more powerful than the effect of velocity on shear stress. So, the wall shear stress will increase with the increasing viscosity, which matches the trend shown in the figure above.

6.5.6. Temperature

As mentioned in the section where the effect of temperature on the terminal velocity and the bubble aspect ratio was discussed, the UDF files for water and sludge are using two different equations, which are also given in that section. Based on these equations , temperature has only effect on the viscosity of the fluids. And the temperature effect on other parameters, e.g. surface tension is neglected in this study.

The trend above can be explained by the same reason in the section 6.5.6 as well, because temperature only changes the viscosity values. The viscosity of water and sludge belong to two different regimes. For water the increase of temperature may lead to a dramatic decrease of viscosity. Therefore the shear stress for water decreases with the increasing temperature. For sludge, the increase of velocity may be more powerful than the decrease of viscosity with increasing temperature. So the shear stress tends to increase with the increasing temperature for sludge.

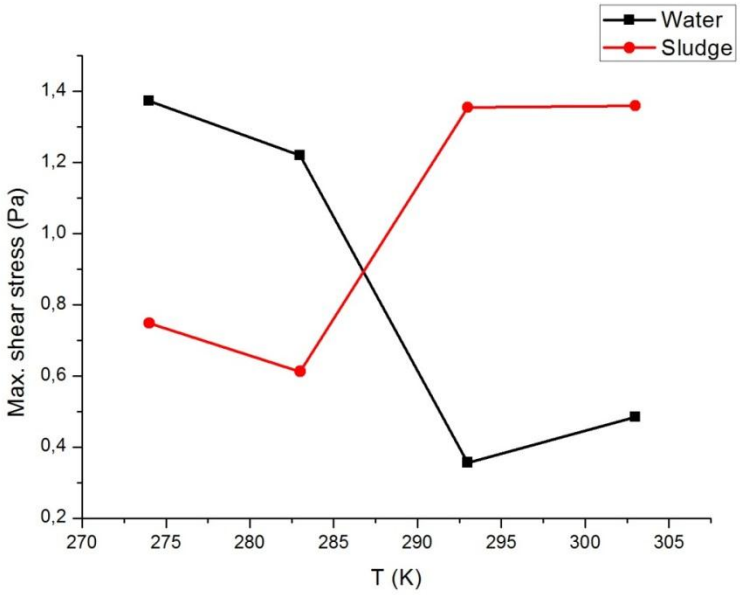

Figure 6.46 The effect of temperature on time averaged maximal shear stress for water and sludge

6.5.7. Gap Width

Different distances were set as 6 mm, 7 mm, 8 mm, 9 mm and 10 mm in the simulation to study the effect of gap width on the shear stress. The numerical results were graphically displayed in the following figure, from which we know that, the maximal shear stress decreases with the increasing gap distances for the rise of a 4 mm bubble. For the smallest gap width of 6 mm, the shear stress is the highest. The same conclusions were drawn by N.V.Ndinisa et al. [92] and by H. Prieskeet et al. [92].

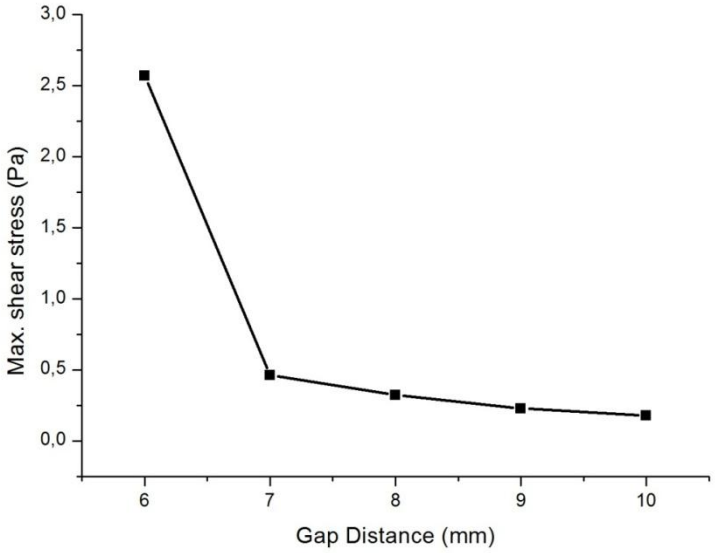

Figure 6.47 The effect of temperature on time averaged maximal shear stress for water and sludge

From this graph, it is recommended that the smallest gap width is applied to the MBR system to achieve the highest shear stress on the membrane and to gain the best cleaning effect in the filtration. However, when the gap distance is further decreasing, the gap between the membranes may be clogged by particles. But a gap width of 6 mm is still suitable for the MBR systems. So based on the simulation, the smallest gap distance can achieve the highest maximal shear stress. But in practice, considering the clogging problem, larger gap distances between two membranes are recommendable. In the study by H. Prieskeet et al. [92], it is recommended that the gap width of 5 mm should be applied to the MBR system. Therefore, the gap width of 5 mm and 6 mm is recommendable for the MBR system.

6.6. Shear Force in Escape Zone

As reported by the company, the membrane might be damaged by the shear force, when large bubbles rise out of the gap of membranes. In this section, the location where the maximal shear stress occurs during the rise of the bubble was firstly confirmed. Secondly, different distances from the upper edge of the membrane to the water surface were set to study its effect on the shear force. Then three different areas were patched on the membrane surface to calculate the shear force on them. The effect of bubble size, the effect of gap distances and the effect of the fluid velocity on the shear force in the escape zone were investigated in the following subsections.

6.6.1. Bubble Y Position

As shown clearly in the last section, the shear stress near the bubble is the much higher and the maximal shear stress occurs almost at the same height of bubble location. And in the escape zone, the maximal shear stress occurs where the bubble is as well. But when the bubble goes out of the gap of membranes, the maximal shear stress occurs always at the top of the membrane.

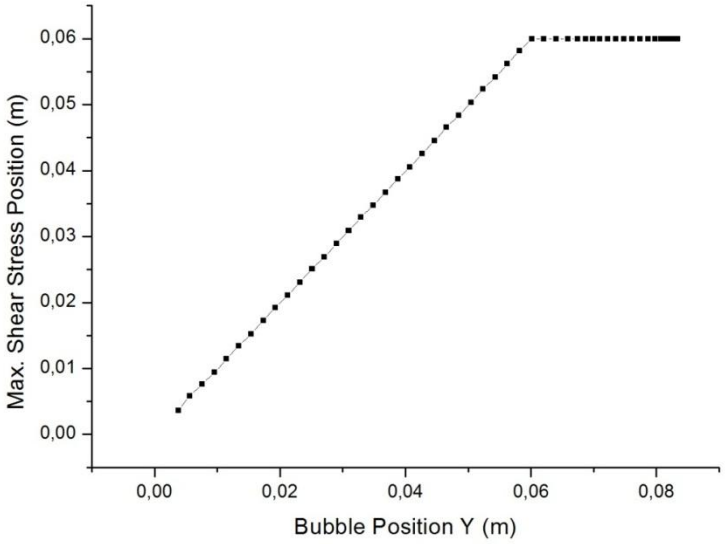

Figure 6.48 The relationship of maximal shear stress and bubble Y position in the escape zone

6.6.2. Distance between the Upper Membrane Edge and Water Surface

To investigate the effect of the distance between the upper boundary of the membrane and the water surface on the maximal shear force on the area of the membrane upper part. Different distances e.g. 10 mm, 20 mm, 30 mm, 40 mm and 50 mm above the membrane edge were set to carry out the simulation. Then the shear forces on three different areas were calculated at each time step. At last the maximal shear force of each area was chosen to compare with the maximal shear force in other cases. The data were shown in the following table. And it shows clearly that the effect of the distance between the upper boundary of the membrane and the water surface is minor.

The shear stress profiles against the bubble position for all the cases are almost the same, which further proved that the effect of the distance between the membrane top and water surface is minor. However, from the graphs, it is also clearly seen that there is a jump of shear stress when the bubble is near the upper edge of the membrane. That indicated that the upmost part of the membrane may be the most vulnerable to be damaged by the shear force induced by the bubble rise.

Table 6-12 The effect of the distance between the upper membrane edge and water surface on the shear force

Upper distance	10 mm		20 mm		30 mm		40 mm		50 mm	
Membrane Location	Left	Right	Left	Right	Left	Right	Left	Right	Left	Right
Max. Shear force [10^{-6} N](4×8 mm)	7.78	7.54	7.88	7.65	7.57	7.51	7.99	7.99	8.03	7.89
Max. Shear force [10^{-6} N](8×8 mm)	11.03	10.90	11.05	10.91	10.84	10.84	11.49	11.49	11.26	11.18
Max. Shear force [10^{-6} N](12×8 mm)	13.04	12.98	13.04	13.00	12.93	12.94	13.43	13.45	13.11	13.09

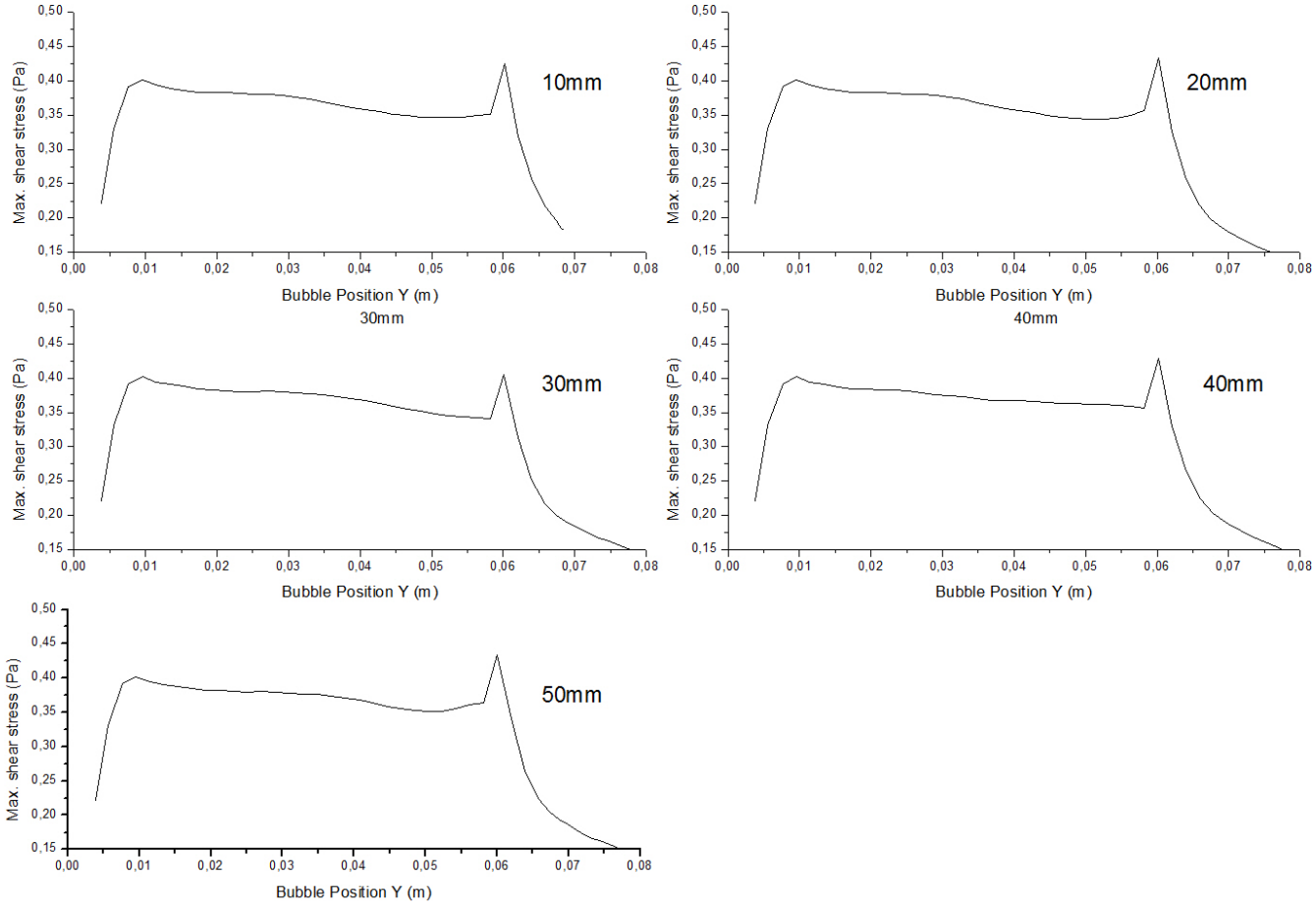

Figure 6.49 The shear stress profile against the bubble position for different distances between the membrane top and water surface

6.6.3. Bubble Size

The shear stress profiles for the bubbles with a diameter greater than 3 mm show the same trend. The value of shear stress increases at the beginning because the velocity of the fluid induced by the bubble motion is increasing. Then the bubble velocity reaches its terminal rising velocity. The velocity becomes stable, so was the shear stress. After the bubble moves out of the membrane channel, the shear stress decreases quickly.

For the small bubbles the trend is not the same. The reason may lie in the relative coarse mesh size for the small bubbles. It is not only because the trend is not the same with others. And the terminal rising velocities of small bubbles are quite different with others and they don't match the results from experiments. So the numerical values for small bubbles with a diameter of 2 mm or 3 mm are not reliable.

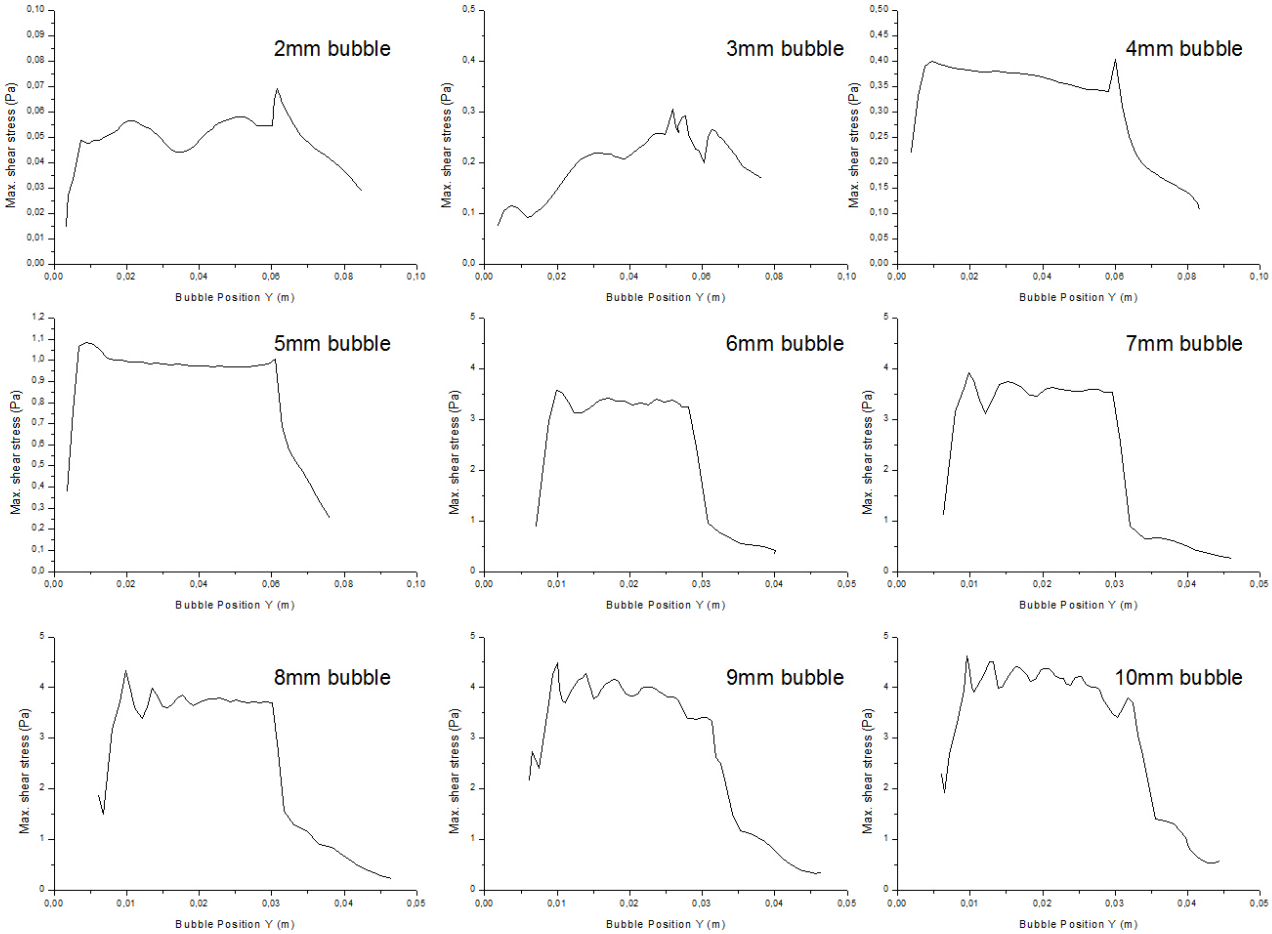

Figure 6.50 The shear stress profile against the bubble position for different bubble sizes

Table 6-13 The effect of bubble size on the shear force

Bubble Size	2 mm		3 mm		4 mm	
Membrane Location	Left	Right	Left	Right	Left	Right
Max. Shear force [10^{-6} N] (4×4 mm)	0.68	1.22	1.40	1.62	3.12	3.11
Max. Shear force [10^{-6} N] (8×8 mm)	2.39	3.14	3.96	4.37	7.70	7.72
Max. Shear force [10^{-6} N] (10×10 mm)	3.55	4.29	5.23	5.78	10.15	10.21
Bubble Size	5 mm		6 mm		7 mm	
Membrane Location	Left	Right	Left	Right	Left	Right
Max. Shear force [10^{-6} N] (4×4 mm)	7.13	7.76	14.93	14.92	26.17	26.77
Max. Shear force [10^{-6} N] (8×8 mm)	16.79	17.79	38.66	38.89	65.71	66.30
Max. Shear force [10^{-6} N] (10×10 mm)	21.73	22.80	51.00	53.71	86.36	85.24
Bubble Size	8 mm		8.95 mm		9.81 mm	
Membrane Location	Left	Right	Left	Right	Left	Right
Max. Shear force [10^{-6} N] (4×4 mm)	23.62	23.68	21.62	20.819	27.21	27.20
Max. Shear force [10^{-6} N] (8×8 mm)	71.58	72.47	66.79	65.75	81.74	82.36
Max. Shear force [10^{-6} N] (10×10 mm)	101.916	99.82	99.14	99.99	117.83	116.43

Bubbles with different diameters were patched in the model to study the effect of bubble size on the shear forces. The shear stress can be directly obtained from the simulation. However, the shear force cannot and it's area dependent. Therefore, three quadratic areas with the size of 4 mm, 8 mm and 10

mm respectively are set on the mid-upper part of membranes in order to calculate the shear force on these areas. The data were displayed in the following table and graphically shown in Figure 6.51.

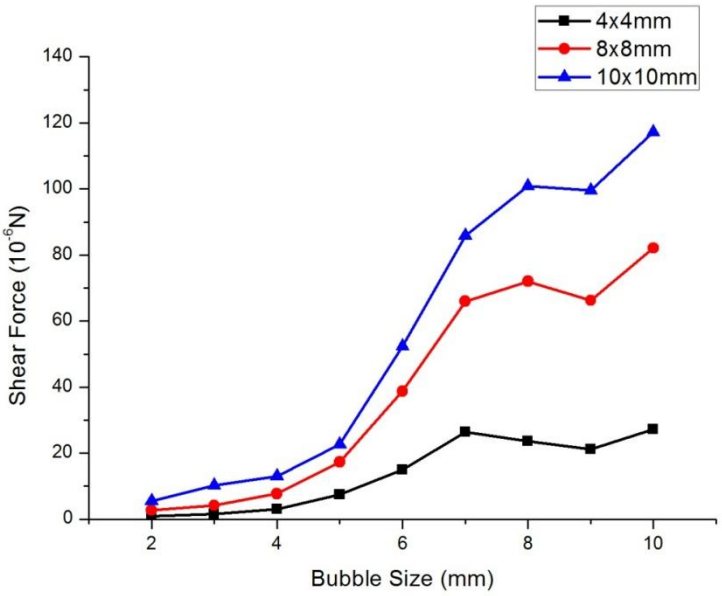

Figure 6.51 The effect of bubble size on the shear force for different areas

And it is obvious that the shear forces increased dramatically with the bubble size when the bubble is smaller than 7 mm. The shear forces for the bubble with diameter of 7 mm, 8 mm and 9 mm are almost the same. It doesn't increase like the smaller bubbles because of the existence of the membranes, which may restrict the bubble motion. However, at the bubble diameter of 10 mm, the shear force starts to increase again. The reason may lie in that the 10 mm bubble belongs to another shape regime and the effect of the bubble size domain again.

Table 6-14 The effect of bubble size on the maximal area averaged shear stress

Bubble Size	2 mm		3 mm		4 mm	
Membrane Location	Left	Right	Left	Right	Left	Right
shear force [Pa] (10 mm×5D)	0.035	0.043	0.050	0.053	0.080	0.079
shear force [Pa] (20 mm×5D)	0.026	0.029	0.033	0.034	0.052	0.052
shear force [Pa] (30 mm×5D)	0.018	0.020	0.023	0.024	0.037	0.037
Bubble Size	5 mm		6 mm		7 mm	
Membrane Location	Left	Right	Left	Right	Left	Right
shear force [Pa] (10 mm×5D)	0.145	0.148	0.295	0.283	0.424	0.424
shear force [Pa] (20 mm×5D)	0.100	0.102	0.229	0.224	0.310	0.316
shear force [Pa] (30 mm×5D)	0.071	0.072	0.152	0.155	0.243	0.237
Bubble Size	8 mm		8.95 mm		9.81 mm	
Membrane Location	Left	Right	Left	Right	Left	Right
shear force [Pa] (10 mm×5D)	0.518	0.519	0.578	0.553	0.596	0.627
shear force [Pa] (20 mm×5D)	0.396	0.400	0.494	0.472	0.526	0.522
shear force [Pa] (30 mm×5D)	0.285	0.294	0.336	0.331	0.401	0.400

Considering the affecting areas of wall shear stress induced by different bubbles are not the same, especially in the horizontal direction. So three other areas with the length of 5D, where D stands for the bubble diameter, were set on the upper part of membrane to calculate the shear force. The shear

forces on each area were not displayed, because they are not comparable, when the areas are not the same. Only the maximal area-averaged shear stress was displayed in the table above.

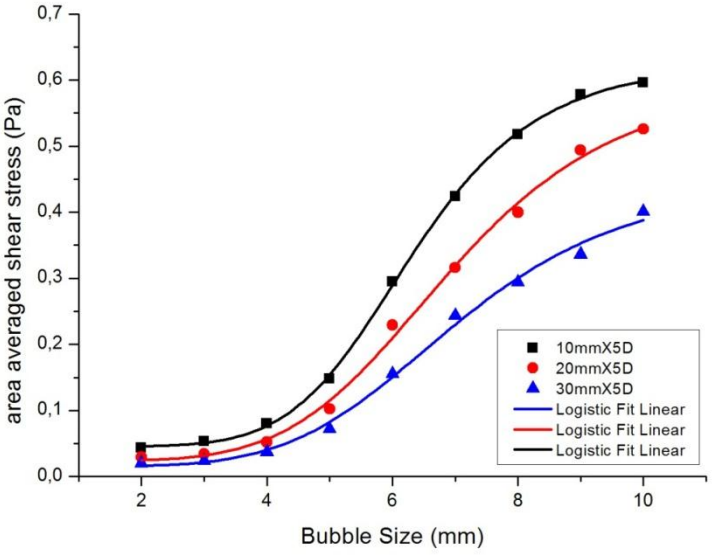

Figure 6.52 The effect of bubble size on the maximal area averaged shear stress for three different areas

From the curves in the figure, it can be seen that the area averaged shear stress increases with the increasing bubble size. The increasing rate increases at first until reaches its maximum, then it decreases again. It also shows clearly, that the data fit the equation very well. The fitted expressions and the correlation are displayed as below. Equation 6-17 and 6-18 are for the data obtained from the largest area, i.e. 30 mm×5D. Equation 6-20 and 6-21 are for the area of 30 mm×5D. The last two equations are for the smallest area.

$$y = 0.454 + \frac{(0.015-0.454)}{1+(\frac{x}{7.067})^{4.963}} \quad (6\text{-}17)$$

$$R^2 = 0.992 \quad (6\text{-}18)$$

$$y = 0.608 + \frac{(0.024-0.608)}{1+(\frac{x}{6.971})^{5.086}} \quad (6\text{-}19)$$

$$R^2 = 0.995 \quad (6\text{-}20)$$

$$y = 0.630 + \frac{(0.045-0.630)}{1+(\frac{x}{6.331})^{6.266}} \quad (6\text{-}21)$$

$$R^2 = 0.999 \quad (6\text{-}22)$$

It is known from these equations that the area averaged shear stress increases with the increasing bubble size. However, if the bubble diameter is infinite, the shear stress could reach its maximal value. The maximal shear stress for the smallest area can reach 0.630 Pa, if the bubble is big enough.

The terminal velocity of bubbles increases with the increasing bubble diameter, and above a certain diameter, it drops slowly and then it stays there. Comparing this trend with the shear stress trend,

there might be little correlation between the bubble terminal velocity and the area averaged shear stress. So the averaged water velocity might have some relationship with the shear stress. So the following figure was made to investigate this effect.

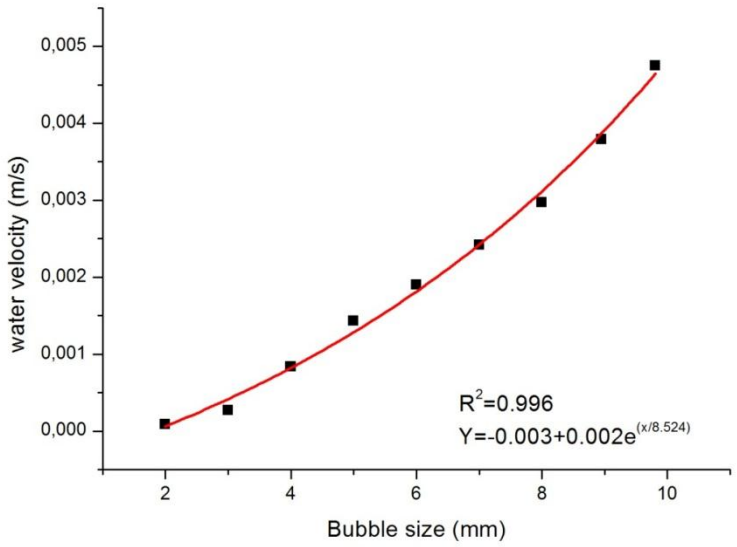

Figure 6.53 The effect of bubble size on the averaged water velocity

It shows clearly that the averaged water velocity increases with the increasing bubble size. And as analyzed before, the shear stress is related to the average velocity of the fluid. And it did show the same trend with the increasing bubble size in the following figure. It's just the increasing rate of the two curves are not same.

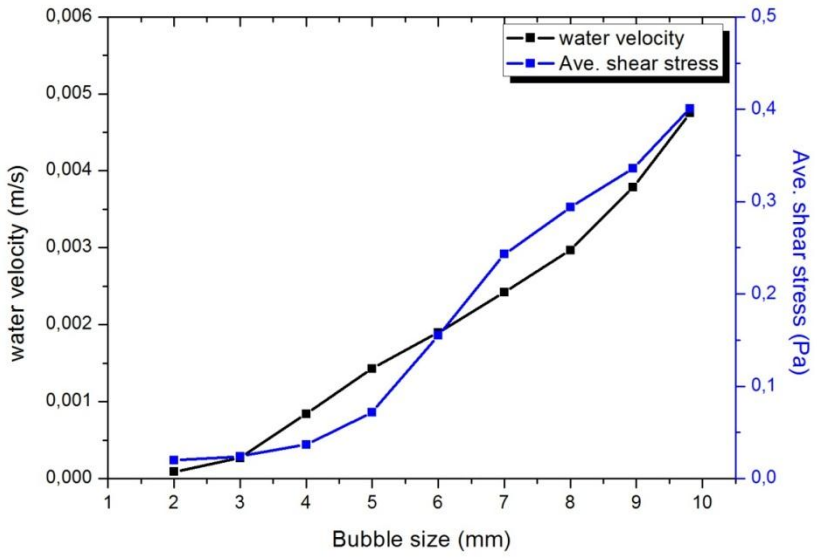

Figure 6.54 The effect of bubble size on water velocity and averaged shear stress

6.6.4. Fluid Velocity

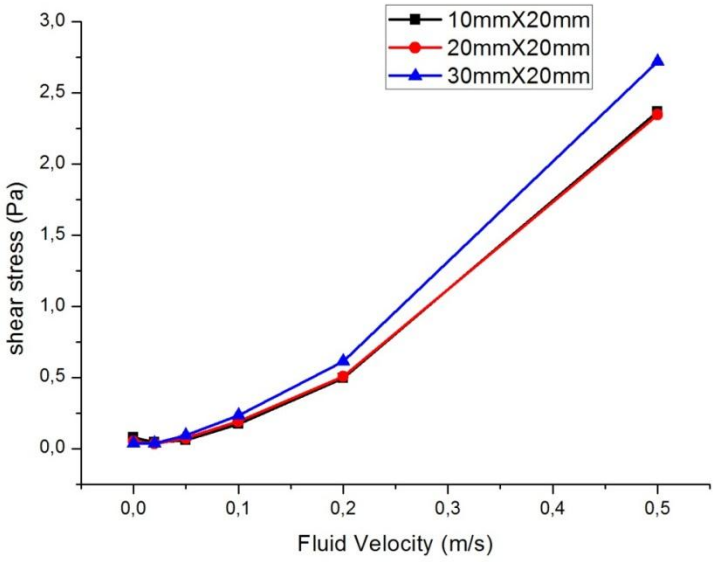

Figure 6.55 The effect of fluid velocity on the maximal area averaged shear stress for three different areas

The fluid velocity doesn't have any effect on the relative bubble rising velocity. But it has a powerful effect on the shear stress. The shear stress profile on the membrane in these cases is quite different compared to the shear stress profile induced only by the rise of a single bubble. Because of the fluid velocity, the shear stress on the membrane are almost the same, whereas in the stagnant water only high shear stress exists near the bubble, the shear stress on the other parts of the membrane is nearly 0. The maximal shear stress occurs still at the same height of the bubble. But among all of the average shear stresses on the areas defined as before, the highest shear stress occurs at the beginning, not when the bubble moves out of the membrane. The averaged shear stresses on these areas when the single bubble reaches the upper edge of the membranes are graphically shown in the figure above. It is obvious that an increase in the fluid velocity leads to an increase of averaged shear stress on the membrane. However, comparing the case of stagnant water and the case of water with a velocity of 0.02 m/s, the shear stress induced only by bubble on the smallest area is actually higher than that in the fluid with a low velocity.

In order to investigate the effect of the bubble motion in the fluid with a low velocity, a simulation with the inlet velocity of 0.02 m/s and without any patch of bubble in the domain was carried out. It was found out that the bubble motion can improve the averaged shear stress on the membrane by 50%. Without bubble the averaged shear stress on the largest area is 0.024 Pa, while it is about 0.037 Pa when the bubble rises between the membranes. The increase of the shear stress because of the bubble motion was also found in the previous literature by by Ndina et al. [94] and by H. Prieske et al. [92].

6.7. 2D vs. 3D

For a 4 mm bubble, the simulation was carried out both in 2d model and 3d model. In 2d simulation, it requires much less computational resources and it also saves a lot of computing time. But it is still a question if the values obtained from the 2d modeling are reliable.

The terminal rising velocity for a 4 mm in 2d is 0.084 m/s, which is about the half of the value obtained from the 3d simulation. The difference of the two values is almost 50%. And it also displayed

in the section 6.1 that in the experiment the terminal rising velocity for a 4 mm is much larger than 0.084 m/s. So the numerical results from the 3d model are much more reliable.

In respect of the maximal shear stresses which are both from the 2d model and 3d model, the value in the 2d model is 4.7 Pa and in the 3d model 0.32 Pa. The difference of the maximal shear stress is much larger than that of the terminal velocity. For the bubble with the same diameter the higher terminal velocity of bubbles might indicate the higher shear stress. But in fact the bubble rises slower in 2d model, but at the same time it can create much higher shear stress. Comparing the path of the bubbles in 2d model and 3d model, in 3d model the bubble moves helically and it doesn't touch the membrane at all. But in 2d model, the bubble bounces against one of the membrane repeatedly. In this way, the bubble can induce higher shear stress on the membrane.

The numerical results from 2d simulation may be not reliable, because planar 2d space was applied to the setting. If this is used for the simulation, it cannot guarantee that the bubble in this simulation is spherical in the beginning and during the simulation. Instead of planar 2d space, axisymmetric swirl 2d space is another option. But if the setting is axisymmetric swirl 2d space, the bubble in 3d will be spherical in the beginning; the domain will be a column, which is not a membrane channel as expected. The geometry of the 2d model doesn't match the geometry in practice and the geometry of the model has a very powerful effect on the numerical results. Thus the values from the 2d model are not that much reliable as the values from 3d model. However, some predictions from the 2d model e.g. higher shear stress can be observed through the bubble bouncing against the membrane are still reliable.

7. Further Work

7.1. The Simulation of Flexible Membrane Wall

7.1.1. Model Geometry

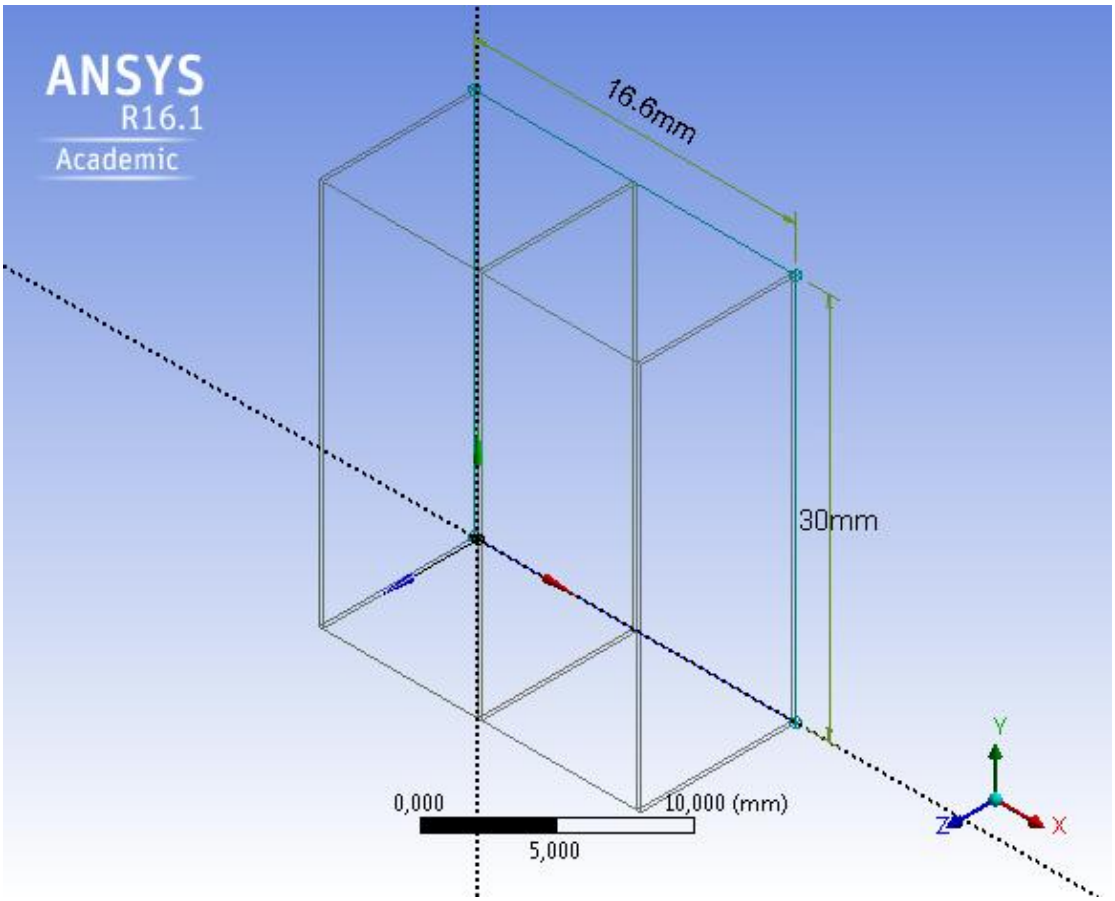

Figure 7.1 Sketch of simulation domain

As shown above, the model consists of three membranes with a thickness of 0.2 mm and two channel gaps between these three membranes. Each of the gaps is 8 mm wide. The height of the first model was 30 mm. It took more than a month for the simulation. However, because of the damage of my hard driver, the data of the simulation were lost. So a second model with the height of 10 mm was applied to the second simulation to reduce the computing time. As analyzed before, the geometry of the model with a length of 8 mm for a 4 mm bubble might lead to an unreliable numerical result. But the error in respect to terminal velocity is within 15%. Considering the requirement of the computational resource the model is still used for this simulation to reduce the requirement of computational resource.

7.1.2. Simulation Settings

Two-way system coupling was used for the solid and fluid simulations. As shown in the figure below, the solid will be solved in Transient Structural and the fluid field will be solved in the Fluent. For the two solvers, they share the same geometry, but the mesh of membranes and the mesh of fluid were generated in their solvers separately. Through the Setup in System Coupling, the data transfers were setting of interfaces between solid and fluid.

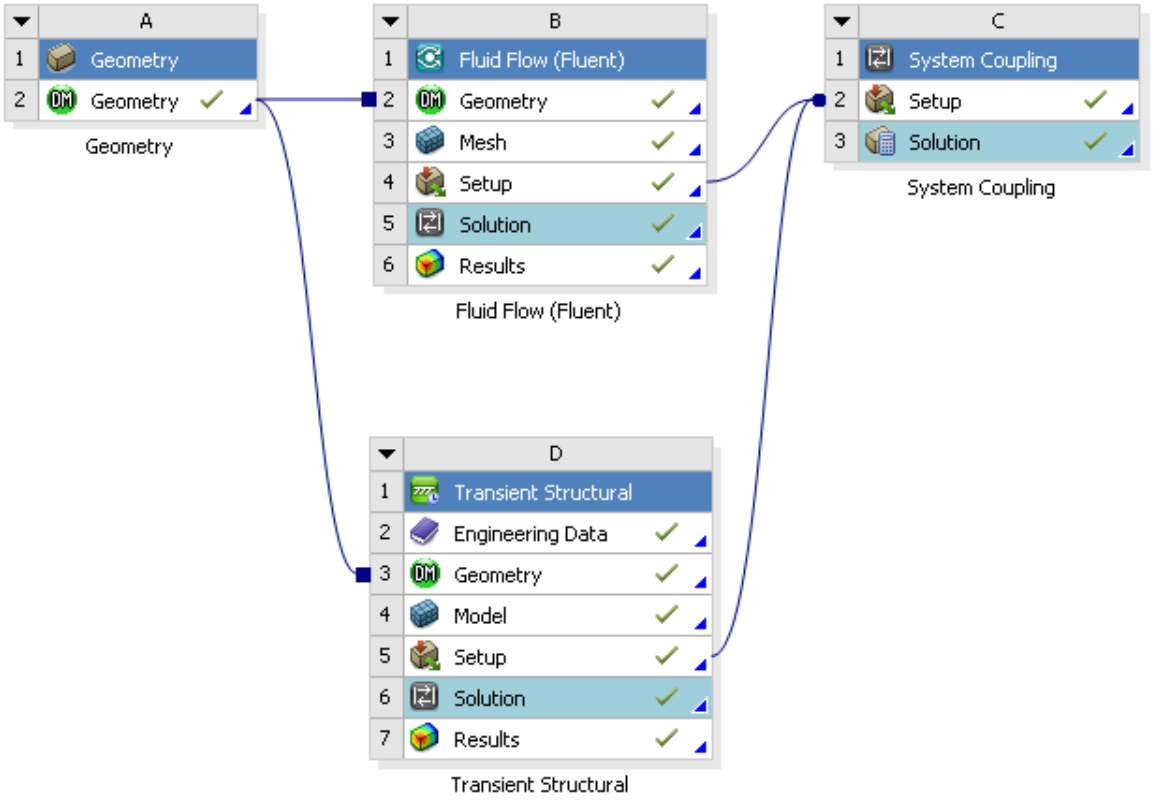

Figure 7.2 Two-way system coupling in workbench

The settings in Fluent were almost the same as before. Only dynamic mesh was chosen for the movement of the membrane. The movement was actually caused by the deformation of the mesh of the domain in the setting of dynamic mesh; the interface of fluid and solid and the deformation of the domain were set. In Transient Structural the density of membrane was set to 2000 kg/m^3. The tensile yield strength and the compressive yield strength were set to 150 MPa and 220 Mpa, which are given by the company. The structured mesh grid with a size of 0.1 mm was generated. The top and the bottom of the membranes were fixed supports. The interface of fluid and solids were set as fluid-solid interfaces, where the data can be transferred.

7.1.3. Numerical Results

The results from Fluent and Transient Structural were displayed in the following figures respectively.

From the figures below, the air volume fraction in this system coupling simulation was the same as the results from Fluent alone. Because of the short time in this simulation, it is hardly observed that the bubble is rising in the simulation. The deformation of the membrane in the picture is observable. The movement of the membrane has a powerful influence on the maximal shear stress. The maximal shear stress during the simulation in the system coupling modeling was 12.48 Pa, which is more than ten times greater than the maximal shear stress in the simulation with a rigid membrane. The maximal shear stress induced by the rise of the bubble and the movement of the membrane might be greater, if the simulation time is longer.

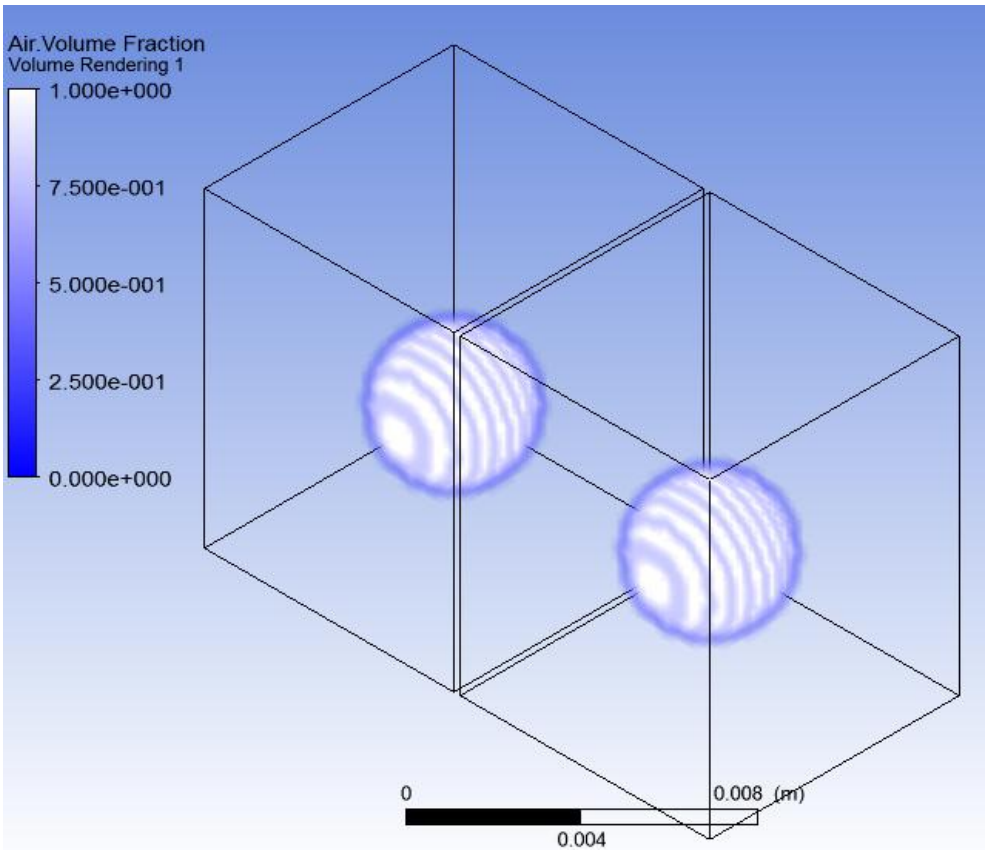

Figure 7.3 Bubble rising in Fluent

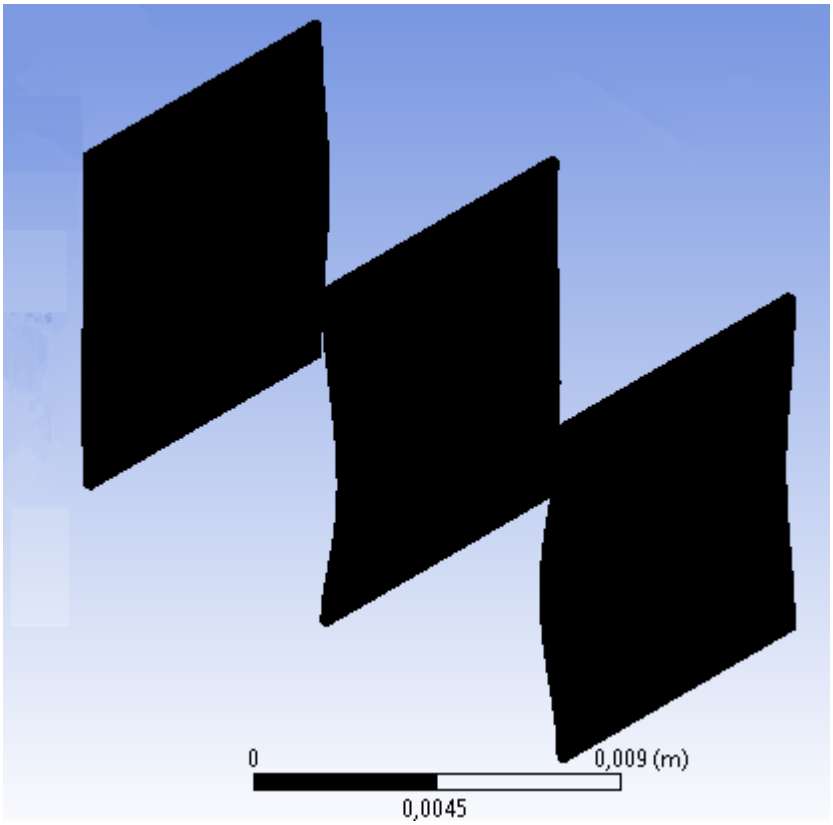

Figure 7.4 Membrane deformation in Transient Structural

7.1.4. Suggestions for this Simulation

The geometry of the model should be large enough. The length of the model should be at least 5 times as large as the bubble diameter. The length of the membrane should be the same as the value in practice, because the displacement of the membrane depends on the size of membrane greatly.

Despite the significant effect of the movement of flexible membrane on the bubble dynamics and shear stress on the membrane, it is not recommendable to carry out a two-way system coupling simulation for the MBR system with the consideration of the time that it takes for the simulation.

The simulation should be carried out long enough, so that the effect of the flexible membrane walls on the bubble behavior can be studied.

8. Conclusion

8.1. Overview

This research has exanimated the shear stress induced by the rise of a single bubble on MBR-membrane plates, the bubble dynamics during the rising by the use of CFD. The objective of the study is to have a better understanding of the hydrodynamics during the membrane filtration. This has been achieved by modeling a single bubble behavior in the channel gap of membranes. The bubble behavior and its effect on the shear stress, and its effect on the shear force when it moves out of the gap were investigated. Besides, the factors which affect the bubble formation were studied earlier. At last the effect of the flexible membrane wall instead of rigid wall on the maximal shear stress on the membrane was exanimated. This has been achieved by two-way system coupling in workbench. The fluid field was simulated by Fluent. And the behavior of the membranes was modeled by Transient Structural. The communication and data transfer of the two solvers were carried out by System Coupling.

In the following, conclusions which were drawn from this study will be presented in this section to describe the hydrodynamics during the aeration process in membrane filtration by the use of CFD. Then some recommendations are made for future works concerning the numerical simulation of membrane filtration in MBR system

8.2. Conclusions

A commercial computational fluid package ANSYS was applied to carry out the simulation which can predict the hydrodynamic behavior of a single rising bubble and the shear stress induced by it on the membrane surface. It can also give the prediction of the cleaning effect and filtration flux during membrane filtration. The conclusions are divided into 10 parts.

8.2.1. Validation and Verification

The results from this simulation was verified against the experimental results, which was carried out in this study as well, against the analytical data, which were calculated by the use of the model found in previous literature and by the use of the computing data same as in the simulation, against the experimental and computational data from the literature.

The experimental data in the large apparatus were in good agreement with the computational and experimental data from the literature, which also have the same conditions as the experiment which was conducted in this study. However, the experimental data, which was obtained when bubbles were rising in the 8 mm channel gap of membranes, didn't match the data from this simulation. The reason for this disagreement is that a serial of bubbles instead of a single was injected into the container. When bubbles rise upward, the flow under the bubble has already affected by this bubble. The fluid is no longer stagnant, whereas the fluid in the simulation is stagnant. If the fluid has an upward velocity, the absolute rising velocity of bubbles as measured in the experiment will be definitely higher than the velocity in the simulation.

To avoid this effect, a small model was built by a 3D printer to carry out the experiment. The data from this experiment agreed well with the numerical data. The error between the both results was within 1%. And in this small apparatus the amount of bubbles can be controlled manually. And the fluid velocity is much lower than the fluid velocity in the large apparatus.

The numerical results were validated against the analytical results regarding the bubble aspect ratio. A very good agreement was achieved. However, this model was proposed for the contaminated water

instead of pure water. And compared the numerical data with the data from the literature in the experiment with the contaminated water, they agreed with each other very well for large bubbles. So, it is speculated that the settings in the simulation are not for the pure water, but for the contaminated water, and if the conditions in the experiment are same as the settings in the simulation, their results will agree with each other.

In a whole, the CFD simulation, which was carried out in this study, is capable of predicting an accurate result.

8.2.2. Inlet Geometry, Inlet Velocity

Several simulations both in 2d and 3d were carried out to investigate the affecting factors during the bubble generation process. The conclusions which are drawn from these simulations were displayed as below:

The configurations of the inlet don't affect the bubble aspect ratio, when the bubble was generated. However, it has an effect during the formation of bubbles. The probability of bubble break-up during the formation process may be increased with the increasing inlet.

The gas amount determines the bubble size, which is also a common sense. The bubble equivalent diameter and the amount of gas have a linear relationship. And parameters, e.g. the inlet velocity, the inlet configurations don't have a significant effect on the bubble size during the formation process, if the gas amount is the same.

However, for a continued aeration, the inlet velocity and the geometry of the inlet could play an important part in bubble formation. Under the circumstance of continued aeration, a bunch of bubbles will be generated instead of a single bubble.

Bubbles which were generated through larger inlet hole tend to be larger at the same injection velocity. But the ratio between the volume of the large bubble and the small one is less than the ratio between the areas of the large and the small inlets.

Similar, bubbles generated at high inlet velocity are apt to be larger than bubbles generated at low inlet velocity, when they are injected through the same inlet.

8.2.3. Bubble Size

Bubble size is a very important parameter, which can affect the bubble motion greatly. In the following subsections, the effect of bubble size on the bubble shape, on the bubble aspect ratio, on the bubble terminal velocity, on the maximal shear stress and on the area averaged shear stress on the three different areas of the membrane will be presented respectively.

Bubble Shape Regime

As discussed before that based on the bubble shape bubbles can be divided into three categories: spherical bubbles, ellipsoidal bubbles and spherical-cap bubbles. In the simulation the small bubbles with a diameter of 2 mm or 3 mm tend to have a spherical shape, bubbles with medium diameter in the range of 4 mm-7 mm belong to ellipsoidal bubbles and large bubbles (8 mm-10 mm) have a shape of spherical-cap. This classification was based on the shape of the bubbles in the simulation. Based on the analysis and the Grace diagram, only 10 mm bubble belongs to the spherical-cap regime, the others are Wobbling bubbles. And based on the data from the literature, only bubbles with a diameter larger than 15 mm have a shape of spherical-cap. This disagreement might be caused by the existence of the

membranes. When the bubble diameter is equal and greater than the gap width, the deformation occurs mainly in the vertical dimension of the bubble. These bubbles are typical Taylor bubbles, which belong to the slug bubble regime. In return, it indicates that the flow pattern in the simulation is a slug flow.

Bubble Aspect Ratio

Bubbles were deformed more severely with the increasing diameter. Small bubbles with diameter less than the gap width deform mainly in the horizontal direction. The other large bubbles deform mainly in the vertical direction. Because the bubble shape has a very powerful impact on the dynamics of bubble motion, the relationship between the bubble size and the aspect ratio was investigated by the use of the model from the previous model. It was found out that the aspect ratio of bubble shape has a more powerful impact on fine bubbles than coarse bubbles under the circumstance that the membrane didn't exist and the bubble moves freely.

Bubble Terminal Velocity

An increase in the bubble size leads to an increase in the terminal velocity for small bubbles and the terminal velocity reaches its maximum at the bubble diameter of 5 mm, above which it begins to decrease slowly. Then the bubble with larger size rises with a constant terminal velocity. The relationship between the terminal velocity and the bubble size is as described before because of the existence of membranes, which has a very powerful effect on the bubble aspect ratio and bubble terminal rising velocity. Bubbles with a diameter greater than the channel gap distances rise with a relative constant velocity. Bubbles with a medium size but with a size less than the gap distance, the bubble rising was slowed down because of the membranes. For small bubbles the effect of membrane gap was not significant.

The relationship between the bubble size, the bubble shape and the terminal velocity were analyzed as well. For the spherical bubbles the terminal velocity increases with the increasing bubble diameter. But the rule didn't fit for the bubbles with severe deformations.

The Maximal Shear Stress

The maximal shear stress improves with the increasing bubble size, which is also in agreement with the conclusions from the previous literature. The increasing rate for the small bubbles is high, but for large bubbles is low.

The maximal shear stress for small and large bubbles occurs at the same height of the bubble location. But the shear stress profiles for them are quite different. The maximal shear stress profile for bubbles with a diameter less than 6 mm has only one peak at the middle of the membrane in the x direction. For large bubbles with the size equals to and greater than 6 mm, the maximal shear stress occurs not in the middle of the membrane, but both on the left and the right side of the membrane in the x direction. And for bubbles with a spherical-cup shape, the maximal shear stress is not in the middle of the bubble in y direction, but in the middle bottom part.

The dependence of the maximal shear stress on bubble size was investigated for large bubbles and small bubbles respectively, based on the shear stress profile. Both of them show an exponential dependence. But the increasing rate for small bubbles is larger than the increasing rate for large bubbles

Averaged Shear Stress in Escape Zone

The shear forces in the escape zone were calculated for three different areas. To achieve a better comparison of the shear forces, area averaged shear stress was applied. The area averaged shear stress increases with the increasing bubble size. But the increasing rate increases at first until to the maximum, and then it drops down again.

8.2.4. Gap Distances

The existence of the membranes and the channel gap distance between membranes affect the bubble dynamics significantly, especially for bubbles, whose diameter are larger than the gap width of membranes.

The gap widths were set from 6 mm to 10 mm, which is also common in the membrane filtration in the MBR system. The terminal velocity shows clearly an increasing dependence on the gap distance of membranes, while the shear stress shows a decreasing trend with increasing gap width. The conclusions agree with the conclusions drawn from previous literature. With the consideration of the clogging problem by particles during the membrane filtration in MBR systems, it is recommended that the 6 mm gap width should be applied to the MBR system. Because the maximal shear stress exerted by the rise of a single bubble in the channel gap of 6 mm is about 5 times higher than that in a 7 mm channel.

8.2.5. Viscosity

The viscosities of the fluid, which can reflect the MLSS concentration of the MBR system, affect the bubble dynamics greatly. The terminal velocity decreases with increasing MLSS concentration and increasing viscosity.

As analyzed before, the shear stress depends directly on the viscosity of the fluid and the average fluid velocity near the wall. But an increase in the viscosity can lead to a decrease of bubble terminal velocity, which in return affects the average fluid velocity near the wall. So the relationship between the shear stress and the fluid viscosity is no longer as simple as between the terminal velocity and viscosity.

When the viscosity increases at first, the average fluid velocity might be decreased. The change of velocity might be greater than the change of viscosity. It is the velocity that domains in this relationship. Therefore, the wall shear stress decreases with the increasing viscosity. But above a certain viscosity, the effect of the change in the fluid velocity is no longer that much powerful as the effect of the change of the viscosity on shear stress. So, a further increase in the viscosity leads to an increase in the shear stress.

8.2.6. Temperature

Without consideration of the effect of temperature on the surface tension and some other properties of the fluid, only the viscosity of the fluid is expressed as a function of temperature for both water and sludge with a MLSS concentration of 8 g/L. The terminal velocity both for water and sludge increase with the increasing temperature, because the velocity becomes lower, which lead to an increasing terminal velocity.

The shear stress for sludge shows an increasing trend with the increasing temperature, while the shear stress for water shows a decreasing trend. It can be explained by the same reason in the last subsection as well, because temperature only changes the viscosity values. The viscosity of water and sludge

maybe belong to two different regimes. For water a dramatic change of viscosity and a slight change of fluid velocity might be caused by increasing the temperature. Therefore the shear stress for water decreases with the increasing temperature. However, for sludge, the dramatic increase of fluid velocity and a slight decrease in viscosity when the temperature is increased. So the shear stress for sludge increases with the increasing temperature.

8.2.7. Fluid Velocity

The absolute bubble rising velocity is equal to the relative terminal rising velocity plus the velocity of fluid around the bubble. The relative terminal rising velocity stays the same, whatever the fluid velocity changes.

The fluid velocity shows little impact on the relative bubble rising velocity, while it has a powerful effect on the shear stress. The high shear stress is no longer concentrated on the area, where the bubble appears. It is evenly distributed along the membrane surface. But the maximal shear stress still occurs at the same height of the bubble location. And an increase in the fluid velocity is apt to increase the shear stress.

Results from the simulation of the model with a single bubble in the fluid with a velocity of 0.02 m/s and the simulation of the model which has a fluid velocity of 0.02 m/s as well but has no bubble rising in the domain were compared. It was found out that the bubble motion can improve the averaged shear stress on the membrane by 50%. Without bubble the averaged shear stress on the largest area is 0.024 Pa, while it is about 0.037 Pa when the bubble rises between the membranes. This confirmed that the use of gas can achieve a better cleaning effect.

8.2.8. Flexibility of the Membrane Walls

The movement of membrane can improve the shear stress on the membrane surface. The maximal shear stress during the simulation in the system coupling modeling was 12.48 Pa, which the maximal shear stress was 0.08 Pa for the simulation of the model with a rigid membrane wall. This is a significant increase in shear stress by the movement of membrane wall.

The data from the first simulation, whose computing time was almost one month, were lost because of the damage of my hard driver. The second simulation didn't last so long because of the deadline to hand in this thesis. If the simulation last longer, the effect of the membrane movement on the bubble motion could be investigated.

8.2.9. Other Parameters

Bubble Trajectory

The trajectory of this bubble is apt to be zigzag, whereas the rising path for large bubbles with ellipsoid shape tends to be helical. And the bubble path, especially the bubble location in the x direction has a very powerful impact on the shear stress. The shear stress on the membrane surface is much higher, when the bubble is closer to the membrane wall. And in the 2d simulation, the bubble bounced against the wall repeatedly. And in this case the shear stress exerted by the bounce of the bubble is much higher.

Operating Pressure

Operating pressure shows little effect on the bubble dynamics and shear stress induced by the rise of a bubble on the membrane surface.

However, it didn't mean that the pressure didn't have any effect on the bubble motion. Of course, in practice the pressure can affect the bubble size and it is also a very important parameter for the gas is compressible. What's more, the surface tension depends on the pressure as well. But in the simulation, the gauge pressure at the water surface is always 0 Pa, because the operating pressure was applied to the gas phase. Therefore, the bubble motion isn't affected by the operating pressure in the simulation.

Initial Velocity of Bubbles

Like the operating pressure, the initial velocity which is patched to the single bubble in the beginning did have little impact on the bubble motion. Because in the simulation the bubble was patched in the stagnant water, the bubble had the initial velocity but the fluid was without any velocity. The bubble was bouncing into the fluid; the velocity of the bubble becomes 0 m/s in a very short time. That's why the initial velocity doesn't have any effect on the hydrodynamics of bubble rising.

2D vs. 3D

The terminal rising velocity for a 4 mm in 2d is 0.084 m/s, while it is 0.169 m/s in 3d simulation. The difference of the two values is almost 50%. Checked the bubble terminal rising velocity against the experimental data, the results obtained from the 3d model are much more reliable. The disagreement of the results in 2d model and the results of 3d model lies in the setting of the simulation. In 2d simulation, the model was set as planar space. In this way, the bubble will not be spherical in 3 dimensions. If the model was set as axisymmetric swirl space, the geometry of the domain will be a column instead of a rectangle. In both cases, the model doesn't fit the actual model during membrane filtration in MBR System.

The maximal shear stress in the 2d model is 4.7Pa and in the 3d model 0.32 Pa. The Error of the maximal shear stresses in both cases is almost 100%. Because in 2d model, the bubble bounces against one of the membrane repeatedly, the shear stress induced in this way is much higher than that only exerted by the rise of a single bubble. Maybe the values from the 2d model are inaccurate, but the trend obtained from the 2d model is still reliable.

8.3. Recommendations for Future Works

Some assumptions are made to simplify the problem in this simulation just like in previous literature. For bubbles, they are set to have a uniform size and the effect of collisions, coalescence and break-up between bubbles is neglected. For membrane walls, it is treated as rigid wall and impermeable walls. But these assumptions will increase the risk of deviation between the real situation and the numerical results.

As indicated in this study, if the membrane wall is treated as flexible wall, the shear stress on the membrane surface is much higher. Then the filtration flux and cleaning effect based on the shear stress will be improved significantly. It is recommended to carry out the simulation of the model with flexible wall if the computational resource is accessible.

To avoid large deviation between the simulation and the real situation, some considerations are presented in the following subsections. And some consideration which is interesting especially in the field of MBR system are also made.

8.3.1. Coupling with PBM Model

In this study, only a single bubble was patched in the water to simplify the simulation. And the shear stress and shear force exerted by this single bubble were very small. In the aeration process of an actual MBR system, a group of bubbles with different diameters exist in the channel gap between membranes at the same time. So a CFD simulation of bubbles with a wide size distribution instead of a single bubble can reflect the actual situation during the aeration process. Besides, large bubbles may break up into several small bubbles and small bubbles may emerge into one large bubble during the aeration. However, only few CFD simulations of gas-liquid flow in MBR systems considers the effect of bubble size distribution, bubble break-up and coalescence.

The population balance model (PBM) coupled into the CFD, is turned out to be an effective way for a gas-flow simulation with the consideration of bubble size distribution and bubble break up and coalescence effect.

The PBM was coupled with an Eulerian model in this study. In population balance model the minimal diameter was set as 0.001 m and the maximal diameter was set as 0.012 m. The luo-model was applied for the aggregation kernel and the frequency of breakage kernel.

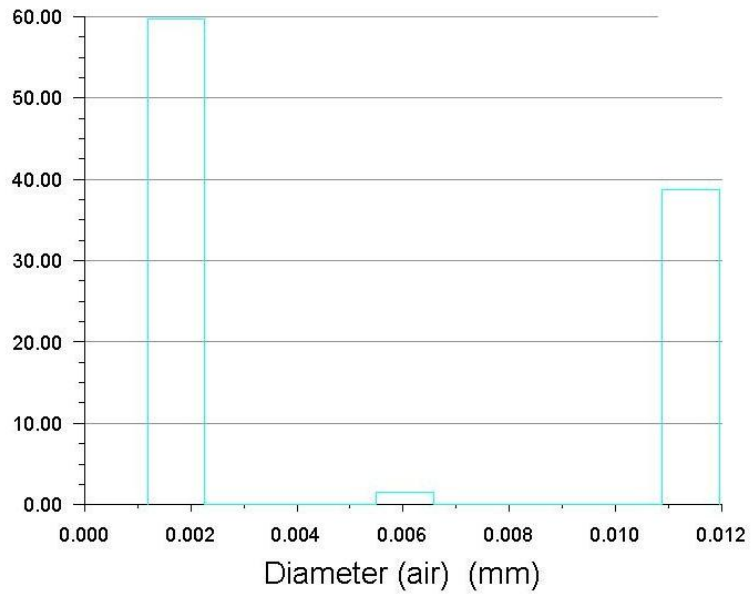

Figure 8.1 Histogram of bubble size distribution

The histogram graph of bubble size distribution was shown in the figure above. The majority of bubbles in the container is small. Bubble with medium size accounts for only 2%. With the increasing time, the proportion of large bubbles is increasing and small bubbles are less and less. This phenomenon indicates the coalescing behavior of bubbles. The small bubbles are merging together.

8.3.2. Coupling of ASM Model

Coupling ASM (Activated Sludge Model) into CFD can be achieved by the following equation [81]:

$$\frac{\partial(X_{species})}{\partial t} + \mathrm{div}\left(\boldsymbol{u}X_{species}\right) = \mathrm{div}\left(\Gamma_t grad X_{species}\right) + S_{species} \quad (8\text{-}1)$$

Where $X_{species}$ is the mass fraction concentration of the species; Γ_t is the turbulent diffusion factor and $S_{species}$ is the source and sink term caused by the biological reaction.

$X_{species}$ is incorporated into the model through UDS (User Defined Scalar). Γ_t can be given directly through the setting in the GUI of Fluent. $S_{species}$ is the source term, which can be compiled into the simulation through UDF (User Defined Function), as shown below.

$$source = -\frac{1}{Y}\mu_{max}\frac{S}{S+K_s}X \tag{8-2}$$

Where X: biomass concentration; S: growth-limiting substrate concentration in solution; Y: true yield coefficient; K_s: half-velocity constant, substrate concentration at one-half the maximum specific substrate utilization rate; μ_{max}: maximum specific bacterial growth rate.

The derivative of the source term, which must be given in the definition of source term as well, is shown in the following equation:

$$\mathrm{d}S[\mathrm{eqn}] = -\frac{1}{Y}\mu_{max}\frac{K_s}{(S+K_s)^2}X \tag{8-3}$$

The two equations above are simplified mathematical model without consideration of the formation of cell debris of biomass and with the hypothesis that the relationship between the total suspended solids (TSS) concentration and the substrate concentration is constant.

List of Tables

List of Figures

Abbreviations

ASM	Activated Sludge Model
CFD	Computational Fluid Dynamics
COD	Chemical Oxygen Demand
DNS	Direct Numerical Simulation
EPS	Extracellular Polymeric Substances
HBP	Herschel-Buckley relationship with Papanastasiou's adaption
HF	Hollow Fiber membrane
FDM	Finite Difference Methods
FEM	Finite Element Methods
FS	Flat Sheet membrane
FVM	Finite Volume Methods
LES	Large Eddy Simulation
MBR	Membrane Bio-Reactor
MF	Microfiltration
MLSS	Mixed Liquor Suspended Solids
NF	Nanofiltration
NOM	Natural Organic Matter
PBM	Population Balance Model
PDE	Partial Differential Equation
PISO	Pressure Implicit with Splitting of Operators
RANS	Reynolds Averaged Navier-Stokes
SAD_m	Specific Aeration Demand against the membrane area
SAD_p	Specific Aeration Demand against the permeate volume
SMP	Soluble Microbial Products
SRT	Solid Retention Time
TMP	Trans Membrane Pressure
TSS	Total Suspended Solids
RO	Reverse Osmosis
UF	Ultrafiltration
UDF	User Defined Function
UDS	User Defined Scalar
VOF	Volume of Fluid

References

1. Judd, S., *The MBR Book: Principles and Applications of Membrane Bioreactors in Water and Wastewater Treatment*. 2006, London, UK: Elsevter Ltd.
2. P.Hillis, *Membrane Technology in Water and Wastewater Treatment*. 2000, UK: Northwest Water Ltd
3. Singh, R., *Membrane Technology and Engineering for Water Purification*. 2nd ed. 2015, UK: Elsevier Ltd.
4. Borchardt, J.C.C.R.R.T.D.W.H.K.J.H.G.T.J.H., *MWH's Water Treatment: Principles and Design*. 3rd ed. 2012, Hoboken, New Jersey: John Wiley & Sons, Inc.
5. LeBerre, O. and G. Daufin, *Skimmilk crossflow microfiltration performance versus permeation flux to wall shear stress ratio.* Journal of Membrane Science, 1996. **117**(1-2): p. 261-270.
6. Chan, C.C.V., P.R. Berube, and E.R. Hall, *Relationship between types of surface shear stress profiles and membrane fouling.* Water Research, 2011. **45**(19): p. 6403-6416.
7. Kaya, R., et al., *Analysis of wall shear stress on the outside-in type hollow fiber membrane modules by CFD simulation.* Desalination, 2014. **351**: p. 109-119.
8. Chan, C.C.V., P.R. Berube, and E.R. Hall, *Shear profiles inside gas sparged submerged hollow fiber membrane modules.* Journal of Membrane Science, 2007. **297**(1-2): p. 104-120.
9. Abdullah, S.Z., et al., *Distribution of surface shear stress for a densely packed submerged hollow fiber membrane system.* Desalination, 2015. **357**: p. 117-120.
10. Wray, H.E., R.C. Andrews, and P.R. Berube, *Surface shear stress and membrane fouling when considering natural water matrices.* Desalination, 2013. **330**: p. 22-27.
11. Thomas Merlin, R.R., *Membranverfahren: Grundlagen der Modul- und Auflagenauslegung*. 3rd ed. 2007, Heidelberg: Springer.
12. Baker, R.W., *Membrane Technology and Applications*. 3rd ed. 2012, UK: John Wiley & Sons, Ltd.
13. Krzeminski, P., J. Gil Linares, A. van Nieuwenhuijzen, J.H.J.M. van der Graaf, J.B. van and Lier, *Flat Sheet or Hollow Fibre – Comparison of Full-scale Membrane BioReactor Configurations.* Desalination and Water Treatment, 2012. **42**(1-3): p. 100-106.
14. Bodik, I., et al., *Comparison of Flat-Sheet and Hollow-Fiber Membrane Modules in Municipal Wastewater Treatment.* Polish Journal of Environmental Studies, 2009. **18**(3): p. 331-340.
15. Braak, E., et al., *Aeration and hydrodynamics in submerged membrane bioreactors.* Journal of Membrane Science, 2011. **379**(1-2): p. 1-18.
16. Yoon, S.-H., *Membrane Bioreactor Processe: Principles and Applications*. 2015: CRC Press.
17. Cui, Z.F. and T. Taha, *Enhancement of ultrafiltration using gas sparging: a comparison of different membrane modules.* Journal of Chemical Technology and Biotechnology, 2003. **78**(2-3): p. 249-253.
18. Cui, Z.F., S. Chang, and A.G. Fane, *The use of gas bubbling to enhance membrane processes.* Journal of Membrane Science, 2003. **221**(1-2): p. 1-35.
19. Yamanoi, I. and K. Kageyama, *Evaluation of bubble flow properties between flat sheet membranes in membrane bioreactor.* Journal of Membrane Science, 2010. **360**(1-2): p. 102-108.
20. Chang, I.S. and S.J. Judd, *Air sparging of a submerged MBR for municipal wastewater treatment.* Process Biochemistry, 2002. **37**(8): p. 915-920.
21. Rahimi, Y., et al., *Optimizing aeration rates for minimizing membrane fouling and its effect on sludge characteristics in a moving bed membrane bioreactor.* Journal of Hazardous Materials, 2011. **186**(2-3): p. 1097-1102.
22. Boehm, L., et al., *The importance of fluid dynamics for MBR fouling mitigation.* Bioresource Technology, 2012. **122**: p. 50-61.
23. Sofia, A., W.J. Ng, and S.L. Ong, *Engineering design approaches for minimum fouling in submerged MBR.* Desalination, 2004. **160**(1): p. 67-74.
24. Kaisong, Z., C. Zhanfeng, and R.W. Field, *Effect of bubble size and frequency on mass transfer*

in flat sheet MBR. Journal of Membrane Science, 2009. **332**(1-2): p. 30-7.
25. Ningyu, L., et al., *Experimental investigation of hydrodynamic behavior in a real membrane bio-reactor unit.* Journal of Membrane Science, 2010. **353**(1-2): p. 122-34.
26. R. Cllift, J.R.G., M. E. Weber, *Bubbles, Drops and Particles*. 1978, New York: Academic Press.
27. Khan, M.J.H., et al., *CFD simulation of fluidized bed reactors for polyolefin production - A review.* Journal of Industrial and Engineering Chemistry, 2014. **20**(6): p. 3919-3946.
28. Grace, J.R., *Shapes and Velocities of Bubble Rising in Infinite Liquids.* Trans. Inst. Chem. Eng., 1973: p. 51,116.
29. Annaland, M.V., et al., *Numerical simulation of behavior of gas bubbles using a 3-D front-tracking method.* Aiche Journal, 2006. **52**(1): p. 99-110.
30. Brennen, C.E., *Fundamentals of Multiphase Flows*. 2005: Cambridge University Press.
31. Zhang, K.S., et al., *Effect of the bubbling regimes on the performance and energy cost of flat sheet MBRs.* Desalination, 2011. **283**: p. 221-226.
32. H.K. Versteeg, W.M., *An Introduction to Computational Fluid Dynamics The Finite Volume Method*. 1995, England: Longman Scientific & Technical
33. Amini, E., et al., *Experimental Study and Computational Fluid Dynamics Simulation of a Full-Scale Membrane Bioreactor for Municipal Wastewater Treatment Application.* Industrial & Engineering Chemistry Research, 2013. **52**(29): p. 9930-9939.
34. Sousa, P., et al., *A CFD study of the hydrodynamics in a desalination membrane filled with spacers.* Desalination, 2014. **349**: p. 22-30.
35. Fimbres-Weihs, G.A. and D.E. Wiley, *Review of 3D CFD modeling of flow and mass transfer in narrow spacer-filled channels in membrane modules.* Chemical Engineering and Processing, 2010. **49**(7): p. 759-781.
36. John D. Anderson, J., *Computational Fluid Dynamics: The basics with applications*. 1995, USA: McGraw-Hill,Inc.
37. Blazek, J., *Computational Fluid Dynamics: Principles and Applications*. 2nd ed. 2007, London: Elsevier Ltd.
38. Aksel, J.H.S.N., *Fluid Mechanics*. 2nd ed. 2008, Heidelberg: Springer.
39. Fasihi, M., et al., *Computational fluid dynamics simulation of transport phenomena in ceramic membranes for SO2 separation.* Mathematical and Computer Modelling, 2012. **56**(11-12): p. 278-286.
40. Pozrikidis, C., *Fluid Dynamics: Theory, Computation, and Numerical Simulation*. 2nd ed. 2009, USA: Springer.
41. Wang, C.Y., *EXACT-SOLUTIONS OF THE STEADY-STATE NAVIER-STOKES EQUATIONS.* Annual Review of Fluid Mechanics, 1991. **23**: p. 159-177.
42. Seetharamu, R.W.L.P.N.K.N., *Fundamentals of the Finite Element Method for Heat and Fluid Flow*. 2004, USA: John Wiley & Sons, Ltd.
43. Chung, T.J., *Computational Fluid Dynamics*. 2002, Cambridge UK: Cambridge University Press.
44. Yip, S., *Handbook of Materials Modeling*. Vol. 1. 2005, Netherland: Springer.
45. Mendes, A., et al., *"Comparison of finite difference and control volume methods for solving differential equations" by G.G. Botte, J.A. Ritter, R.E. White, 24 (2000) 2633-2654.* Computers & Chemical Engineering, 2005. **29**(10): p. 2256-8.
46. Schaefer, M., *Computational Engineering-Introduction to Numerical Methods*. 2006, Heidelberg: Springer-Verlag.
47. Cao, Z., D.E. Wiley, and A.G. Fane, *CFD simulations of net-type turbulence promoters in a narrow channel.* Journal of Membrane Science, 2001. **185**(2): p. 157-176.
48. Naessens, W., et al., *Critical review of membrane bioreactor models - Part 2: Hydrodynamic and integrated models.* Bioresource Technology, 2012. **122**: p. 107-118.
49. Ndinisa, N.V., D.E. Wiley, and D.F. Fletcher, *Computational fluid dynamics simulations of Taylor bubbles in tubular membranes - Model validation and application to Laminar flow systems.* Chemical Engineering Research & Design, 2005. **83**(A1): p. 40-49.
50. Hirt, C.W. and B.D. Nichols, *A computational method for free surface hydrodynamics.*

Transactions of the ASME. Journal of Pressure Vessel Technology, 1981. **103**(2): p. 136-141.
51. Ferreira, R.B., et al., *Numerical simulations of two-phase flow in proton exchange membrane fuel cells using the volume of fluid method - A review.* Journal of Power Sources, 2015. **277**: p. 329-342.
52. Zahedi, P., et al., *Influence of fluid properties on bubble formation, detachment, rising and collapse; Investigation using volume of fluid method.* Korean Journal of Chemical Engineering, 2014. **31**(8): p. 1349-1361.
53. Ghidossi, R., D. Veyret, and P. Moulin, *Computational fluid dynamics applied to membranes: State of the art and opportunities.* Chemical Engineering and Processing, 2006. **45**(6): p. 437-454.
54. Chang-Wei, K., et al., *Bridging the gap between membrane bio-reactor (MBR) pilot and plant studies.* Journal of Membrane Science, 2008. **325**(2): p. 861-871.
55. Wang, Y., M. Brannock, and G. Leslie, *Membrane bioreactors: overview of the effects of module geometry on mixing energy.* Asia-Pacific Journal of Chemical Engineering, 2009. **4**(3): p. 322-333.
56. Khalili-Garakani, A., et al., *Analyze and control fouling in an airlift membrane bioreactor: CFD simulation and experimental studies.* Process Biochemistry, 2011. **46**(5): p. 1138-1145.
57. Liu, X.F., et al., *Numerical simulation of bubble induced shear in membrane bioreactors: Effects of mixed liquor rheology and membrane configuration.* Water Research, 2015. **75**: p. 131-145.
58. Karabelas, A.J., C.P. Koutsou, and S.G. Yiantsios, *Direct numerical simulation of flow in spacer-filled channels: Effect of spacer geometrical characteristics.* Journal of Membrane Science, 2007. **291**(1-2): p. 53-69.
59. Drews, A., et al., *Advantageous and detrimental effects of air sparging in membrane filtration: Bubble movement, exerted shear and particle classification.* Desalination, 2010. **250**(3): p. 1083-1086.
60. Martinelli, L., C. Guigui, and A. Line, *Characterisation of hydrodynamics induced by air injection related to membrane fouling behaviour.* Desalination, 2010. **250**(2): p. 587-591.
61. Buetehorn, S., et al., *CFD simulation of single- and multi-phase flows through submerged membrane units with irregular fiber arrangement.* Journal of Membrane Science, 2011. **384**(1-2): p. 184-197.
62. Guenther, J., et al., *Modeling the effect of packing density on filtration performances in hollow fiber microfiltration module: A spatial study of cake growth.* Journal of Membrane Science, 2012. **389**: p. 126-136.
63. Guenther, J., et al., *A numerical approach to study the impact of packing density on fluid flow distribution in hollow fiber module.* Journal of Membrane Science, 2010. **348**(1-2): p. 277-286.
64. Lotfiyan, H., et al., *Computational fluid dynamics modeling and experimental studies of oil-in-water emulsion microfiltration in a flat sheet membrane using Eulerian approach.* Journal of Membrane Science, 2014. **472**: p. 1-9.
65. Yan, X., et al., *Hydraulic optimization of membrane bioreactor via baffle modification using computational fluid dynamics.* Bioresource Technology, 2015. **175**: p. 633-637.
66. Ratkovich, N.H., Michaela; Futselaar, Harry; Nopens, Ingmar, *Use of CFD to Model and Optimize the Hydrodynamics of an Airlift MBR Side-Stream Module.* WEFTEC, 2009: p. 2812-2818(7).
67. Brannock, M., Y. Wang, and G. Leslie, *Mixing characterisation of full-scale membrane bioreactors: CFD modelling with experimental validation.* Water Research, 2010. **44**(10): p. 3181-3191.
68. Ratkovich, N., et al., *Experimental study and CFD modelling of a two-phase slug flow for an airlift tubular membrane.* Chemical Engineering Science, 2009. **64**(16): p. 3576-3584.
69. Wei, P., et al., *CFD modeling of hydrodynamic characteristics of slug bubble flow in a flat sheet membrane bioreactor.* Journal of Membrane Science, 2013. **445**: p. 15-24.
70. Le-Clech, P., B. Jefferson, and S.J. Judd, *A comparison of submerged and sidestream tubular membrane bioreactor configurations.* Desalination, 2005. **173**(2): p. 113-122.

71. Bohmn, L. and M. Kraume, *Fluid dynamics of bubble swarms rising in Newtonian and non-Newtonian liquids in flat sheet membrane systems.* Journal of Membrane Science, 2015. **475**: p. 533-544.
72. Taha, T., et al., *Gas-sparged ultrafiltration using horizontal and inclined tubular membranes - A CFD study.* Journal of Membrane Science, 2006. **279**(1-2): p. 487-494.
73. Wang, T.F., J.F. Wang, and Y. Jin, *A CFD-PBM coupled model for gas-liquid flows.* Aiche Journal, 2006. **52**(1): p. 125-140.
74. Tiefeng, W., *Simulation of bubble column reactors using CFD coupled with a population balance model.* Frontiers of Chemical Science and Engineering, 2011. **5**(2): p. 162-72.
75. Yang, F., et al., *Yield stress and rheological characteristics of activated sludge in an airlift membrane bioreactor.* Journal of Membrane Science, 2009. **334**(1-2): p. 83-90.
76. Laera, G., et al., *Membrane bioreactor sludge rheology at different solid retention times.* Water Research, 2007. **41**(18): p. 4197-4203.
77. Garakani, A.H.K., et al., *COMPARISON BETWEEN DIFFERENT MODELS FOR RHEOLOGICAL CHARACTERIZATION OF ACTIVATED SLUDGE.* Iranian Journal of Environmental Health Science & Engineering, 2011. **8**(3): p. 255-264.
78. Ratkovich, N., et al., *Activated sludge rheology: A critical review on data collection and modelling.* Water Research, 2013. **47**(2): p. 463-482.
79. Krauth, K. and K.F. Staab, *PRESSURIZED BIOREACTOR WITH MEMBRANE FILTRATION FOR WASTE-WATER TREATMENT.* Water Research, 1993. **27**(3): p. 405-411.
80. Le Moullec, Y., et al., *Activated sludge pilot plant: Comparison between experimental and predicted concentration profiles using three different modelling approaches.* Water Research, 2011. **45**(10): p. 3085-3097.
81. Brannock, M., *Computational Fluid Dynamics Tools for the Design of Mixed Anoxic Wastewater Treatment Vessels.* 2003.
82. Le Moullec, Y., et al., *CFD simulation of the hydrodynamics and reactions in an activated sludge channel reactor of wastewater treatment.* Chemical Engineering Science, 2010. **65**(1): p. 492-498.
83. Tomiyama, A., et al., *Terminal velocity of single bubbles in surface tension force dominant regime.* International Journal of Multiphase Flow, 2002. **28**(9): p. 1497-1519.
84. Wellek, R.M., A.K. Agrawal, and A.H. Skelland, *SHAPE OF LIQUID DROPS MOVING IN LIQUID MEDIA.* Aiche Journal, 1966. **12**(5): p. 854-&.
85. L.S. Fan, K.T., *Bubble Wake Dynamics in Liquids and Liquid-Solid Suspensions*. 1990, London: Butterworth-Heinemann.
86. Ma, D., et al., *Two-dimensional volume of fluid simulation studies on single bubble formation and dynamics in bubble columns.* Chemical Engineering Science, 2012. **72**: p. 61-77.
87. M.T.Islam, P.G., J.N.Sahu, M.N.Uddin, A.Mannan, *A Single Air Bubble Rise in Water: A CFD Study.* Mechanical Engineering Research Jounal, 2013. **9**: p. 1-6.
88. Vries, A.d., *Path and wake of a rising bubble*. 2001, University of Twente.
89. Islam, M.T., P. Ganesan, and J. Cheng, *A pair of bubbles' rising dynamics in a xanthan gum solution: a CFD study.* Rsc Advances, 2015. **5**(11): p. 7819-7831.
90. A.Tomiyama, *Single bubbles in stagnant liquids and in linear shear flows.*
91. Liu, L., H.J. Yan, and G.J. Zhao, *Experimental studies on the shape and motion of air bubbles in viscous liquids.* Experimental Thermal and Fluid Science, 2015. **62**: p. 109-121.
92. Prieske, H., et al., *Optimised hydrodynamics for membrane bioreactors with immersed flat sheet membrane modules.* Desalination and Water Treatment, 2010. **18**(1-3): p. 270-276.
93. Podvin, B., et al., *Model and experimental visualizations of the interaction of a bubble with an inclined wall.* Chemical Engineering Science, 2008. **63**(7): p. 1914-1928.
94. Ndinisa, N.V., et al., *Fouling control in a submerged flat sheet membrane system: Part II - Two-Phase flow characterization and CFD simulations.* Separation Science and Technology, 2006. **41**(7): p. 1411-1445.